Ph. D Thesis

박사 학위논문

Analysis and Modeling of Capacity Fading in Lithium Ion Batteries

Williams Agyei Appiah (아피아)

Department of

Energy Science and Engineering

DGIST

2020

Analysis and Modeling of Capacity Fading in Lithium Ion Batteries

Advisor: Professor Yong Min Lee
Co-Advisor: Professor Myung-Hyun Ryou

by

Williams Agyei Appiah

Department of Energy Science and Engineering
DGIST

A thesis submitted to the faculty of DGIST in partial fulfillment of the requirements for the degree of Doctor of Philosophy in the Department of Energy Science and Engineering. The study was conducted in accordance with Code of Research Ethics[1].

05. 29. 2020

Approved by

Professor Yong Min Lee
(Advisor)

Professor Myung-Hyun Ryou
(Co-Advisor)

[1].Declaration of Ethical Conduct in Research: I, as a graduate student of DGIST, hereby declare that I have not committed any acts that may damage the credibility of my research. These include, but are not limited to: falsification, thesis written by someone else, distortion of research findings or plagiarism. I affirm that my thesis contains honest conclusions based on my own careful research under the guidance of my thesis advisor.

Analysis and Modeling of Capacity Fading in Lithium Ion Batteries
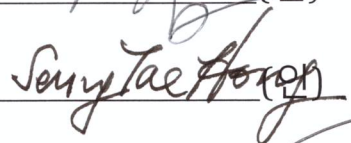
Williams Agyei Appiah

Accepted in partial fulfillment of the requirements for the degree of

Doctor of Philosophy

05. 29. 2020

Head of Committee Prof. Hochun Lee   _____ (인)
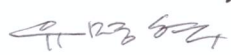
Committee Member Prof. Seung-Tae Hong   _____ (인)

Committee Member Prof. Kang Taek Lee   _____ (인)

Committee Member Prof. Myung-Hyun Ryou   _____ (인)

Committee Member Prof. Yong Min Lee   _____ (인)

Ph. D/ES
201734002

아피아, Williams Agyei Appiah, Analysis and Modeling of Capacity Fading in Lithium Ion Batteries, Department of Energy Science and Engineering, 2020, 201 pages, Advisor Prof. Yong Min Lee, Co-Advisor Prof. Myung-Hyun Ryou.

Abstract

The distinctive intrinsic electrochemical characteristics of lithium ion batteries (LIBs) have made them a suitable energy storage device for many electrical storage applications such as electric vehicles (EVs) and energy storage systems (ESS). Yet, concerns about the mileage requirement, reliability and safety of LIBs for EV application remain a major drawback. To meet the mileage requirements, there is the need to increase the energy density of LIBs for EVs. This can be achieved by replacing the conventional cathode and anode active material with a higher energy density active material. However, these materials suffer from severe capacity fade. The physical and chemical degradation mechanisms for the severe capacity fade are diverse, complicated and interdependent, and very difficult to understand. Yet, there are limited reliable and practical methods for detecting, predicting and quantifying these degradation phenomena.

This thesis presents a non-destructive capacity-fading analysis method to identify the various degradation mechanisms of high energy density active materials for Li ion cells. The key objective of this method is the extraction of information on degradation from physics-based model parameters that changes with cycling via a parameter estimation technique.

Comprehensive capacity-fading models; physico-chemical and chemo-mechanical model, are then developed to describe and quantify the identified degradation mechanisms. The developed capacity fade models are used to study the nature of different cell design parameters and adhesive strength on the specific capacity and stability of Li ion cells. A time-effective accelerated capacity fading analysis method for Li ion batteries is proposed using the developed physico-chemical model and a pseudo-two-dimensional model. The developed capacity fade models improve the prediction and quantification of the degradation mechanisms of high energy density electrode active materials. This will enhance the effective integration of high energy density electrode active material into LIBs and thereby resolve the issues related to mileage requirement and reliability of LIBs for EVs. The findings presented in this work is of both technological and commercial interests.

Publications

The work presented in this thesis is partly covered by the following publications.

[1]. W. A. Appiah, M.-H. Ryou, Y. M. Lee. A physics-based model capacity fade analysis of LiMn$_2$O$_4$/graphite cell at different temperatures. *Journal of the Electrochemical Society,* **2019**, *166*, 5109.

[2]. W. A. Appiah, J. Park, S. Byun, M.-H. Ryou, Y. M. Lee. A mathematical model for cyclic aging of spinel LiMn$_2$O$_4$/graphite lithium-ion cells. *Journal of the Electrochemical Society,* **2016**, *163*, 2757.

[3]. W. A. Appiah, J. Park, S. Byun, Y. Roh, M. Ryou, Y. M. Lee. Time-effective accelerated cyclic aging analysis of lithium-ion batteries. *ChemElectroChem* **2019**, *6*, 3714.

[4]. W. A. Appiah, D. Kim, J. Song, M. Ryou, Y. M. Lee. Understanding the effect of polydopamine interlayer on the long-term cycling performance of silicon anodes: A multiphysics-based model study. *Batteries & Supercaps* **2019**, *2*, 541.

[5]. W. A. Appiah, J. Park, S. Byun, I. Cho, A. Mozer, M.-H. Ryou, Y. M. Lee. A coupled chemo-mechanical model to study the effects of adhesive strength on the electrochemical performance of silicon electrodes for advanced lithium ion batteries. *Journal of Power Sources* **2018**, *407*, 153.

[6]. W. A. Appiah, Y. Roh, C. B. Dzakpasu, M.-H. Ryou, Y. M. Lee. Design of thin-film interlayer between silicon electrode and current collector using a chemo-mechanical model. *Journal of the Electrochemical Society,* **2020**, *167*, 080542.

[1] presents a non-destructive capacity fading analysis method for spinel-based cathode and graphite anode which was presented in Chapter 2. Contributions of the co-authors are limited to general advice on the work.

[2] describe the physico-chemical degradation model developed for the spinel- based cathode and graphite anode presented in Chapter 3. Contributions of the co-authors are limited to general discussions and feedback on the work. The work was also presented at the PRIME 2016 in Honolulu, Hawaii, USA.

[3] applies the physico-chemical degradation model in Chapter 3 to propose a time-effective accelerated capacity fade analysis framework for LIBs and forms the basis of

Chapter 4. Contributions of other researchers are limited to general advice and feedback on the work.

[4] extends the capacity fade analysis method demonstrated in Chapter 2 to high volume expansion anode materials with a bare and polydopamine-treated copper current collector and it is presented in Chapter 5. Contributions of other researchers are limited to the manufacturing of coin cells with various electrode designs and general feedback on the work.

[5] utilizes the identified degradation mechanisms in Chapter 5 to design a chemo-mechanical model to study the influence of adhesive strength on high volume expansion anode materials which forms the basis of Chapter 6 and Chapter 7. Contributions of co-authors are limited to general advice and feedback on the work.

[6] extends the chemo-mechanical degradation model to include kinetic properties of the thin-film interlayer and SEI, and it is presented in Chapter 6 and 7. Contributions of other researchers are limited to general advice and feedback on the work.

Table of contents

List of figures

List of tables

Nomenclature

a specific surface area, m^{-1}

c concentration, $mol\, m^{-3}$

D diffusion coefficient, $m^2\, s^{-1}$

E_a activation energy, $J\, mol^{-1}\, K^{-1}$

F Faraday's constant, $96487\ C\, mol^{-1}$

I_{app} applied current density, $A\, m^{-2}$

i_{os} exchange current density for side reaction, $A\, m^{-2}$

j pore wall flux of lithium ions, $mol\, m^{-2}\, s^{-1}$

j_s local volumetric current density for side reaction, $A\, m^{-2}$

k electrochemical reaction rate constant, $m^{2.5}\, mol^{-0.5}\, s^{-1}$

k_0 frequency factor, s^{-1}

L thickness of battery component, m

M molecular weight, $mol\, kg^{-1}$

r radial coordinate, m

R ideal gas constant, $8.3143\ J\, mol^{-1}\, K^{-1}$

R_{film} film resistance at the electrode/electrolyte interface, $\Omega\, m^2$

R_P resistance of the film products, $\Omega\, m^2$

t time, s

t_+ cation transference number

T temperature, K

U equilibrium potential, V

x main dimension across the cell sandwich

Greek symbols

ε volume fraction

η local over potential, v

κ electrolyte conductivity, $S\,m^{-1}$

σ electrode conductivity, $S\,m^{-1}$

ρ density of active material, $kg\,m^{-3}$

δ_{film} film thickness, m

ϕ electric potential, v

Subscript

1   solid phase

2   liquid phase

e   electrolyte

n   negative electrode

p   positive electrode

P   Side reaction product

−   to the left of an interface

+   to the right of an interface

s   side reaction

Chapter 1

Introduction and literature review

1.1 Introduction

Micro hybrids, mild hybrids, plug-in hybrids (PHEVs) and all-electric vehicles (EVs) powered by battery systems are the major alternatives being offered in the vehicle market. A micro hybrid vehicle is a system the uses the start-stop technology. This enables the vehicle to be ignited by the battery pack, trap energy to be stored in the battery during breaking and be able to support the electrical systems when the internal combustion engine (ICE) is shut off. The mild hybrid is like the micro hybrid with additional components. These components are an electric motor/generator in parallel with the ICE. The electric motor/generator assist the vehicle when coasting and breaking. There is no electric-only mode of driving in the mild hybrids, even though they can assist the ICE. PHEVs has the same characteristics as the mild hybrid vehicles with the ability to plug into electric grid as well as having an electric-only mode of driving [1]. Consumer interest, technology, cost, regulatory requirements and a variety of government incentives are the factors that controls the hybrid and electric vehicle markets. The features of battery systems such as cell chemistry, power density, energy density, cycle life and operating conditions influence all these factors. The type of cell chemistry is extremely relevant as it controls the inherent safety, battery design, shelf life, reliability and so on. Figure 1.1 [2] shows the comparisons of various cell chemistries together with their miles per charge and target.

Pb-acid batteries are relatively cheaper among the existing automotive battery systems; however, they are composed of toxic materials and shows a lower energy density [3]. Compared to Pb-acid batteries, Ni-Cd batteries exhibits higher energy and power density values, but Cd anode is toxic and expensive. Ni-MH batteries are relatively better than Ni-Cd batteries in terms of power and energy densities with non-toxic MH anode. However, they require complex charging protocols and they have high self-discharge issues. LIBs are comparatively more expensive than the other cell chemistries, but they deliver the highest energy and power densities as well as longer cycle life [4–6]. Nevertheless, there are still issues related to the mileage requirement, safety and warranty.
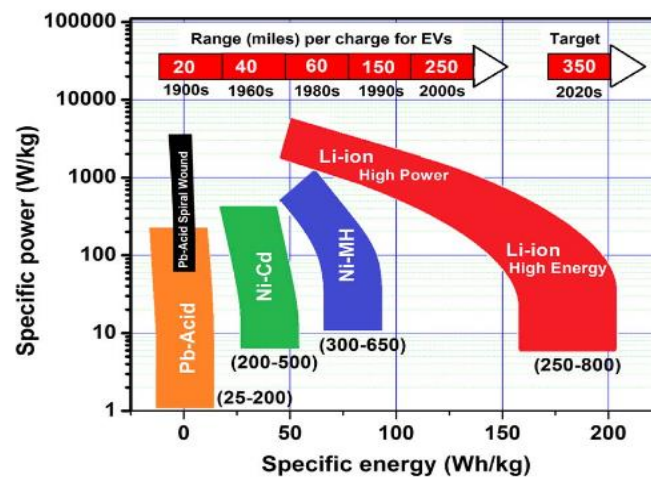
Figure 1.1. Ragonne plot of various cell chemistries and their miles per charge as well as target. The number s in the parenthesis is the price (USD) for the particular cell system per kWh [2].

The mileage of current EVs is ca. 250 miles per charge, which is less than the mileage of ICEs. To take on ICEs, the driving range of EVs should be increased to ca. 350 miles per charge by 2020 [2]. To increase the mileage requirements of EVs, there is the need to increase the energy density of LIBs. The energy density of LIBs is influenced by many factors at the battery pack, cell, electrode and material level. These factors include the effect of

components such as the electrolyte, separator, electrode, amount of inactive material, cell and battery design. The energy density required for a driving range of 350 miles at the battery pack level is 70 to 80 kWh for similar EV models available in the market. To meet the mileage requirement of EVs, the energy density of LIBs should be improved at all levels as presented in Figure 1.2 [7].
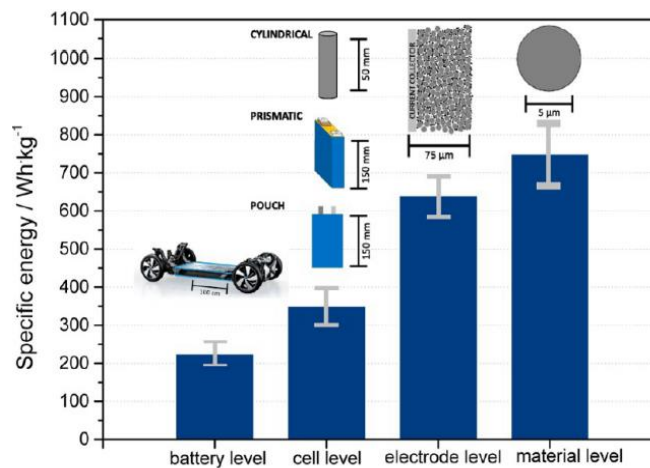
Figure 1.2. Specific energy density from pack to materials level alongside design steps for battery packs [7].

The energy density at materials level is first translated to a full electrode level, where electrode design parameters such as porosity, thickness and composition are needed. These electrode design parameters are function of the specific properties of the active material such as particle size and conductivity. At the cell level, a suitable cell type and size, number of jellyrolls and suitable cathode and anode should be selected. Prismatic hard case, cylindrical and pouch cells are the three main cell formats used for EVs application. Even though cylindrical cells delivers higher energy densities because a stacked cell assembly is in a cylindrical cell is wound with higher tension, prismatic and pouch cells are used for a wide range of automotive applications owing to easier customization of their size for the final product. Finally, to achieve practical voltages (usually between 200 and 400 V) and required

capacities for EVs application, appropriate strategies must be selected to connect the individual cells to battery modules and battery packs. From Figure 1.2, an energy density of 750 Wh kg^{-1} at the materials level is required to achieve an energy density of 300 Wh kg^{-1} at the battery level. Thus, the choice of active material has a profound effect on enhancing the energy density of LIBs for EV applications.

Currently, natural and artificial graphite is the main anode-active material in LIBs [8,9] and act as a universal reference in assessing new materials. However, to improve the energy density of LIBs, graphite must be replaced with higher-specific-capacity alternatives such as Si. Si is one of the most promising anode material owing to its high theoretical capacity (>4000 mAh g^{-1}) and lucrative operating voltage (~0.3 V versus Li/Li$^+$) [10–12]. However, Si suffers from severe capacity fade due to huge volume change upon (de) lithiation leading to failure modes such as pulverization, delamination and formation of unstable solid electrolyte interphase (SEI) as shown in Figure 1.3 [13]. Considerable efforts have been focused on combating these key failure modes. Progress has been achieved in this area by using smart electrode structures [14–16] and binder designs [17–19]. Smart electrode structures such as porous carbon [15,20,21], graphene [16], tubular templates [22] and other semiconducting materials [23] with similar morphologies buffer the volume expansion in Si through conductive nanoporous structures. Replacement of conventional polyvinylidene difluoride (PVDF) with new binders such as polymers with crosslinked chains [17,24], self-healing polymeric matrices [18,19], carbohydrate-based polymers and electronically conducting polymers adequately maintain the electrode structure during iterative volume changes of Si. The use of smart electrodes and binder designs simultaneously resolves issues related to pulverization and delamination of the active material. The problem related to the formation of unstable SEI can be largely resolved by a circumspective selection of electrolyte solution

[25–27]. Even though, these progresses have been made, the commercialization of Si is still at a halt, owing to limited understanding of the capacity fading mechanisms and more limited is a way to quantitatively assess and identify capacity-fading mechanisms.
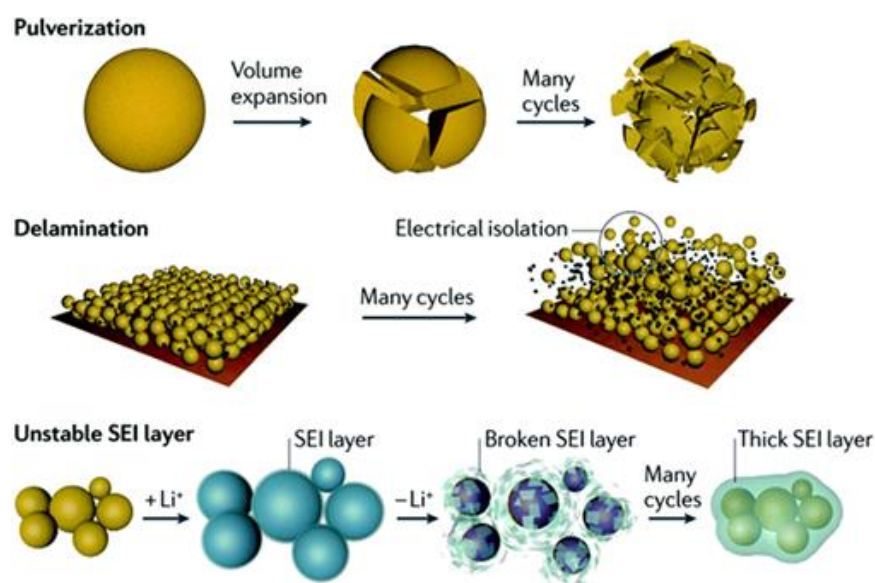
Figure 1.3. Degradation mechanism of Si anodes due to large volume expansion during lithiation [13].

Ni-rich and Li- and Mn-rich layered materials are the next prominent cathode materials in the field of LIBs. These materials originated from the early works by Dahn [28] and Thackeray [29]. They are the successive generation of their well-established layered counterparts, $LiCoO_2$ (~145 mAh g^{-1}) and $LiNi_{1/3}Co_{1/3}Mn_{1/3}O_2$ (~153 mAh g^{-1}) [30]. Ni-rich $LiNi_xCo_yMn_zO_2$ or $LiNi_xCo_yAl_zO_2$ (x +y + z = 1) layered cathode materials in which $x>0.6$, have higher relative specific capacity because of their electronic structures, as with $LiNiO_2$; in contrast to $LiCoO_2$, the energy band of $LiNiO_2$ does not overlap with the O_{2p} band [31], permitting a higher degree of charging without distorting the O_2 framework. The specific capacity of Li- and Mn-rich cathode materials is higher than 250 mAh g^{-1}. This capacity is achieved owing to the presence of Li_2MnO_3 which is activated in the first charge during Li extraction and O_2 evolution at a potential of >4.7 V [32]. However, these two materials suffers

from severe capacity fade during cycling because of the transformation of the layered structures to a more thermodynamic stable spinel-like phases upon the extraction of Li-ion during charging [33]. The transition is due to the preferential migration of transition metals (TMs) to the octahedral sites in the Li slabs (Li-TM mixing) [34] (Figure 1.4 [13]) leading to a drop in both the discharge voltage profile and capacity, and the dissolution of TMs resulting in irreversible and inactive interfacial compounds [31]. In addition, formation of resistive surface films that increases the electrode impedance during the interaction of nucleophilic and basic cathode materials with solution species also contributes to the severe capacity fade [35]. To combat these degradation mechanisms, strategies such as TM doping [36–38], surface coating with AlF_3 [39], Al_2O_3 [40,41], $AlPO_4$ [42], and the incorporation of concentrated gradient structures [43].
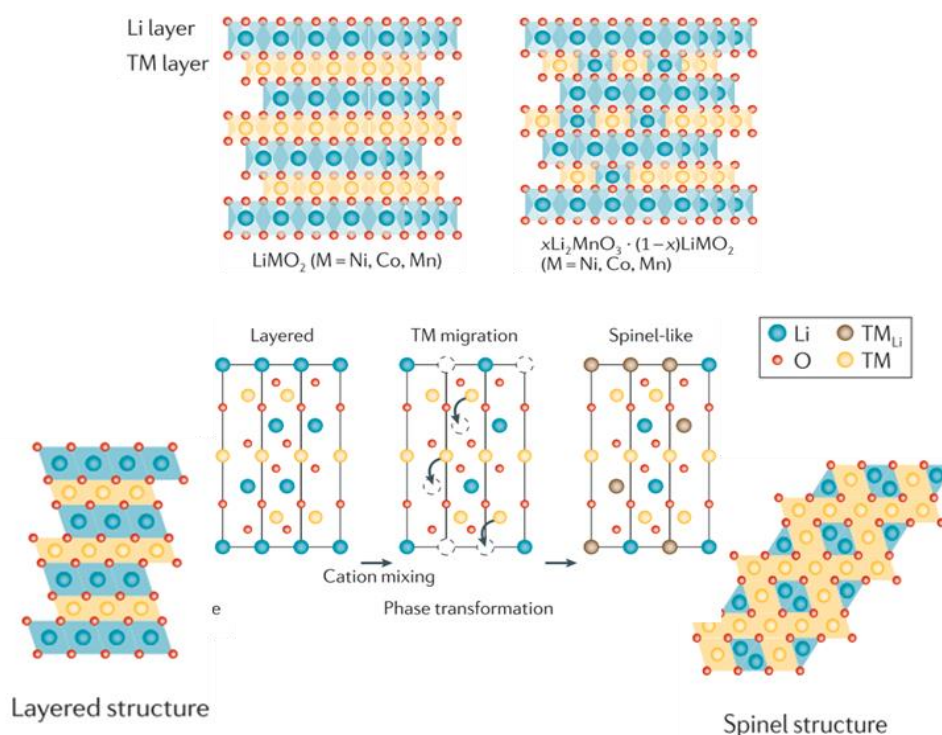
Figure 1.4. Layered-to-spinel transformation upon charging of Ni-rich and Li- and Mn-rich cathode materials [13].

For effective integration of high energy density electrode active material into LIBs, and prognostics and health management (PHM) analysis of LIBs, knowledge about the capacity-fading mechanisms under certain operating conditions is vital [44,45]. There are two existing methods for studying the capacity-fading mechanism of LIBs [46]:

1. Post-mortem method: This method involves the physico-chemical analysis of disassembled aged batteries using advanced instruments and test methods (such as scanning electron microscope (SEM), X-ray diffraction (XRD), transmission electron microscopy (TEM), X-ray photoelectron spectroscopy (XPS) among others).

2. Battery performance-based analysis method: This is a non-destructive method, which employs electrochemical voltage spectroscopy (EVS) to analyze the capacity fade and increase in resistance. It also involves the analysis of the capacity-fading mechanism using identified model parameters.

Post-mortem analysis methods are reviewed in section 1.2 and battery performance-based analysis method in section 1.3. Identified capacity-fading mechanisms are modeled to predict and study the effect of design parameters on the long-term cycling performance. Section 1.4 present a review on capacity fade modeling. The focus and aims of this work are discussed in section 1.5. This chapter is terminated with an outline of the thesis.

1.2 Post-mortem analysis methods

Samples for physico-chemical analysis methods can originate from anode, cathode, separator, current collector, or the electrolyte. Different parts of a solid sample can be differentiated: electrode surface, bulk, cross-sections, and different analysis methods can be allocated to them, respectively. Surface sensitivity analysis are related to the physical nature of the involved types of radiation or particles. They are produced either by reflection of radiation/particles on the surface of the sample due to short mean free paths of particles inside the solid samples. Representative surface sensitive methods are microscopy, EDX, XPS, IR or SIMs. Other methods are not surface sensitive and includes information from the bulk electrode. Examples are ICP-OES analysis and XRD analysis.

Optical microscopy.—Optical microscopy is used to detect capacity-fading effects such as changes in electrode thickness[47] or depositions on electrode surfaces which are in µm size range [47,48]. Brand et al. [49] used optical microscopy to observe the scorching of a separator after shaking tests of 18650 cells. In situ analysis via optical microscopy has been used to study Li deposition and dendrite formation during charging process [50–52], and color changes in graphite [53] and rutile [54] electrodes . Optical microscopy have been successful utilized in the development of new materials: determination of fracture energy of lihtiated Si thin-film electrodes as a function Li ion concentration [55], and the effect of silica nanoparticles added to gel electrolytes to prevent Al current collector corrosion [56].

Scanning electron microscopy. —Scanning electron microscopy (SEM) deliver improved resolution compared to optical microscopy. SEM has been used to study the growth of solid electrolyte interphase (SEI) on the negative graphite electrode [47,57,58]. The capacity fade due to the growth of SEI is related to the decomposition of electrolyte resulting

in loss of Li ions [59,60]. Honbo et al. [61] studied Li deposition on graphite using SEM and undiscovered dendritic and granular morphologies on pristine and grinded carbon, respectively. Zier et al. [62] revealed that it is possible to enhance the material contrast of Li deposition on graphite electrode by reaction with OsO_4. Studies conducted on other anode materials such as $Li_4Ti_5O_{12}$ by SEM has so far not given precise information on degradation mechanisms [63]. Mechanical stress due to volume changes in the cathode material during cycling results in cracks in the particles, which are observable by SEM [64,65]. Degradation of other cell components such as corrosion of Al current collectors [66,67] and pore-closure [68,69] or melting of separators are discoverable by SEM.

Transmission electron microscopy.—Transmission electron microscopy (TEM) uses higher acceleration voltages for electrons, permitting transmission through materials and a higher resolution down to the atomic scale as compared to SEM [62,70]. TEM has been used to investigate the structural changes in particle morphology arising from calendar and cycling aging for $LiNi_{0.8}Co_{0.15}Al_{0.05}O_2$ cathode material [71]. Relevant insight regarding binder dependency on cell performance, SEI formation cathodes and evaluation of new electrode materials have been provided by TEM. Usage of TEM is shifting from a post-mortem analysis method to an in situ and operando technique [72].

1.2.1 Surface sensitive chemical analysis methods

Energy dispersive X-ray spectroscopy.—Energy dispersive X-ray spectroscopy (EDX) is often combined with SEM devices to provide information on the chemical composition of the active materials and to detect the presence of additional phases such as detection of redeposited dissolved Mn on top of graphite from $NMC/LiMn_2O_4$ blended cathodes [57,59]. Similarly, Klett et al. observed Fe on anodes after dissolution from $LiFePO_4$ cathodes [73].

The presence of F and P on anodes due to the decomposition of the electrolyte [57,74]. EDX mapping permits the detection of O and C suggesting the formation of Li_2CO_3, however, a further analysis using FTIR and XRD for verification was required [75]. Maleki et al. [76] investigated the effects of deep discharge below the end-of-discharge voltage for commercial $LiCoO_2$/graphite cells using EDX. The authors discovered that, discharging to 0 V can lead to dissolution of Cu from the negative current collector which is detected on both anode and cathode.

X-ray photoelectron spectroscopy.—X-ray photoelectron spectroscopy (XPS) has been used to detect the possibility of catalytic reactions occurring at the electrolyte graphite interface [77]. Lu et al. [78] performed XPS surface and depth profiling analyses and observed an increase of the SEI thickness in aged cells. Using XPS, Ehrenberg's group were able identify the constituents of the outer and inner layers of SEI in a commercial pouch cells, but was not able to discern into the differences in SEI characteristics for different formation procedures [79]. Zheng et al. [80] used post-mortem XPS to confirm that newly formed layers of Li_2CO_3 and LiF on the anode surface were the reason for the significant increase in bulk resistance and charge transfer resistance when they studied the degradation of commercial $LiFePO_4$/graphite cells. Post-mortem XPS was used by Feng et al. [81] to identify the main problem of Li-S cells which is the accumulation of S species on the electrode surfaces resulting in capacity fade.

Fourier transforms infrared spectroscopy.—Fourier transform infrared spectroscopy (FTIR) samples from Post-Mortem analyses have been conducted aiming to tackle differences when using electrolyte additives [82,83]. In these cases, both anodes and cathodes were studied. Likewise, FTIR results are used to compare SEI characteristics when changing the Li-based salt [84]. Norberg et al.[85], studied $LiNi_{0.5}Mn_{1.5}O_4$-based cathodes cycled with 1

M LiPF6 in EC/DEC mixture. After cycling, FTIR tests unveiled characteristic bands of alkyl carbonates along with bands at 1310 cm^{-1} and 1110 cm^{-1} assigned to C-O and C-C stretching modes in ketones, which evidence of electrolyte de- composition on the cathode surface. Nevertheless, the identification of the specific decomposition compounds was not possible with this technique. Other Post-Mortem surface chemical sensitive analysis methods include secondary ion mass spectroscopy (SIMS) and glow discharge optical emission spectroscopy depth profiling (GD-OES).

1.2.2 Bulk electrode chemical analysis methods

Inductively coupled plasma optical emission spectrometry— In Post- Mortem analyses, inductively coupled plasma optical emission spectrometry (ICP-OES) is used to determine the elemental composition of electrodes. ICP-OES measurements are relevant in proving dissolution of transition metals from the cathode by detecting the migrated material on the anode. This dissolution was shown to contribute to the capacity-fading mechanism of the anode [47,57,59] and is caused by HF [86,87]. Stiaszny et al.[47], observed transition metal concentrations of fresh and aged anodes of LiMn$_2$O$_4$-NMC/graphite cells with ICP-OES which was confirmed by the decrease in peak height of the NMC peak in the cyclic voltammetry. The Mn on graphite anodes dissolved from NMC/LiMn$_2$O$_4$ blend cathodes was found to increase with temperature [57,59] and time [59] by ICP-OES. Another capacity-fading mechanism studied by ICP-OES is the growth of SEI limited to the elements Li, P, and Mn and sup- ported by EDX [57,59].

Nuclear magnetic resonance spectroscopy.—Nuclear magnetic resonance (NMR) spectroscopy is a powerful method that characterize materials and chemical compounds in solid state and in solvents [88]. It also provide information about transport properties and

mobility of ions, electronic, magnetic, as well as thermodynamic and kinetic properties [89,90].

According to Delpuech et al.[91], the high irreversible capacity loss of Si- based anodes originates from the degradation of the carbonate solvents followed by the formation of non-lithiated carbon species in oligomeric or polymeric form. Grey and co-workers [92] showed that the capacity loss and self-discharge is directly linked to structural changes in Si anodes and can be avoided by the correct choice of binders. DeSilva et al.[93], studied SEI formation on $LiNi_{0.80}Co_{0.2}O_2$ cathodes and MCMB-(1028)-carbon anodes by 7Li, 19F and 31P solid state MAS NMR. In case of the cathode, the authors could determine different amounts of irreversible Li concentrations for the same nominal electrochemical SOC after cell disassembly. Furthermore, they could show that additive decomposition and deposition occurs on the cathode.

1.2.3 Electrolyte analysis methods

Electrolyte degradation occurs due to side reactions that provide insoluble, soluble and gaseous products [87,94]. Detection of such products is fundamental to trace back the side reactions responsible for capacity fading in LIBs. Thus, many studies have implemented techniques to analyze electrolytes and gases generated during battery aging. Chromatographic techniques have proven to be very successful in Post-Mortem electrolyte characterization.

Gas Chromatography (GC) coupled with a thermal conductivity detector (GC-TCD) enabled the observation of H_2, CO, CO_2, CH_4, C_2H_4, C_2H_6 and C_3H_8 upon the first charge. To gain insights in the formation mechanism of alkyl dicarbonates, Sasaki et al.[95], carried out Post-Mortem GC-mass spectrometry (GC-MS) analyses of electrolyte recovered after cycling of Li / graphite half-cells. The presence of alkyl dicarbonate was confirmed, and

parallel chemical simulations signaled that Li alkoxides could trigger the alkyl dicarbonate formation.

Laruelle et al.[96] performed Post- Mortem electrolyte and gas analyses on lab scaled cells. The authors used Electro Spray Ionization coupled with High Resolution Mass spectrometry (ESI-HRMS) and GC-MS for analyzing the electrolytes, though a different set of capillary columns was used for GC- MS analyses of the stemmed gas. The parallel use of these techniques permits the detection of compounds on a wide mass range, thus a global electrolyte degradation mechanism was elucidated [97,98]. The authors discovered that most degradation compounds are derived from the linear carbonate reduction, which provide the Li alkoxides that further trigger the electrolyte esterification, while the two-step reduction of EC was less important.

Recently, the GC-FTIR-MS equipment was used to analyze the gases from a swollen commercial cell. The gas recovery was performed in an Ar-filled glove box by piercing the pouch cell bag with an air-tight syringe. The authors identified CO, CO_2, CH_4 and C_3H_8 in the GC/FTIR Gram-Schmidt graph. The GC/MS chromatogram allowed the detection of other less abundant volatile compounds. Complementary GC-MS electrolyte analyses allowed the detection of alkyl dicarbonates and longer carbonate chains, as well as organophosphate compounds, which indicated that water traces present in the commercial cell play a role in the electrolyte decomposition [99].

1.3 Battery performance-based analysis methods

Battery performance analysis methods is less complex and non-destructive. A wealth of information on the capacity-fading mechanisms of LIBs can obtained from this method. The two main battery performance-based analysis methods are the electrochemical voltage spectroscopy (EVS), and identification and tracking of model parameters.

1.3.1 Electrochemical voltage spectroscopy

The state of health (SOH) of cells can be obtained by direct monitoring of the changes in capacity and power retention; however, cell diagnosis is not achievable due to the limited accessible information on the capacity-fading mechanisms. Likewise, capacity and power tracking are not recommended for prognosis either. Such information is traditionally obtained through post-mortem analysis[100], however previous studies in recent years has proven otherwise. That is, it is possible to obtain the capacity-fading mechanisms from data collected during capacity tests because the voltage response of a cell changes during cycling due to the changes in the balance between the cathode and anode [101,102]. The changes in the voltage response can also be related to variations in the electrochemical reactions, which occur on either electrode [103]. Hence, information on the thermodynamic state and on the kinetics of the cell can be obtained by tracking and studying the changes in these voltage profiles. This permits the diagnosis and prognosis of the cell.

The incremental capacity (IC), or $dQ/dV = f(V)$, was first applied to Li metal cells by Thompson [104] in the late 1970s. IC was introduced to enable the visualization and quantification of the minute changes in the voltage profiles associated with a change in electrode balance or a change in electrode signature on the classic voltage (V) vs. capacity

(Q) curve. IC was efficient and less complex for analyzing voltage profiles of half-cells as it was adopted to identify potential electrodes for Li-ion cells with IC signature for graphite [105–107] and cathode materials [108–110]. However, the analysis of full-cell signature was complex and only little qualitative or quantitative information was readable as reported by Barker et al. [111] and the Berkeley National Laboratory [112]. To solve this issue, Bloom et al. [113] introduced another derivative method, differential voltage analysis (DV) or $dV/dQ = f(Q)$. Dubarry et al. [114] proposed a methodology to index IC curves which enabled the full qualitative and quantitative analysis of ageing of both half and full cells. Both IC and DV techniques have been adopted and accepted as valid alternatives to post-mortem techniques to characterize commercial cells [115].
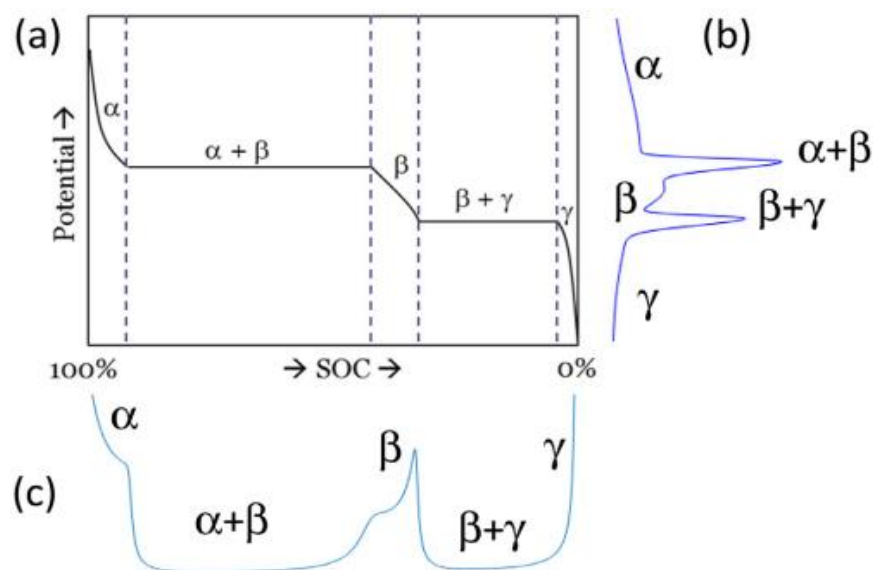
Figure 1.5. Correlation between (a) voltage profile and derivatives profiles (b) IC and (c) DV. [116]

Both IC and DV analysis are based on the study of the changes in the voltage profiles of a cell. Because of differences in chemical composition and/or crystallographic structure, all active electrode materials have a different thermodynamic voltage profile with a different set of voltage plateaus and regions where the voltage varies with composition. The voltage

response of a hypothetical material, M, undergoing a lithiation to LiM and the two derivatives of interest with IC and DV are shown in Figure 1.5a, 1.5b and 1.5c respectively [116]. From Figure 1.5b, it can be observed that, for IC curve, the main focus is the phase transformations corresponding to the voltage plateaus while for the DV curves, the main focus is on the single-phase regions with peaks for solid solutions. In theory, both IC and DV curves provides the same information since they are both derived from the same voltage, however IC curves are more preferable for identifying the capacity-fading mechanisms of blended active materials owing to the additive contribution of both active materials to the voltage profile. This is different for DV curves and modeling will be required to analyze the different contributions.

The capacity fading of Li-ion cell is complex and that many capacity-fading mechanisms can occur throughout the life of a cell depending on the operating conditions. These capacity-fading mechanisms are well described in literature [117]. Large amount of test is required to quantifying all of these mechanisms individually and likely some relevant post-mortem analyses [100]. Compared to these sophisticated tests, EVS analysis cannot provide such accuracy and details; however they can be used to gather information on degradation modes [116]. The capacity-fading mechanisms can be classified into one or several of three categories or degradation modes depending on how they affect electrochemical behavior of the cell [101]. Some capacity-fading mechanisms affect the amount of active material available for electrochemical reaction (e.g. dissolution or grain isolation) and thus can be classified as LAM. Others consume Li ions from parasitic reactions (e.g. SEI layer growth and inactive species precipitation) and thus can be classified as LLI. Lastly, some capacity-fading mechanisms change the ohmic resistance of a cell (e.g. corrosion of the current collectors) and alter the kinetics of the cell (e.g. growth of passivation layers). These three

degradation modes can be quantified using EVS because they change the balance between the PE and the NE (which may lead to further LAM). Bloom et al. [113] explained how to interpret DV changes and relate them to the different degradation modes. Dubarry et al. [118] attempted the same classification for IC curves by considering a Li-ion cell as a communicating vessel problem. Experimental validation supporting both approaches (DV and IC curves) for quantification of LLI and LAM degradation modes has been presented in previous reports [119–121].

1.3.2 Identification and tracking of model parameters

Another battery performance-based capacity fading analysis method is to analyze the electrochemical mechanisms using identified and tracked model parameters. There are two types of battery model: the equivalent circuit model (ECM) and electrochemical models. The study of state of health (SOH) of Li ion cells using the ECM was introduced by [122]. A novel SOC estimation method based on the model adaptive extended Kalman filter (MAEKF) was proposed by Sepasi et al. [123] to update battery model of aged cells and estimate SOC accurately. Guo et al. [124] introduced an SOH estimation method based on a simple EMC approach to parameterize a single-variable, time-based SOH inference model using CC charging profiles at various stages of life. The simplicity and accuracy of this approach in estimating SOH makes it easy for on-board applications without sophisticated experiment schedules. This makes the EMC-based capacity fade analysis attractive for practical applications. However, the model parameters are lumped circuit parameters and are hardly used for capacity-fading mechanism analysis, which is different from rate of capacity fade analysis, which can be studied through SOC and SOH estimation.

Electrochemical models on the other hand can handle the complex mechanisms of physical and chemical processes, such as diffusion, transport of ions, ohmic phenomena, electrochemical reaction and thermal behaviors [125–127]. They have a large set of parameters with corresponding physical meaning, which makes them appropriate for the analysis of capacity-fading mechanisms. Identification and tracking of electrochemical model parameters for characterizing capacity-fading mechanisms has gained a lot of attention in on recent years. The capacity-fading mechanisms of Li ion cells with different cathode active materials and graphite-based anodes were investigated based on the changes in the SOCs of the electrode material [128–130]. Schmidt et al. [131] studied the correlation between the volume fraction of active material in the electrode (ε_s), the ionic conductivity of the electrolyte (κ_e) and the cycle number during aging. The authors used the changes in these model parameters to characterize the SOH of Li ion cells. Ramadesigan et al. [132] observed that both the electrochemical reaction rate constant (k_s) and the Li-ion diffusion coefficient constant (D_s) in the anode fades exponentially with cycle number. Fu et al. [133] treated the volume fraction of active material in the electrode (ε_s), the solid electrolyte interface (SEI) resistance (R_{film}) and the diffusion coefficient constant of the electrolyte (D_e) of an electrochemical thermal model as capacity fading parameters to analyze the degradation effects on the side reactions. Zhang et al.[46] analyzed the capacity-fading mechanisms and increase in the internal resistance of an $LiCoO_2$/graphite batteries via electrochemical model parameters identification and tracking.

1.4 Capacity fade modeling

The capacity-fading mechanisms in Li –ion batteries originate from complex coaction of physical and chemical mechanisms, perpetuated by environmental conditions, usage patterns, and operational history. The individual cell components: the electrodes, the separator, the electrolyte and the current collectors, are affected by different degradation mechanisms [87,107,134]. The most frequently reported capacity-fading mechanisms are presented in Figure 1.6 [119].
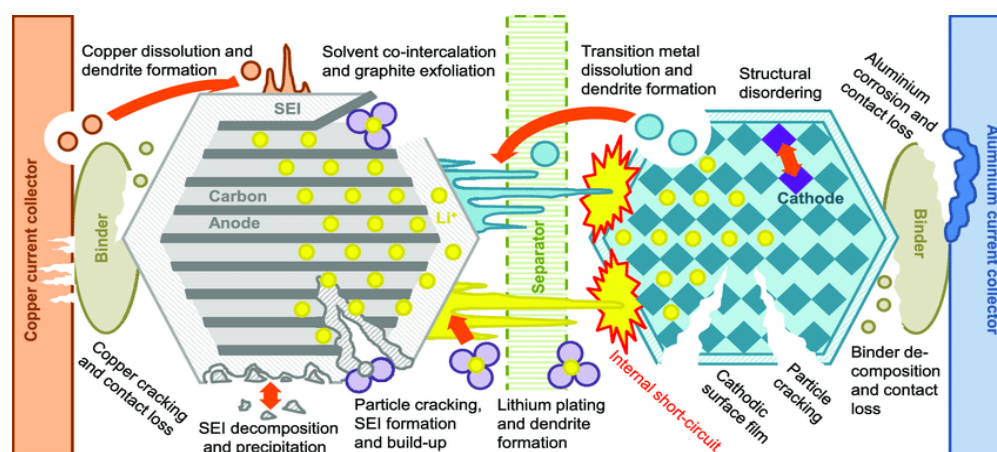
Figure 1.6. Degradation mechanisms in Li-ion cells [119].

The inter-dependencies, different causes and rates, and complexity of the capacity-fading mechanisms pose great challenges to attempt to model or identify capacity-fading mechanisms in Li-ion cells. To tackle the issues related to capacity fading modeling, two main approaches have been proposed: the empirical model approach and the physics-based model approach.

1.4.1 Empirical modeling method

There are two general types of empirical methods for identifying and quantifying capacity-fading mechanisms in Li ion cells. These are the data-driven methods and the on-line state estimators.

1.4.1.1 Data-driven methods

Data-driven methods normally depends on large sets of experimental data obtained by operating the Li-ion cells in harsh operating conditions. The obtained data from such experiments can thus be used to establish relationships between environmental and operational conditions and the symptoms of degradation, such as capacity and power fade.

Bloom et al [135] applied this method to model power fade by fitting experimental data obtained at different temperatures to the equation

$$Q = A \cdot \exp\left(\frac{-E_a}{RT}\right) t^z \tag{1.1}$$

where Q is percentage power loss, A is pre-exponential factor, E_a is activation energy, R is gas constant, T is absolute temperature, t is time and z an empirically determined exponent. Wang et al. [136] modified Eq. 1.1 to include current rate by substituting time with Ah-throughput, which represents the amount of charge inserted/extracted during cycling. The authors obtained good results for the stress factors they considered however, they did not consider the effects of other stress factors such as different cut-off voltages and charge rate, or combinations of stress factors.

Li et al. [137] developed a cycle life model, which considers stress coupling between temperature, cycling rates, end-of-charge and end-of-discharge voltages, and showed that

coupling effects have a non-negligible impact on capacity fading above certain stress levels. This methodology requires extensive test regimes for every new cell type, which consumes a lot of time. Safari et al. [138] devised a capacity fade model based on the principles of mechanical fatigue prognostic theory and validated it against simulated ageing data, produced by a physics-based battery model, which assumes SEI growth as the only capacity-fading mechanism. Validating the model with an existing model saves time and resources compared to validating with experimental data; however, the model being validated is only as good as the existing model. Since the physical model used is based on SEI formation, the validated model developed for predicting capacity fade by Safari et al. [138] can only be used to model SEI formation and not capacity fade in general, which could also be caused by other mechanisms.

He et al. [45] developed an empirical model for capacity fade

$$Q = a \cdot \exp(b \cdot k) + c \cdot \exp(d \cdot k) \qquad [1.2]$$

where Q is the cell capacity, k is the cycle number, a and b are empirical parameters related to the impedance and c and d are empirical parameters representing the ageing rate. The model is fitted to the experimental cycle performance. Equation 1.2 can be used for predicting the end-of-life of Li ion cells via extrapolation of the model parameters. Similar data-driven methods based on empirical capacity fade models have presented in previous reports [139–141]. The advantage of the above methods is that modeling and predicting the effects of degradation on performance of the does not necessarily require knowledge of the underlying physical and chemical mechanisms and specific composition of the cells. However, large sets of experimental data are required to obtain accurate predictions. The acquisition of such data sets is time consuming and expensive, and the data are highly

specific to a certain type of Li-ion cells and do not necessarily reflect real-life usage if recorded in laboratory conditions. On the other hand, data-driven models trained on large data sets may be well suited to predict gradual changes in capacity or power capability of the recorded data. However, such models are unlikely to accurately predict the end-of-life of individual cells whose ageing behavior deviates significantly from that of the average cell [41]. Nevertheless, knowledge of underlying capacity-fading mechanisms is critical to identify potential safety hazards and improve the performance of the cell.

1.4.1.2 On-line state estimators

On-line state estimators are usually composed of simple dynamic models, such as equivalent circuit models (ECMs), combined with a look-up table for the cell's OCV and adaptive filters or observers to evaluate both the fast-changing battery states (e.g. SOC) and the slower-changing, time-varying model parameters, such as internal resistance and cell capacity, which constitute the SOH [142].

Plett, [143] applied a dual estimation approach using a simple ECM in combination with an extended Kalman filter (EKF) to simultaneously estimate SOC and SOH, where SOH is defined as the change in capacity and resistance of the cell. The input parameters were the experimentally obtained terminal voltage and current. Similarly, Verbrugge et al. [144] implemented a simple ECM combined with a weighted recursive least squares algorithm to estimate SOC and SOH using voltage and current measurements. The SOH was defined as the values of the ECM parameters relative to their initial values. Both Plett [143]and Verbrugge et al. [144] failed to demonstrate how their algorithms perform at different operating temperatures.

Kim et al. [145] implemented a different approach, where a dual-sliding-mode-observer is combined with a simple ECM to estimate SOC and SOH (where the SOH was defined as capacity fade and resistance increase). The parallel architecture of SOC and SOH observers accounts for effects of degradation on SOC estimates, while keeping computational efforts low (the authors claimed their method to be five times faster than equivalent Kalman filter techniques). The changes in ECM parameters with temperature was considered as model uncertainty and a large operating temperature range ($-$ 30 °C to 55 °C) was covered. SOC estimation errors still reached 10%, which would have to be improved for reliable applications.

Remmlinger et al. [146] proposed a method for on-line estimation of a degradation index that is based on internal resistance, using ECM and a regressive linear least-squares algorithm. The identification process was conducted on a recurrent battery excitation specific to HEVs, recorded during the start of the combustion engine. Although the separation of SOC and SOH estimations is advantageous in that it reduces computational complexity, this approach is limited to internal resistance as the only estimator of SOH.

On-line state estimators are the most preferred choice for battery management systems (BMS) in industry due to their relatively simple implementation and low computational complexity [142]. However, on-line state estimators does not include the effects of degradation and operating temperature on the cell's OCV [147], which is used at the core of most state estimators. To achieve and maintain high accuracies in SOC estimation, changes in the OCV of the cell due to different ambient temperature and capacity-fading mechanism must be considered [148]. On-line state estimators are not generally concerned with underlying capacity-fading mechanisms. This makes it difficult to anticipate the safety hazards linked to certain capacity-fading mechanisms.

1.4.2 Physics-based models

Owing to the large number and complexity in the interplay of capacity-fading mechanisms in LIBs, physics-based models usually considers two or more of the well-known capacity-fading mechanisms such as SEI formation, cathode electrolyte interphase (CEI) and crack formation within the electrode and particle, to predict the cell performance. Physical and chemical capacity-fading mechanisms modeling required a dynamic model to estimate the driving forces for the degradation at the electrode level such as electrode potential, current densities and temperature. The two main electrochemical models: the pseudo-two-dimension (P2D) model and the single particle model (SPM) have been used as the basis for physics-based capacity fade models.

The P2D model is undoubtedly rigorous and accurate. However, it is too complicated and sluggish to be applied to BMSs. The SPM, on the other hand, provides quick responses but it is unsuitable for simulating high discharge rates and thick electrodes. The shortcomings of the SPM and the complexity of the P2D model have motivated the development of simplified versions of the P2D model to be used in the BMSs in different applications.

1.4.2.1 Pseudo-two-dimension model
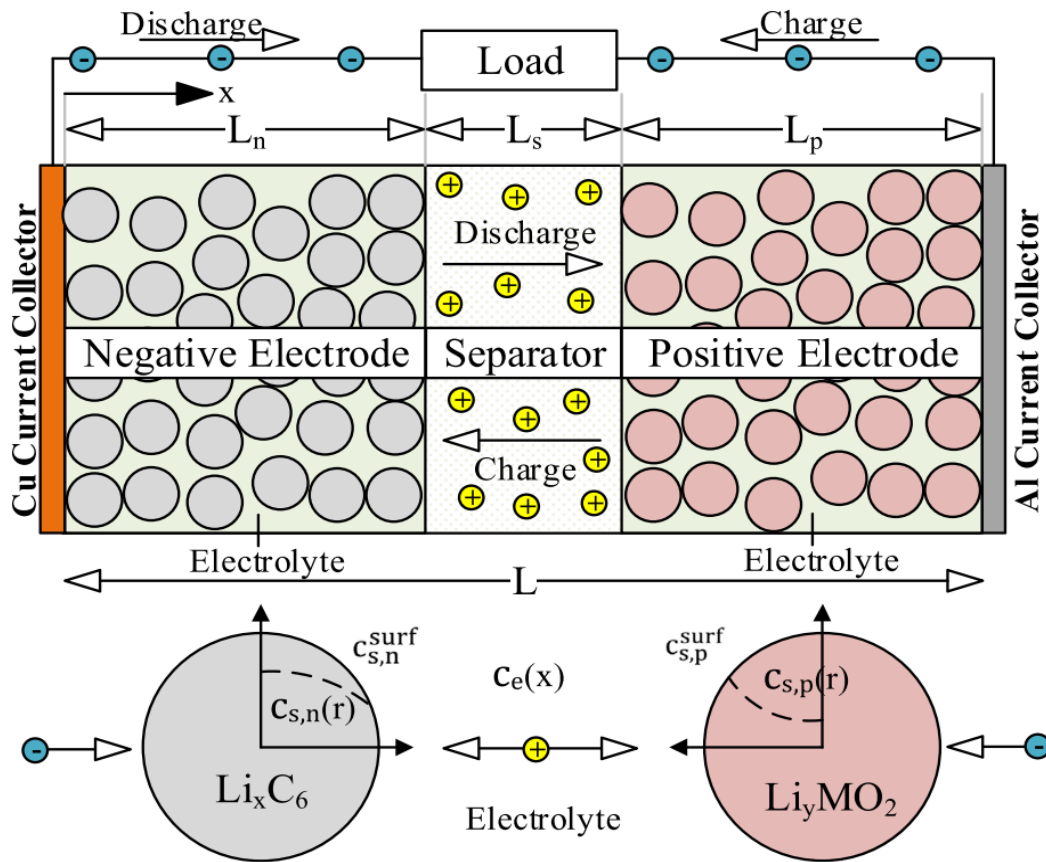
Figure 1.7. Schematic diagram of Li ion battery P2D model [149].

Doyle et al. [125] introduced the Pseudo-two-Dimensional (P2D) model for Li-ion batteries using a combination of the porous electrode theory developed by Newman and Tiedman [150] and the concentrated solution theory in 1993. Figure 1.7 shows a schematic of the Li-ion battery [149]. The P2D model handles the three domains in the cell as an independent homogenized continuum with effective conductivity properties using the Bruggeman's approximation. In the P2D model, the Li ions concentration in the solid phase (c_s) is obtained from the Fick's second law of diffusion while the Li ions concentration in the liquid phase (c_e) is based on the conservation of Li ions. Ohm's law is applied to obtain

the potential distribution in the solid phase (ϕ_1), and both Ohm's law and Kirchoff's laws are used to estimate the potential distribution (ϕ_2) in the liquid phase. The Butler-Volmer kinetic equation is used to describe the pore wall flux (j) of Li ions. The governing equations of the P2D model are presented in Table 1.1.

Table 1.1. The governing equations of P2D model

Cell compartment	Name	Governing equations
Li metal	Butler-Volmer equation	$j_n = \kappa_n \left(c_{n,\max} - c_{n,surf} \right)^{0.5} c_{n,surf}^{0.5} c_{e,n}^{0.5} \times \left[\exp\left(\frac{0.5F}{RT} \eta_n \right) - \exp\left(-\frac{0.5F}{RT} \eta_n \right) \right]$
	Over-potential	$\eta_n = \phi_1 - \phi_2 - U_n$
Separator	Material balance, liquid phase	$\varepsilon_e \frac{\partial c_e}{\partial t} = \frac{\partial}{\partial x}\left(D_{eff,s} \frac{\partial c_e}{\partial x} \right)$
	Charge, liquid phase	$-\kappa_{eff,s} \frac{\partial \phi_{2,s}}{\partial x} + \frac{2RT\left(1-t_+^0\right)}{F} \kappa_{eff,s} \frac{\partial lnc_e}{\partial x} = 0$
Porous electrode	Material balance, solid phase	$\frac{\partial c_{s,p}}{\partial t} = D_{s,p} \frac{1}{r^2} \frac{\partial}{\partial r}\left(r^2 \frac{\partial c_{s,p}}{\partial r} \right)$
	Charge, solid phase	$\sigma_{s,p}^{eff} \frac{\partial^2 \phi_{1,p}}{\partial x^2} = a_{s,p} F j_p$
	Material balance, liquid phase	$\varepsilon_{e,p} \frac{\partial c_{e,p}}{\partial t} = \frac{\partial}{\partial x}\left(D_{eff,p} \frac{\partial c_{e,p}}{\partial x} \right) + \left(1-t_+^0\right) a_{s,p} j_p$
	Charge, liquid phase	$-\frac{\partial}{\partial x}\left(\kappa_{eff,p} \frac{\partial \phi_{2,p}}{\partial x} \right) + \frac{2RT\left(1-t_+^0\right)}{F} \frac{\partial}{\partial x}\left(\kappa_{eff,p} \frac{\partial lnc}{\partial x} \right) = a_s j_p F_p$
	Butler-Volmer equation	$j_p = \kappa_p \left(c_{p,\max} - c_{p,surf} \right)^{0.5} c_{p,surf}^{0.5} c_{e,p}^{0.5} \times \left[\exp\left(\frac{0.5F}{RT} \eta_p \right) - \exp\left(-\frac{0.5F}{RT} \eta_p \right) \right]$
	Over-potential	$\eta = \phi_1 - \phi_2 - U_0 - j_{film} F\left(R_{film} \right)$

Using P2D model as the basis and Mn^{3+} disproportionation reaction proposed by Lu et al. [151], many researchers have tried to develop capacity fade model to describe and predict the cycle performance of LiMn$_2$O$_4$ cathode active material. Park et al. [152] developed a mathematical model to describe the degradation of spinel LiMn$_2$O$_4$. Cai et al. [153]developed an updated P2D thermal model that depends on the Mn^{3+} disproportionation reaction where

a shrinking core model was used to describe the solid phase diffusion in the cathode. The model accounted for changes in volume, radius, and porosity in the cathode and in the film resistance due to the Mn^{3+} disproportionation reaction. Dai et al. [154] also devised a model to describe the capacity fade in the spinel $LiMn_2O_4$ electrode by studying the effects of acid attack on the active material and the formation of SEI on the $LiMn_2O_4$ particle surface. Although half-cell studies are useful and provide valuable information about the electrochemical characteristics of the electrode material, they do not provide actual estimates of capacity fade for practical applications.

Ramadass et al.[155] developed a first principles capacity fade model for Li-ion cells by incorporating a continuous occurrence of solvent reduction reaction during constant current and constant voltage charging to explain capacity fade of the battery. The solvent reduction reaction accounted for the formation SEI on the anode. Similarly, Narayanrao et al. [156] proposed a hypothesis based on a set of phenomenological evolution models for major degradation mechanisms namely SEI formation fracture and isolation. The SEI was assumed to be formed on fresh surfaces of the particles as well as on fractured surfaces. Fu et al. [157] developed a physics-based model for side reactions based on the formation of deposit layers and loss of electrolyte and integrated into a P2D electrochemical-thermal model. From the above previous works, the P2D model has been coupled with developed capacity fade model to predict and study the various cell designs and operating conditions on the electrochemical performance of LIBs.

1.4.2.1 Single particle model
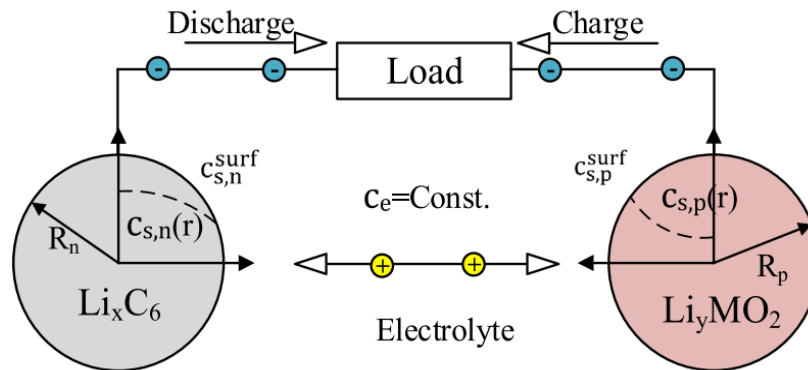
Figure 1.8. Schematic diagram of single particle model (SPM) [149].

Zhang et al. [158] proposed a simplified version of the P2D model known as the single particle model (SPM) in 2000. The development of the SPM is based on two main assumptions: first, each electrode is modeled as two spherical particles in which ion (de) intercalation phenomena occur. Second, the variation in the electrolyte concentration and in the potential are not considered. Figure 1.8 illustrates schematic diagram of the SPM [149]. The main governing equations of the SPM are the solid-state concentration and Butler-Volmer kinetics equations at both the positive and negative electrodes.

Owing to the simplicity of the (SPM), it the frequently used as the basis for physics-based degradation models. The formation and growth of the SEI at the anode usually forms the central hypothesis in many previously developed capacity fade models [155,157,159–163]. Laresgoiti et al. [163] use the SPM as the basis to model the break and repair of the SEI as the primary cause for capacity fade in Li-ion cells. Other examples of SPM-based degradation models, are reported by Pinson and Bazant [162], Christensen and Newman [160], Prada et al. [164], and Prasad and Rahn [165]. Deshpande et al. [14] proposed a mathematical mode to describe the Li loss caused by couple chemical and mechanical degradation (a crack propagation model driven by diffusion induced stress and subsequent Li-consuming

passivation reactions over new crack surfaces) for capacity loss prediction. A general drawback of using the SPM as a basis for degradation models is that the SPM does not account for non-uniformities in electrolyte composition within the pores of the electrode or separator, or ohmic losses resulting from electronic conduction in the solid part of the electrode. The neglect of liquid diffusion and solid-phase conductivity limits validity of the SPM to currents below 1C [166].

1.4.2.1 Simplified models

The simulated concentration profiles of the electrolyte via a P2D model at different discharge rates [36] suggests that, the electrolyte properties can be assumed constant at low current rates. Hence, the SPM is a preferred choice for simulating the electrochemical performance at low C-rates. However, at a higher C-rate, the changes in the simulated electrolyte concentration is significant and requires a more accurate and computationally viable model. To ensure the safety of electric vehicles, the Li ion battery pack should be monitored by a BMS, which rely on fast and accurate prediction models. BMS usually depends on simple empirical models [167], which are fast but cannot predict battery-aging parameters as it ages. In view of this, the simplified P2D models are developed to compensate for the drawbacks of the two electrochemical-based models and empirical models. The simplified P2D models are mostly based one-dimensional polynomial profiles for the electrolyte properties. These simplified P2D models are developed mainly for applications in control, on-line monitoring, optimization, parameter estimation, and age prediction. Due to the use of physical-based equations, simplified P2D models are more accurate and suitable for parameter estimation and age prediction of Li-ion cells [149].

Wang et al. [168] adopted a polynomial profile to simulate the solid-state concentration function in P2D model. Their model predicts both the battery and the fuel cells behavior. Using a similar approach, Subramanian et al. [169,170] proposed a simplified model, known as the Parabolic Profile approximation (PP), for Li-ion batteries. In the PP model, the solid concentration equation of the P2D model is simplified by assuming a solid concentration polynomial profile. This assumption allows the reduction of Partial Differential Equations (PDEs) to simpler Differential Algebraic Equations (DAEs). The accuracy of the PP model depends on the order of the polynomial approximation. Cai et al.[171] proposed a simplified Li-ion battery model using a Proper Orthogonal Decomposition (POD). In this model, the number of equations is reasonably reduced and so is the computational time. The predictions of the POD model show excellent agreement with that of the P2D model up to 20C discharge rates. However, it is necessary to rely on experimental data to run the POD model and it does not work well for real time applications. Several simplified models have been developed to reduce the computational time by reducing the PDEs and Buttler Volmer equation in the P2D and for accurate online LIBs capacity fading predictions [172–175].

1.5 Focus and objectives

From the above literature review, it can be inferred that, to successfully implement high energy density active materials into LIBs, there is the need to understand their capacity-fading mechanisms and address each mechanism cautiously. The use of sophisticated experimental analysis via post-mortem studies is very beneficial in outlining the various capacity fading mechanisms after cell degradation has occurred. To adopt these methods to analyze the capacity fade mechanisms during cycling will involve an extensive amount of

resources since individual cells would have to be used for each cycle. However, the use of battery performance-based analysis is quite convenient, non-destructive, and less expensive to analyze the capacity-fading mechanisms during cycling. Nevertheless, a combination of the two will provide a vivid understanding of the various mechanisms at different cell operations especially at the end of the cycling process.

In addition, mathematical models are required to describe the various capacity-fading mechanisms and predict the effect of cell designs and operating conditions on the capacity fade models is effective only at low current rate; however, cell degradation mechanisms such as particle cracking which is famous in high energy density active material are accelerated and predominant at high current rate. Thus, for high current rate application and to study the effect of the electrolyte on the capacity retention of LIBs, one must apply the P2D models as the basis for capacity fade modeling. This brings us to the main objectives of this work. To use a model parameter estimation capacity fade analysis method to unveil the capacity-fading mechanisms of spinel-based cathode materials, and silicon-based anode materials for LIBs.

1. To develop a physics-based capacity fade model and incorporated into the P2D model to describe the long-term cycle performance of spinel-based cathode materials, and silicon-based anode materials for LIBs.

2. To use the developed physics-based capacity fade model for the spinel-based cathode to devise a time effective accelerated capacity fade analysis framework for LIBs.

3. To employ the physics-based model for the silicon-based anode to describe the effect of adhesive strength on the long-term cycle performance of LIBs.

1.6 Outline

This thesis consists of eight chapters. The above literature review constitute Chapter 1 Chapter 2 to 7 is the main body of the thesis and each chapter is structured into an introduction and sections describing model development, experiments, methodology, results and discussions, and conclusions. In chapter 2 to 4, our focus will be on the cathode active materials while in chapter 5 to 7, we will focus on the anode active material

Chapter 2 presents a non-destructive capacity-fading analysis method, which involves the use of a parameter estimation technique to monitor parameters that changes with cycling in a physics-based model to unveil the capacity-fading mechanisms in a spinel-based cathode and graphite anode Li-ion cell at different operating conditions.

Chapter 3 involves the development of a physico-chemical capacity fade model (PCM) to describe the various capacity-fading mechanisms identified in Chapter 2. PCMs are also physics-based capacity fade model since they consider two or more degradation mechanisms. The PCM is coupled with a P2D model to predict and quantify the various degradation mechanisms of the spinel-based cathode and graphite anode Li-ion cell considered in this work.

Chapter 4 demonstrates the application of the developed PCM in combination with the P2D model to propose a time-effective accelerated cycling aging analysis framework based on time-temperature superposition for LIBs.

Chapter 5 shows an extension of the non-destructive capacity-fading analysis method used in Chapter 2 to Si-based anodes to identify the degradation mechanisms, and to study the effect of a polydopamine interlayer on the long-term cycle performance of Si-based anode LIBs.

Chapter 6 involves the development of a coupled chemo-mechanical degradation model to describe the capacity-fading mechanisms of Si-based anode with different adhesion strength between the copper current collector and composite silicon electrode identified in chapter 5. The developed model is used to study the design parameters of an adhesive interlayer on the cycling performance of the Si-based LIBs.

Chapter 7 deals with the application of the development of a coupled chemo-mechanical model to evaluate the effects of the adhesion strength on the electrochemical performance of Si-based LIBs. In addition, the developed model will be used to investigate the effects of adhesion strength and various cell design parameters on the specific capacity of the Si-based Li-ion cells. The influence of the intrinsic properties and design parameters of the thin film polydopmine interlayer on the cycle performance will also be studied in the Chapter.

Overall conclusions and suggested future work are presented in Chapter 8.

Chapter 2

Capacity fade analysis of spinel-based cathode materials

2.1 Introduction

Over the past decade, spinel $LiMn_2O_4$ has gained an immense attention owing to its excellent qualities as a cathode material, including low cost, high safety, a high discharge voltage plateau (~4.0 V vs Li/Li^+) and facile production. In addition, spinel $LiMn_2O_4$ does not contain cobalt, which makes it an environmentally friendly active material. The profound qualities of spinel $LiMn_2O_4$ makes it a suitable candidate for EVs and hybrid electric vehicle (HEVs) applications. However, spinel $LiMn_2O_4$ suffers from a fatal capacity fade upon prolong cycling and extended storage at higher temperatures over 55 °C, particularly when graphite is used as the negative electrode [176,177]

In the quest to improving the electrochemical performance of the spinel, $LiMn_2O_4$ cathode material, an intensive effort has been utilized in identify and control the factors responsible for the fatal capacity fading [178–180]. So far, apart from the common capacity fading mechanisms in LIBs such as the formation of SEI at the anode, additional mechanisms have been discovered for the spinel $LiMn_2O_4$. These mechanisms include the dissolution of the $LiMn_2O_4$ active material via Mn^{3+} disproportionation reaction to form a more stable Mn(IV) and soluble Mn^{2+} species [180] and decomposition of the electrolyte via an oxidation process to form the cathode electrolyte interphase (CEI) [181]. In addition, the catalytic formation of SEI on the graphite anode by the reduced Mn nanoparticles is considered as the most critical mechanism that leads to capacity fading in this cell system [151,182,183].

All these capacity-fading mechanisms of the spinel $LiMn_2O_4$ were identified via a destructive and expensive method. Identification of capacity-fading mechanisms via a non-destructive method remains a great challenge for Li-ion battery management systems. Nevertheless, some authors have tried to utilize this method to describe the degradation mechanisms of LIBs of different cell compositions

Zhang et al.[129], conducted a capacity fade analysis on a Li ion cell comprising $LiNiCoO_2$ cathode and a carbon anode using a physics-based single particle model. The authors postulated that, the capacity fade of LIBs due to SEI formation and loss of cathode active material can be studied via the changes of three physics-based model parameters namely, the initial SOCs for the cathode and anode ($x_{0,pos}$ and $x_{0,neg}$) and the volume fraction of the cathode (ε_{pos}). However, the effect of temperature was not considered because single particle physics-based model cannot account for electrolyte decomposition at high temperatures. Lam et al. [184] also adopted a physics-based P2D model to analyze the effect of discharge current density on the degradation mechanism of a generic Li-ion battery. The cycle performance of the cells were described by the fluctuation in the identified three parameters (the initial SOCs for the cathode and the negative electrode ($x_{0,pos}$ and $x_{0,neg}$) and the volume fraction of the cathode (ε_{pos})) as cycling proceeds. These two authors did not consider the effect of temperature on their analysis. To the best of our knowledge, there have been no reports on the analysis of capacity fade at different temperatures based on the changes in the initial state of charge (SOCs) of the cathode and anode ($x_{0,pos}$ and $x_{0,neg}$), and the volume fraction of the cathode (ε_{pos}) which are known to change with cycling for the $LiMn_2O_4$/graphite cell. Hence, in this Chapter, we will conduct a capacity fade analysis of $LiMn_2O_4$/graphite cell via the changes in the initial SOCs for the cathode and anode

($x_{0,pos}$ and $x_{0,neg}$) and the volume fraction of the cathode (ε_{pos}) using a physics-based P2D model at 25 and 60°C. The P2D model accounts for the variations electrolyte concentration while the single particle model does not, which makes it a better option for capacity analysis at different temperatures and current rates.

The capacity-fading mechanisms identified in the Chapter forms the basis for the capacity fade model developed in Chapter 3, which can be used to quantify and predict the capacity-fading mechanisms.

A large part of the work presented in this chapter was published in [185].

2.2 Experiment

The experimental discharge capacity retention at 25 and 60 °C for a 2032 coin-type Li ion cell comprising $LiMn_2O_4$ as the cathode and artificial graphite as the anode is presented in Figure 2.1. We used a polyethylene separator (ND420, Asahi Kasei E-Materials, Japan) and a liquid electrolyte consisting of 1.15 M $LiPF_6$ in an ethylene carbonate and ethylmethyl carbonate mixture (3/7, v/v, ENCHEM, Korea). The mass composition of the cathode was 90 wt% $LiMn_2O_4$ (Iljin Materials, Korea), 5 wt% electric conductor (Super P Li®, Imerys, Belgium) and 5 wt% poly(vinylidene fluoride) (PVdF, KF-1300, Kureha, Japan) as a binder. *N*-methyl pyrrolidone (NMP, Sigma Aldrich, USA) was used as the solvent for electrode slurry. The anode composition was 95 wt% artificial graphite (Showa Denko, Japan), 1wt% electric conductor (Super P Li®, Imerys, Belgium), 4 wt% PVdF (Solef6020, Solvay, France). The cycling performance of the cells were conducted at 1C charge/discharge and a lower and upper cut-off voltage of 3.0 and 4.2 V, respectively.
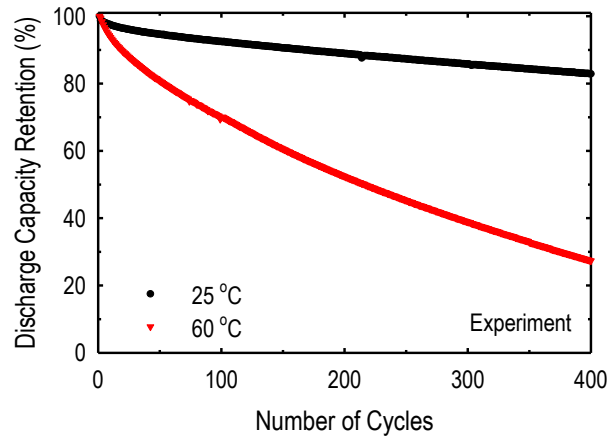
Figure 2.1. The experimental discharge capacity retention of $LiMn_2O_4$/graphite cells as a function of number of cycles at 25 and 60 °C. The cells were cycled at 1C and an upper and lower cut of 3.0 and 4.2V

2.3 Results and discussion

2.3.1 Parameter Estimation

To evaluate the parameters that changes with cycling, we compared the experimental voltage profiles obtained from the 2032 coin-type cells at 25 and 60 °C to those from the P2D model predictions at selected cycle numbers. The outcome of the comparison at 25 and 60 °C are shown in Figure 2.2a and 2.2b, respectively. The model predictions were made with the parameters in Table 2.1. The correlation between the experimental voltage profiles and those of the physics-based model predictions are quite high. This is evidenced by the lower estimated standard deviation as shown in Figure 2.2.
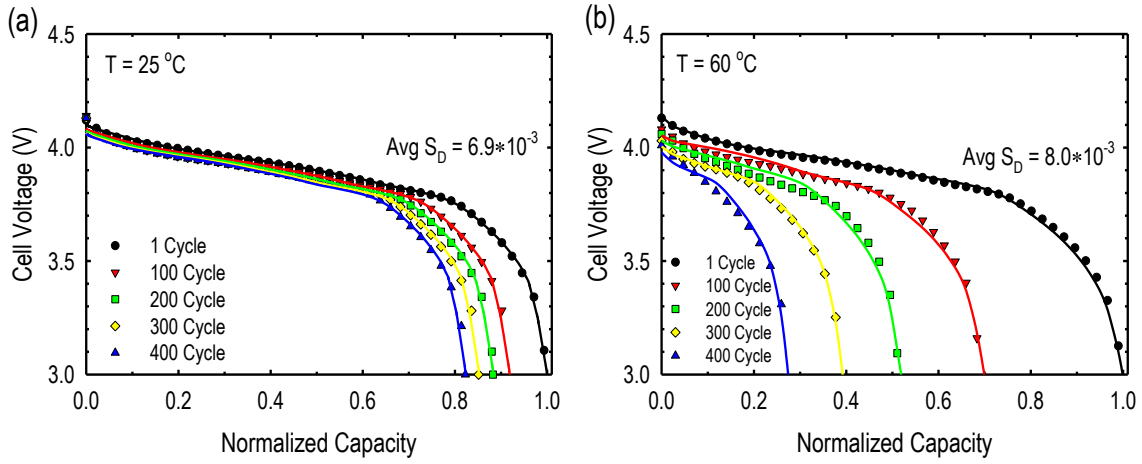
Figure 2.2. Comparison of experimental discharge profiles and model-prediction for 1st, 100th, 200th, 300th and 400th at (a) 25 ºC and (b) 60 ºC.

Table 2.1. Design parameters, electrode specific parameters, and other constants used in this study.

Design parameters	$Li_yMn_2O_4$	Li_xC_6
Electrode thickness, μm [a]	36	43
Volume fraction electrolyte [a]	0.33	0.37
Maximum solid phase concentration, mol m^{-3}	23230	27362
Initial SOC of the electrode	0.45	0.58
Volume fraction of active material	0.559	0.566
Reaction rate constant, mol m^{-2} s [c]	3.94×10^{-11}	3×10^{-11}
Density g/cm^3 [b]	4.2	2.2
Matrix conductivity, S/m [b]	10	100
Separator thickness, μm [a]		20
Separator porosity [a]		0.41
Initial salt concentration, M [a]		1.15
Diffusion coefficient, m^2/s [c]	3.98×10^{-14}	1.14×10^{-14}
Particle radius, μm [a]	6.6	10.5

[a] Value set in cell design

[b] Parameters based on literature value [24]

[c] Parameters not based on literature value

The high correlation between the experimental voltage profiles and the physics-based model predictions at the two temperatures in Figure 2.2 were achieved by using a non-linear

least square method to estimate the three parameters considered to change with capacity fade in this study. These parameters are the initial SOCs for the positive and negative electrode ($x_{0,\text{pos}}$ and $x_{0,\text{neg}}$) at the beginning of charging and the volume fraction of the cathode (ε_{pos}). The changes in the parameters changing with cycling at 25 and 60 °C is illustrated in Figure 2.3. The volume fraction of the cathode (ε_{pos}) decreased with cycling with the rate of decrease being higher at 60 °C (Figure 2.3a). Also, the initial SOC for the cathode ($x_{0,\text{pos}}$) increased with cycling for the two temperatures (Figure 2.3b). The rate of increase was rapid at 60 °C. On the other hand, a different trend was observed for initial SOC for the anode ($x_{0,\text{neg}}$), that is, it changed with cycling at 25 °C but it did not show any significant changes at 60 °C. Figure 2.3 demonstrates that, during cycling, both the cathode and anode become frequently less charged at 25 °C while at 60 °C, only the cathode becomes less charged.
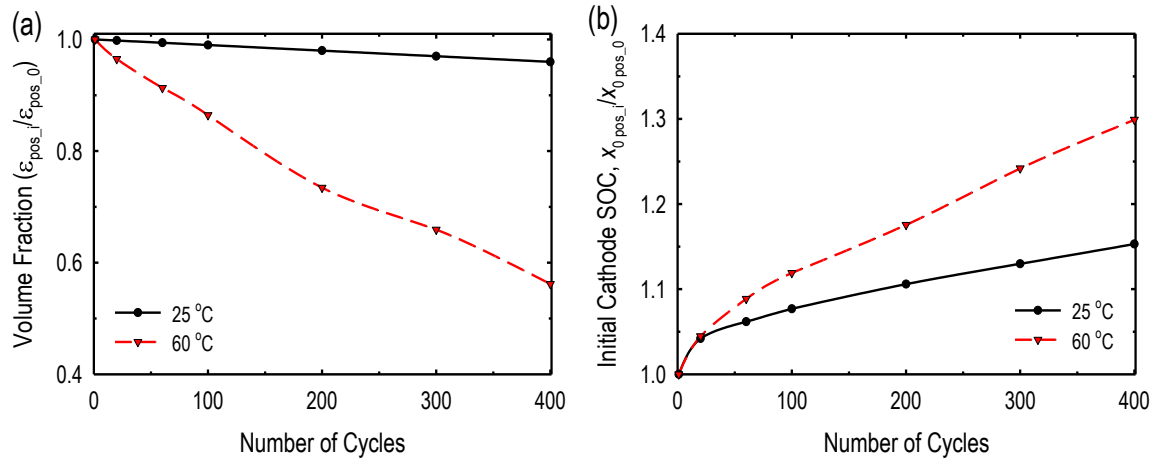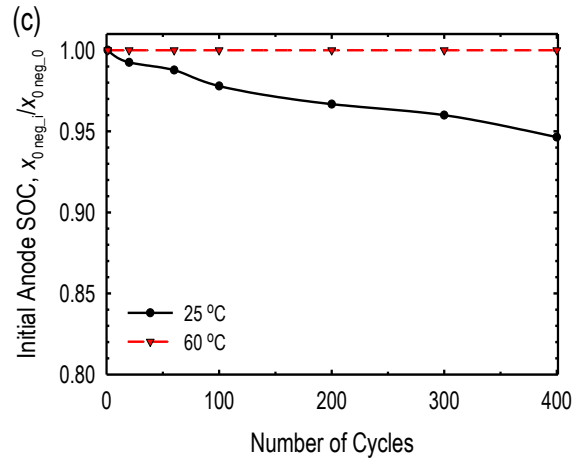
Figure 2.3. The relative changes in (a) volume fraction of the active material of the cathode, (b) initial SOC of the cathode and (c) initial SOC of the negative electrode, with cycling at 25 and 60 °C.

The predicted SOCs for the cathode and anode at the end of discharge (EOD) (x_{pos} and x_{neg}) and, at 25 and 60 °C are shown in Figure 2.4a and 2.4b respectively. At 25 °C (Figure 2.4a), the anode becomes less discharged while the cathode shows no relevant changes at the EOD (x_{neg} increases while x_{pos} remains constant). The SOC of the cathode remained constant at ca. 0.98, stipulating that the cathode is almost completely intercalated. A similar pattern was observed in the intercalation of the negative electrode of the cells cycled at 60 °C (Figure 2.4b), however, unlike the intercalation pattern in the cathode at 25 °C, that at 60 °C became less intercalated (x_{pos} decreases). In addition, the rate at which the negative electrode becomes less discharged at the EOD is more severe at 60 °C than at 25 °C. A detail discourse of the difference in the patterns at the two temperatures are given in section 2.3.3.
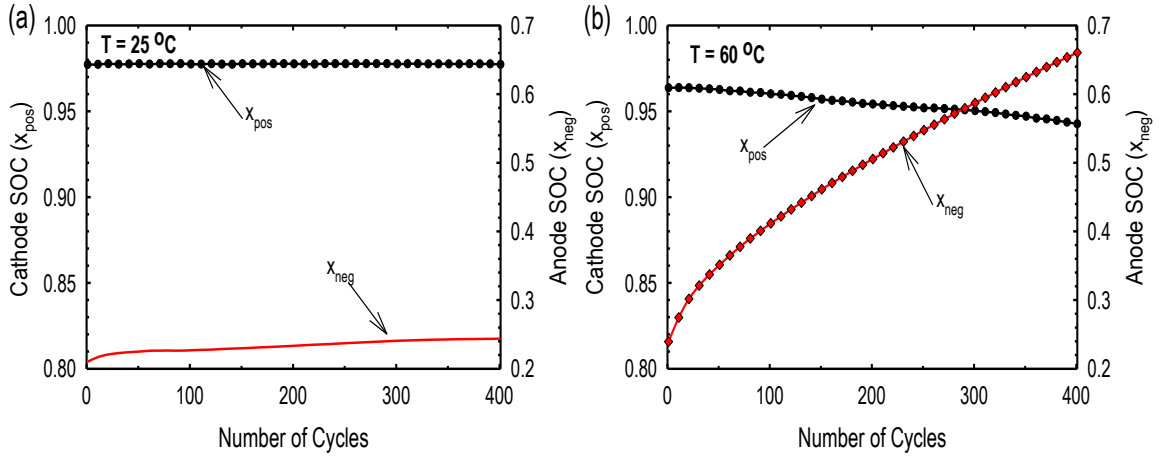
Figure 2.4. Predicted SOC at the EOD at (a) 25 °C and (b) 60 °C, using the parameters presented in Figure 2.3.

2.3.2 Model prediction

We fitted the model parameters to the quadratic equations presented in Table 2.2. The initial SOC for the negative electrode at 60 °C (x_{neg}) was not included in Table 2.2 because it did not change with cycling. The various fitting parameters of the equation presented in Table 2.2 were obtained using the curve-fitting tool in MATLAB. The parameters extrapolated from the model equations are depicted in Figure 2.5. The parameter extrapolation was made based on the assumption that; the capacity fading mechanism is not altered during the duration of our prediction.

Table 2.2. Mathematical expression used for the extrapolation in Figure 2.5

Parameters	Expression	a	b	c
$\varepsilon_{pos,\,25\,°C}$	$ax^b + c$	-1.005×10^{-4}	1.000	1.000
$x_{0,\,pos,\,25\,°C}$	$ax^b + c$	1.338×10^{-2}	0.4142	0.9892

$x_{0,\,neg,\,25\,°C}$	$ax^b + c$	-9.526×10^{-4}	0.6694	1.001
$\varepsilon_{pos,\,60\,°C}$	$ax^b + c$	-1.005×10^{-4}	0.796	1.006
$x_{0,\,pos,\,60\,°C}$	$ax^b + c$	5.81×10^{-3}	0.6557	0.9986
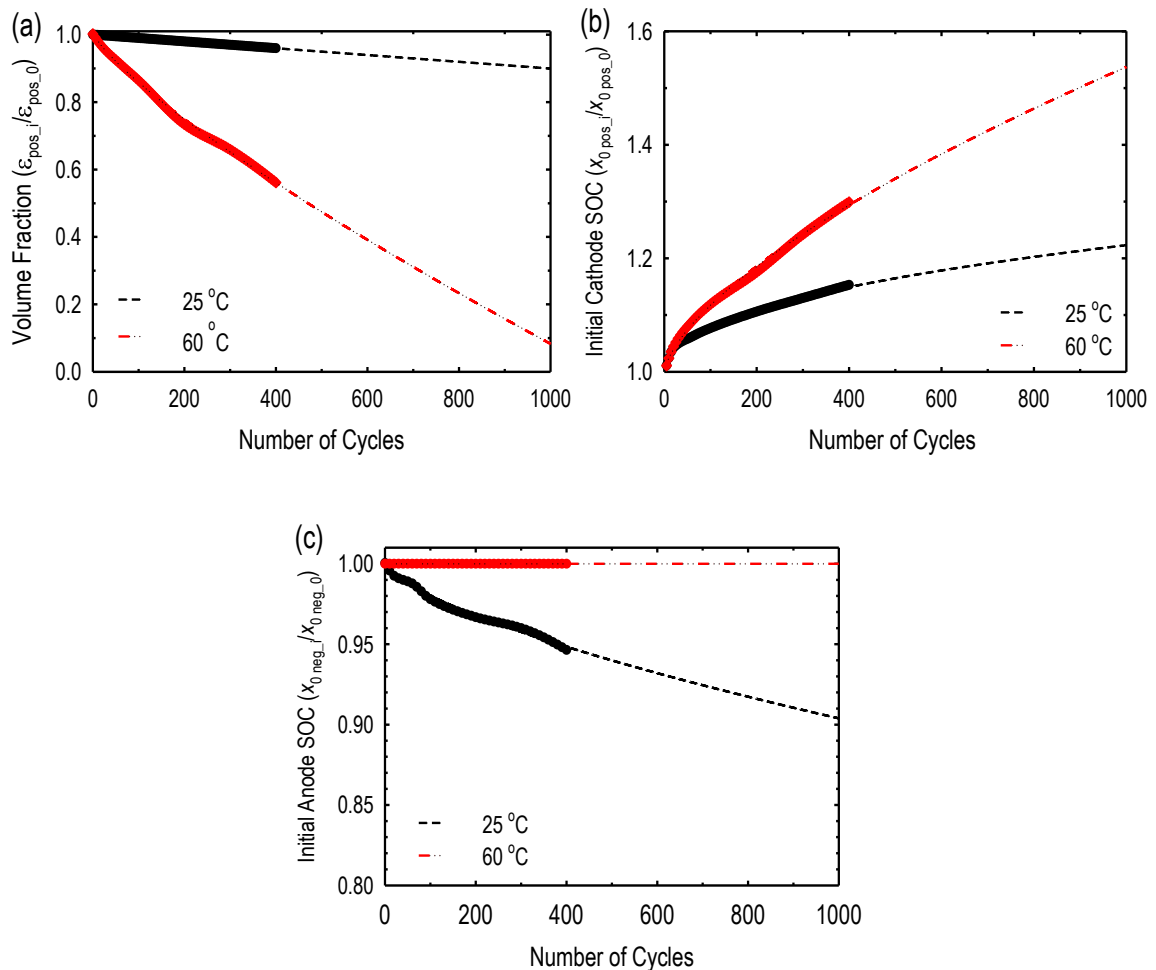
Figure 2.5. Extrapolation of the model parameters presented in Figure 2.3. The mathematical expressions used for the extrapolation are presented in Table 2.2.

The extrapolated model parameters in Figure 2.5 were used to predict the discharge capacity retention as a function of cycle number at 25 and 60 °C. The model predictions of the discharge capacity retention for 1000 cycles at the 25 and 60 °C are shown in Figure 2.6. The experimental discharge capacity retention for 400 cycles were compared with the model prediction at 25 and 60 °C and are also shown in Figure 2.6a and 2.6b, respectively. There

was a good agreement between the experimental data and the model predictions. A prediction of the discharge capacity retention by an empirical model (Table 2.3) at 25 and 60 °C have also been demonstrated in Figure 2.6. At 25 °C, the predicted discharge capacity retention by the physics-based model at the end of the 1000th cycle was quite higher than that predicted by the empirical based model. This is in contrast to the previous report made by Zhang et al. [129] when they compared a single-particle physics-based model prediction of discharge capacity of a 1 Ah $LiNiCoO_2$/carbon Li ion cell to that of an empirical equation at 25 °C. This contrast can be attributed to the different cell designs and the active material of the cathode employed in the two studies. A similar trend was also observed at 60 °C in Figure 2.6b. For the empirical equation prediction, the cell completely died before it got to the 700th cycle, while for the physics-based model, the cell lasted to ca. 900th cycle.
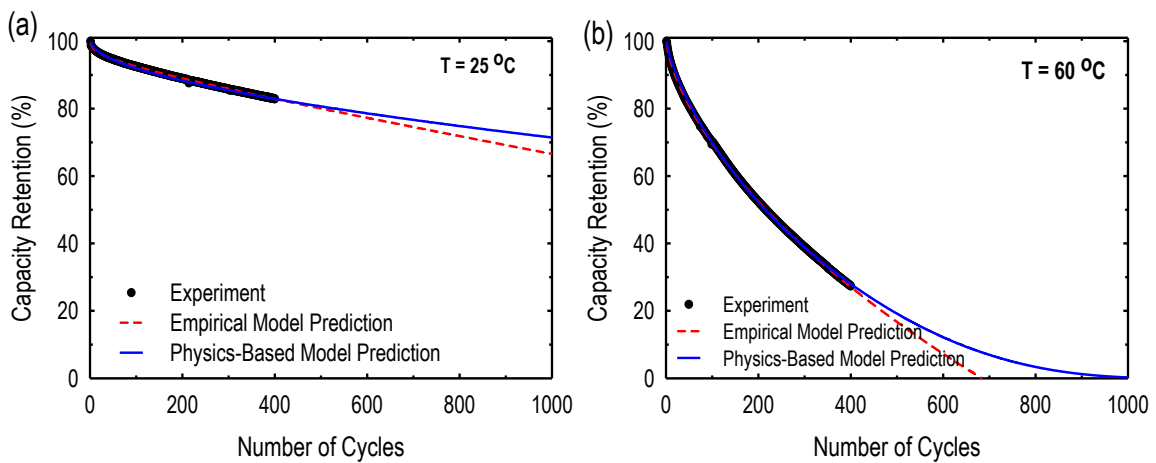
Figure 2.6. Discharge capacity retention as a function of number of cycles predicted by the physics-based model and empirical model at (a) 25 and (b) 60 °C. The empirical model predicted a fast decay of the capacity at both temperatures.

Table 2.3. Empirical model expressions

Temperature	Model	A	B	C	D
25 ˚C	$Ax^B + Cx + D$	−3.676	0.1801	−0.02398	103.3
60 ˚C	$Ax^B + Cx + D$	−1.434	0.7124	0.07247	100.5

Figure 2.7 shows the predicted SOCs of the cathode and anode at the EOD using the estimated model parameters. The predicted SOC of the cathode at the EOD at 25 °C (Figure 2.7a) remained unchanged, which is like that observed in the first 400 cycles in Figure 2.4. That of the anode also continued to increase until the 1000th cycle. Increasing the temperature to 60 °C in Fig 2.7b accelerated the rate at which the SOC of the negative anode at the EOD increased (less discharged). The SOC of the cathode at the EOD also begun to decrease (less intercalated) until the 800th cycle where it remained constant. The detailed analysis of the capacity fade of the LiMn$_2$O$_4$/graphite cells at 25 and 60 °C based on the information derived by using the physics-based model will be presented in the following section.
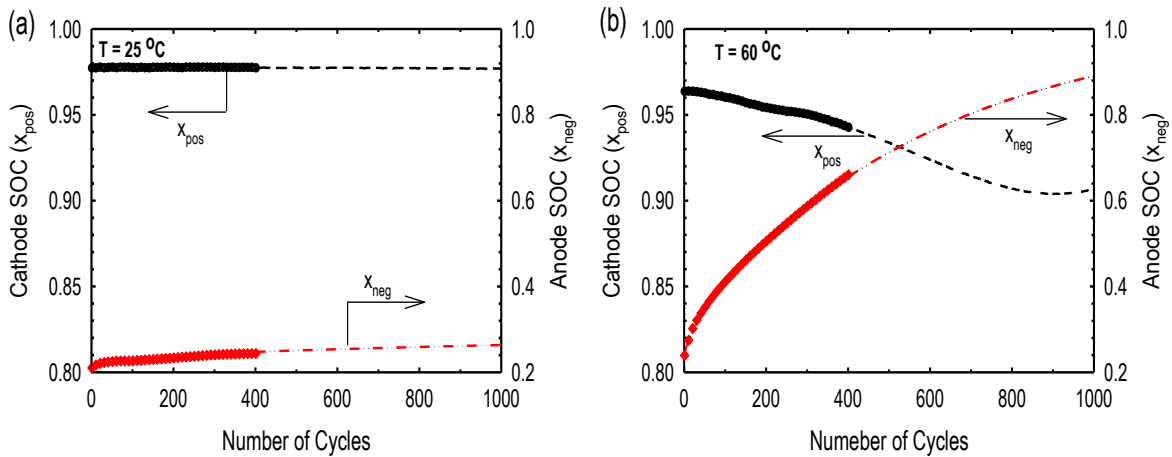
Figure 2.7. The predicted SOCs for the positive and negative electrode at the EOD using the extrapolated model parameters presented in Figure 2.5. The symbols show the SOC at the EOD in Figure 2.4.

2.3.3 Analysis of capacity fade

From the results presented in the previous section, it is clearly seen that, temperature has a profound effect on the capacity-fading mechanism of the $LiMn_2O_4$/graphite cells. The phenomenon constituting these changes are discussed in this section.

The study conducted on the variation of the parameters with cycling indicates that the volume fraction of the active material in the cathode (ε_{pos}) decreases as cycling proceeds with the rate of decrease being accelerated at a higher temperature (see Figure 2.3). This postulates that, the cathode losses some of the active material during cycling and the loss is high at higher temperatures. For the, $LiMn_2O_4$/graphite cells, the loss of active material has been attributed to the dissolution of the Mn^{2+} due to the disproportionation reaction of Mn^{3+} into soluble Mn^{2+} species and stable Mn^{4+} species [31-33]. Experimentally, it has been reported that, increasing the temperature increases the rate of Mn dissolution in the cathode resulting in a fatal capacity decay of the cells [176,186,187]. Hence, the results obtained in our parameter estimation analysis of the capacity fade at the two given temperatures are in line with that of previously reported experimental results.

In addition, there have been several previous reports on the occurrence of side reactions on the negative graphite electrode during charging process [188,189]. These side reactions are known to consume Li ions giving rise to the formation of SEI on the surface of the anode. In this study, the loss of the Li ions can be envisioned in the variation of the both the initial SOCs and that at the EOD of the cathode and anode. Owing to the relatively high rate of SEI formation on just produced cells, the loss of Li ions to the formation of SEI controls the capacity fade during the first few cycles (pre-cycling) [189]. However, the capacity fade analysis in this study was conducted after the pre-cycling stage; hence, the quantitative

estimation of the Li ions loss to the SEI formation during the first stage was not done. Nevertheless, during the entire cycling at 25 °C, the SOC of the cathode (x_{pos}) did not change. Notwithstanding, the anode became increasingly less de-intercalated at the EOD. That is, there is a progressive deposition of Li ions in the graphite negative electrode that cannot be intercalated back into the cathode. In addition, the residual capacity of the cathode decreases as the volume fraction of the active material reduces. Here the cathode is the limiting electrode because it is almost completely discharged at EOD, causing the cell to reach the lower cut-off voltage.

The capacity-fading mechanism at 60 °C is slightly different from that at 25 °C. That is, there was a continuous trapping of Li ions in the anode, which occurred at a rapid rate throughout the entire cycling (rapid increase in in Figure 2.7b). In addition to that, the cathode was progressively less intercalated at the EOD, resulting in a decreasing of the SOC of the cathode (x_{pos}) at the EOD. However, the initial SOC of the anode ($x_{0,neg}$) remained constant. This is due to the rapid reduction in the holding capacity of the cathode as the cathode loses more active material. In return, more usable Li ions are accumulated inside the negative electrode, casing fatal capacity decay. Thus, the loss of Li ions, which leads to a sudden increase in the SOC of the anode (x_{neg}) at EOD, is not only due to SEI formation, but also due to a significant reduction in the holding capacity of the cathode. This makes it impossible for the intercalated Li ions into the anode to de-intercalate back into the cathode. This is supported by the negligible changes in the initial SOC of the anode ($x_{0,neg}$). Experimentally, it has been reported that, at elevated temperatures, the dissolved Mn^{2+} migrate through the separator to the graphite where they are reduced to metallic Mn nanoparticles. The Mn nanoparticles act as catalyst perpetuating the rapid decomposition of

the electrolyte to form the SEI on the surface of the negative electrode during cycling [182]. The formation of the SEI leads to a continuous trapping of the usable Li ions resulting in a drastic capacity decay [183]. This is evidenced in the reduction of the SOC of the cathode as observed in Fig 2.7b. At the last 200 cycles, the capacity mechanism at 60 °C slightly changes. The rate of Li ion trapping due to SEI formation continuously increased with cycling and the cathode became the limiting electrode (x_{pos} remained constant).

2.4 Conclusion

The capacity fading characteristics of a $LiMn_2O_4$/graphite Li ion cells was analyzed by fitting the model predictions of a physics based P2D model to experimental discharge profiles obtained from cycling Li ion cells at 25 and 60 °C. The parameters that changed with cycling were estimated using a nonlinear least square technique. The analysis conducted on the experimental discharge profiles showed that, the capacity fading mechanism of the $LiMn_2O_4$/graphite Li ion cells were affected by temperature. The major capacity fading mechanism observed based on our parameter estimation analysis is the trapping of the cyclable Li ions into the SEI on the anode and reduction in the volume fraction of the active material in the cathode. At 25 °C, the dominant capacity fading mechanisms was the formation of the SEI layer with a small reduction in the active material of the cathode. The cathode was the limiting electrode at 25 °C. At 60 °C, the reduction in the volume fraction of the active material occurred at a rapid rate and the cathode became less intercalated at the end of discharge. There was also a rapid trapping of Li ions to the formation of the SEI due to the presence of the Mn nanoparticles at the graphite negative electrode.

Chapter 3

A capacity fade model for spinel-based cathode materials

3.1 Introduction

The capacity fade in spinel $LiMn_2O_4$ is known to accelerate with the cycling and temperature due to the successive increase in the rate of Mn^{2+} dissolution which is notably high at the delithiated state (at >4.1 V vs. Li/Li$^+$) where the electrochemical oxidation of the solvent is also significant [190]. Further studies have revealed that Mn dissolution accounts for only 23% and 34% of total capacity fade at 25 °C and 55 °C respectively, which suggests that the capacity fading during cycling is caused by not only simple Mn dissolution but also structural change and decomposition of the electrolyte [180,191].

The dissolution of Mn^{2+} is via the disproportionation reaction of Mn^{3+} [151] as mentioned in Chapter 1. Park et al. [152] devised a mathematical model to describe the degradation of spinel $LiMn_2O_4$ based on this mechanism. The authors postulated that the dissolution of Mn^{2+} leads to changes in the effective transport properties, which play a critical role in capacity, fade. Similarly, Cai et al. [153] developed an advanced P2D thermal model based on the Mn^{3+} disproportionation reaction. The model accounted for changes in volume, radius, and porosity in the cathode and in the film resistance due to the Mn^{3+} disproportionation reaction. Dai et al. [154] also developed a model to describe the capacity fade in the spinel $LiMn_2O_4$ electrode. Therein the Mn^{2+} dissolution was described an acidic attack on the active material and the formation of SEI on the $LiMn_2O_4$ particle surface. All above capacity-fade models utilize a half-cell for their model validation. Although half-cell studies are useful and provide

valuable information about the electrochemical characteristics of the electrode material, they do not provide actual estimates of capacity fade for practical applications. In addition, the dissolved Mn^{2+} is known to be reduced at the graphite electrode, which contribute to capacity decay. Thus, to fully understand and model the capacity fade of spinel $LiMn_2O_4$, their effect on the anode must be taken into consideration.

In this Chapter, we present a comprehensive capacity fade model (physico-chemical model) that accounts for SEI formation and dissolution in the anode, for dissolution of the $LiMn_2O_4$ cathode, for the effect of the reduced Mn nanoparticles on the SEI at the anode, and for the formation of a cathode-electrolyte interphase (CEI) layer on the cathode. A decrease in the Li-ion diffusion coefficient in the cathode as result of Mn^{2+} dissolution is added as a factor that causes capacity fade. The effect of temperature on the capacity fade parameters and chemical reactions are included in this model via an Arrhenius-type dependence of the rate constants and apparent diffusion coefficient. The P2D model is used as the basis for this capacity fade model and the model is solved in the battery module of COMSOL Multiphysics.

A large part of the work presented in this chapter was published in [192] and was presented at the 2016 Pacific Rim Meeting on Electrochemical and Solid-state Science (PRIME) in Honolulu, Hawaii, USA.

3.2. Model development

The major reactions responsible for the capacity fade in this model are the disproportionation reaction of Mn^{3+} in the cathode, the solvent oxidation in the cathode, the formation and dissolution of SEI in the anode, and solvent and ion reductions at the anode. These side reactions have already been discussed extensively in previous work [152,178,189,190].

3.2.1 Modeling of Mn^{2+} dissolution in the cathode

The Mn^{2+} dissolution at the cathode into the electrolyte is assumed to occur according to the following disproportionation reaction of Mn^{3+} [178,190]:

$$2Mn^{3+}_{(s)} \rightarrow Mn^{4+}_{(s)} + Mn^{2+}_{(l)} \qquad [3.1]$$
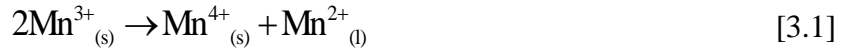
The rate of dissolution is proposed to be a function of time and is expressed as [151]

$$\left[1-\left(1-X_a\right)^{1/3}\right]=k_0 t , \qquad [3.2]$$

where k_0 is the reaction rate constant (s⁻¹), and X_a is the dissolution reaction shown in Eqn. [3.3] and is defined as

$$X_a = \frac{2\times\left(\text{Amount of Mn(II) ions in the electrolyte}\right)}{\text{Amount of Mn(III) ions in the spinel cathode}} . \qquad [3.3]$$

The reaction rate constant is defined by

$$k=k_0 \exp\left(-\frac{E_a}{RT}\right). \qquad [3.4]$$

From Eq. [3.3], the decrease in volume due to Mn^{2+} dissolution can be derived as

$$\frac{M_d^{3+}}{M_i^{3+}} = \frac{X_a}{1+X_a}, \qquad M_r^{4+} = \frac{1}{2}M_d^{3+}, \tag{3.5}$$

where M_i^{3+}, M_d^{3+} and M_r^{4+} are the molar mass of the initial Mn^{3+}, the dissolved Mn^{3+} and

the remaining Mn^{4+} ions, respectively. The volume at time t can be evaluated from the molar

mass ratios of the Li^+, Mn^{3+}, Mn^{4+} and O^{2-} ions and the atomic weight ratio ($Mn/LiMn_2O_4 =$

0.304) as follows:

$$V(t) = V_i\left(1 - 0.152\frac{X_a}{X_a+1}\right), \tag{3.6}$$

where V_i is the initial volume. The changes in in the volume fraction of the cathode active

material $\left(\varepsilon_{active}\right)$ and the inert material $\left(\varepsilon_{inert}\right)$ is estimated by assuming the loss in volume

fraction is compensated by an increase in the inert volume as follows:

$$\varepsilon_{active,p} = \varepsilon_{active,p}^i\left(1 - 0.152\frac{X_a}{X_a+1}\right), \tag{3.7}$$

$$\varepsilon_{inert} = \varepsilon_{inert}^i + \varepsilon_{active}^i 0.152\frac{X_a}{X_a+1}, \tag{3.8}$$

where ε_{active}^i and ε_{inert}^i are the initial volume fractions of the cathode active material and the

inert material, respectively. Relative changes in the volume fraction in each phase results in

a decrease in the specific area, the effective conductivity (i.e., an increase in effective

resistance), and the diffusivity in the cathode. The specific surface area of the $a_{s,i}$ electrode

can be expressed as

$$a_{s,i} = \frac{3\varepsilon_{active}}{R_i}, \tag{3.9}$$

where R_s is the radius of the solid particles in the electrodes. By combining Eq. [3.7] and

[3.9], the decrease in the specific surface are can be expressed as

$$a_{s,p} = \frac{3\varepsilon_{active,p}^i}{R_s}\left(1 - 0.152\frac{X_a}{X_a + 1}\right).$$ [3.10]

The increase in the effective resistance due to the presence of the inactive Mn^{4+} in the

cathode can be expressed as

$$\sigma_{s,p}^{eff} = \left(\varepsilon_{active,p}\right)^{1.5} \sigma_{s,p}.$$ [3.11]

The Li-ion diffusion coefficient in the cathode changes due to the dissolution of the

cathode active material. An empirical relation similar to those reported in previous work

describes the decrease of the Li-ion diffusion coefficient in the cathode [154,193] as

$$D_{s,p} = D_{s,p}^i\left[1 - \left(\frac{\varepsilon_{active,p}^i - \varepsilon_{active,p}}{\varepsilon_{active,p}^i}\right)^n\right],$$ [3.12]

where $D_{s}{}^i{}_p$ is the initial solid phase diffusion coefficient, n is an empirical factor that

represents the effect of the formation of SEI on the Li-ion diffusion coefficient that can be

determined from experiments.

3.2.2 Modeling of CEI formation in the cathode

Electrolyte oxidation is recognized as the major source of film formation on the cathode.

The process could successively be driven by the reduction of unstable M^{4+} ions present in

the active electrode material [40]. This effect was clearly identified in cells with $LiMn_2O_4$

positive active material where corrosion leads to dissolution of Mn^{2+} ions into the electrolyte

and to subsequent electrolyte oxidation, which produces insoluble products [194]. The

mechanism for electrolyte oxidation is assumed to be described by the following oxidation

reaction [195]:

$$S \xrightarrow{\text{oxidation}, k_{S,1}} S_1 + H^+ + e^-, \quad [3.13]$$
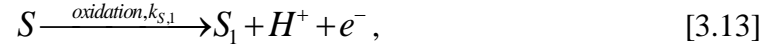
where S is the solvent, and S_1 is the overall polymer/polycarbonate products of the solvent

oxidation that form the CEI in the cathode. The rate of the solvent oxidation reaction, $R_{s,1}$,

is assumed to be a first order reaction with respect to the solvent concentration at the cathode,

$C_{s,p}$, and is expressed as

$$R_{S,1} = k_{S,1} C_{S,p}. \quad [3.14]$$

We assume that the film/electrolyte interphase is stationary during the formation of the

SEI on the cathode and that the electrode/film interphase is a moving boundary. The total

material balance on the solvent can then be expressed as

$$\frac{\partial C_{S,p}}{\partial t} - D_{S,p} \frac{\partial^2 C_{S,p}}{\partial z^2} = k_{S,1} C_{S,p}, \quad [3.15]$$

where $D_{s,p}$ is the solvent diffusivity through the SEI layer.

The boundary conditions for eqn. [3.15] at the film/electrolyte interphase and the

electrode/film interphase at the cathode are given by

$$C_{S,p} = C_{S,0} \text{ at } z = 0, \quad [3.16]$$

$$C_{S,p} = C_{S,0} e^{-k_1 t} \text{ at } z = L_p(t). \quad [3.17]$$

3.2.3 Modeling of the SEI and Mn side reactions at the anode

Since the electrolyte used in the reaction is an ethylene carbonate/ethyl methyl carbonate mixture (EC/EMC) with $LiPF_6$, we assume that the product, which forms the SEI layer, is Li_2CO_3 and that the growth of the SEI layer is one-dimensional. We also assume that the solvent species generated from the dissolution reaction at the film/electrode interphase diffuses back to the electrode/film interphase and reacts with Li ions to form the SEI layer. The formation and dissolution of SEI at the anode can be expressed as

$$S + 2Li^+ + 2e^- \xrightarrow{\;k_{S,2}\;} P + E, \qquad\qquad [3.18]$$

$$P + E \xrightarrow{\;k_{S,3}\;} S + 2Li^+ + 2e^-, \qquad\qquad [3.19]$$
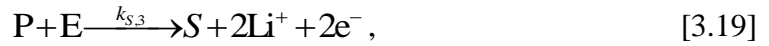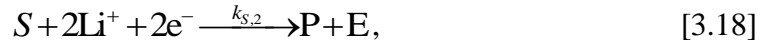
where P and E are the Li carbonate (Li_2CO_3) and ethylene (C_2H_4) products formed due to the solvent reduction reaction at the anode, respectively.

The dissolved Mn^{2+} ions are expected to be transported by diffusion and migration through a thin separator to be deposited at the anode where they are easily reduced due to the higher redox potential of Mn/Mn^{2+} (1.87 V vs. Li/Li^+) compared to the Li intercalation into graphite (< 0.3V vs. Li/Li^+). Simultaneously, the drastic decomposition of the electrolyte with Mn metal results in a remarkable capacity loss of the cell [33]. The overall reaction can be expressed as

$$S + Mn^{2+} + 2e^- \xrightarrow{\;k_{S,4}\;} S_p + Mn, \qquad\qquad [3.20]$$

where S_p denotes the products (e.g. organic manganese compounds) formed from the decomposition of the electrolyte with Mn nanoparticles. Assuming the rate of SEI formation and dissolution and the rate of solvent decomposition with the Mn metal are all first-order reactions with respect to the concentrations of their reactants, the total rate of solvent

decomposition to form SEI and organic manganese compounds at the anode can be expressed as

$$R_{S,2} = k_{S,2}C_{S,n} + k'_{S,4}C_{S,n}C_{Mn^{2+}} - k'_{S,3}C_pC_e,$$ [3.21]

where $k_{S,2}$, $k_{S,3}$, and $k_{S,4}$ are the rate constants for the SEI formation, its dissolution, and the Mn^{2+} side reaction with the SEI at the anode, respectively, and $C_{S,n}$, C_p, C_e and $C_{Mn^{2+}}$ are the concentrations of the solvent at the anode, the Li carbonate products, the ethylene products, and Mn^{2+} ions, respectively.

Assuming that the electrode/film interphase is the moving boundary in the SEI layer formation at the anode and that the film/electrolyte interphase is stationary, the total material balance of the solvent species can be expressed as

$$\frac{\partial C_{S,n}}{\partial t} - D_{S,n}\frac{\partial^2 C_{S,n}}{\partial z^2} = k_{S,2}C_{S,n} + k'_{S,4}C_{S,n}C_{Mn^{2+}} - k'_{S,3}C_pC_e.$$ [3.22]

The concentrations of ethylene and Mn^{2+} ions are assumed to be constant, so we can write $k_{S,3} = k'_{S,3}C_e$, and $k_{S,4} = k'_{S,4}C_{Mn^{2+}}$. At any point in time t,

$$C_{S,n} + C_p = \text{constant} = C_0.$$ [3.23]

Hence, equation [3.22] can be simplified to

$$\frac{\partial C_{S,n}}{\partial t} - D_{S,n}\frac{\partial^2 C_{S,n}}{\partial z^2} = C_{S,n}\left(k_{S,2} + k_{S,3} + k_{S,4}\right) - k_{S,3}C_{S,0}.$$ [3.24]

The boundary conditions for eqn. [3.24] at the film/electrolyte interphase and the electrode/film interphase at the anode are given by

$$C_{S,n} = C_{S,0} \text{ at } z = 0,$$ [3.25]

$$C_{S,p} = C_{S,0}e^{-(k_{S,2}+k_{S,3}+k_{S,4})t} - \frac{C_{S,0}k_{S,4}}{(k_{S,2}+k_{S,3}+k_{S,4})}e^{-(k_{S,2}+k_{S,3}+k_{S,4})t} + \frac{C_{S,0}k_{S,4}}{(k_{S,2}+k_{S,3}+k_{S,4})} \quad \text{at} \quad z = L(t)$$

[3.26]

The fractional amount of Li ions consumed during the formation of SEI at the anode and cathode, $x_{SEI,i}$, can be expressed as

$$x_{SEI,i}(t) = \frac{C_{S,0} - C_{S,i}}{C_{S,0}} \times 100$$

[3.27]

The thickness of the SEI film on the electrode can be calculated using the expression proposed by Sankarasubramanian and Krishnamurthy [196] and given by

$$L_{SEI}(t) = \frac{x_{SEI,i}(t)N_0}{Z_p C_p A_i},$$

[3.28]

where N_0, Z_p, C_p, and A_i are the initial number of moles of Li ions in the electrolyte, the stoichiometric coefficient of Li in the solvent oxidation and reduction reactions at the cathode and anode, the concentration of Li ions in the oxidation and reduction reactions, and the area of the electrodes, respectively.

Since the SEI film grows as the formation reactions at the anode and cathode and the electrolyte decomposition reactions occur, the resistance of the SEI film increases. Thus, we introduce a variable, R_{film}, to represent the resistance in the cathode and anode. We assume that the film resistance is a function of $x_{SEI,i}$ as follows:

$$R_{film} = R_{film,0} + R_{SEI}(t),$$

[3.29]

where $R_{film,0}$ is the initial film resistance of the SEI layer formed during the formation period, and R_{SEI} is the additional SEI layer formed during cycling and is defined as

$$R_{SEI}(t) = \frac{L_{SEI}}{\kappa_{SEI}} , \qquad [3.30]$$

where κ_{SEI} is the conductivity of SEI material formed on the cathode and anode.

The SEI film resistance also affects the surface reactions on the electrode. Hence, we modify the Butler-Volmer equation, which describes the surface reaction, to include the SEI film resistance by subtracting the effect of the SEI from the overall potential (η), defined as the potential difference between the cathode and the anode minus the equilibrium potential as follows:

$$\eta = \phi_1 - \phi_2 - U_0 - j_{film}FR_{film} . \qquad [3.31]$$

where ϕ_1 is the solid phase potential, ϕ_2 is the solution phase potential, and U_0 is the equilibrium potential.

The developed model was incorporated in the P2D model described in Table 1.1. We assume that the Mn^{3+} disproportionation reaction (Eq. 3.1) only occurs on the interface between the cathode active spinel material and the electrolyte. The SEI formation and dissolution reactions are assumed to occur on the electrode and electrolyte interfaces. All the simulations were performed at low current where the temperature across the cell does not change significantly at a given operating temperature. Hence, energy balance was not included in this model.

3.3. Parameter estimation

The numerical calculation of the model consists of two stages: the parameter extraction stage and the model prediction stage. The parameter extraction stage involves the use of literature values, experimentally determined values, values based on the cell design, and freely varying, assumed values for some of the degradation parameters. The error between the modeled and the experimental discharge profiles generated at 25 °C is estimated, and the numerical values of the assumed capacity fade parameters are then iteratively optimized to minimize this error. The Levenberg-Marquardt least squares regression method was employed to confirm the uniqueness of the convergence of the capacity fade parameters. Once the arbitrary capacity fade parameters are determined, the model then becomes

Table 3.1. Model parameters.

Parameter	Value	Parameter	Value
$L_p{}^a$	36×10^{-6} m	T_0	298 K
$L_s{}^a$	20×10^{-6} m	T	333 K
$L_n{}^a$	43×10^{-6} m	$I_{app}{}^a$	8.6 A m^{-2}
$R_p{}^a$	6.5×10^{-6} m	$x_0{}^b$	0.45
$R_n{}^a$	10.5×10^{-6} m	$y_0{}^b$	0.58
$D_{s,p,0}{}^b$	3.98×10^{-14} m^2 s^{-1}	$c_{e,0}{}^a$	1150 mol m^{-3}
$D_{s,n}{}^b$	1.14×10^{-14} m^2 s^{-1}	$\sigma_p{}^c$	10 S m^{-1}
Brugg$_p{}^c$	1.5	$\sigma_n{}^c$	100 S m^{-1}
Brugg$_s{}^c$	1.5	$E_a{}^d$	72.48 kJ mol^{-1}
Brugg$_n{}^c$	1.5	$E_{ak,p}{}^b$	25 kJ mol^{-1}
$\varepsilon_{2,p}{}^a$	0.330	$E_{ak,n}{}^b$	15 kJ mol^{-1}
$\varepsilon_{2,n}{}^a$	0.380	$E_{ad,p}{}^b$	1.2 kJ mol^{-1}
$\varepsilon_{2,s}{}^a$	0.410	$E_{ad,n}{}^b$	5.5 kJ mol^{-1}
$\varepsilon_{1,p}{}^a$	0.559	$\alpha_a{}^c$	0.5
$\varepsilon_{1,n}{}^a$	0.566	$\alpha_p{}^c$	0.5
$c_{s,p,max}{}^d$	23230 mol m^{-3}	$L_{film,p,0}{}^d$	1.6×10^{-9} m
$c_{s,n,max}{}^d$	27362 mol m^{-3}	$L_{film,n,0}{}^d$	450×10^{-9} m
R	8.314 J mol^{-1} K^{-1}	$t_+{}^c$	0.37
F	96487 C equiv^{-1}	n^b	0.045
$k_{p,0}{}^b$	9.5×10^{-11} mol$^{0.5}$ m$^{2.5}$ s^{-1}	$k_{S,2}{}^b$	1.6×10^{-8} s^{-1}

$k_{n,0}$[b]	9.8×10^{-11} $mol^{0.5}$ $m^{2.5}$ s^{-1}	$k_{S,3}$[b]	5.4×10^{-9} s^{-1}
$k_{S,1}$[b]	4.6×10^{-8} s^{-1}	$k_{S,4}$[b]	1.8×10^{-8} s^{-1}
E_1[b]	20.8 kJ mol^{-1}	E_4[b]	38.64 kJ mol^{-1}
E_2[b]	38.64 kJ mol^{-1}	$D_{s,film}$[d]	2.85×10^{-16} m^2 s^{-1}
E_3[e]	14.405 kJ mol^{-1}	κ_{film}[d]	2.4×10^{-4} S m^{-1}

[a] Parameter set in cell design
[b] Fitted parameter
[c] Obtained from COMSOL library
[d] Parameters based on literature [152,197]

3.4. Results and discussion

To solve the capacity fade model and the P2D model, numerical simulations are performed using COMSOL™ MULTIPHYSICS 5.1. An interactive smart mesh is used to discretize the three main domains using the Finite Element Method. The calculations are performed with an Intel Core ™ i7 central processing unit running at 3.30 GHz with a random-access memory of 16.1 GB.

The first set of simulations carried out to validate our model are the comparisons of the cell voltage against the normalized capacity at 25ºC and 60ºC, and selected number of cycles within a voltage range of 3.0 and 4.2 V as shown in Figure 3.1(a) and 3.1(c), respectively. Numerical fitting and optimization are used to extract the fitting parameters in both cases, and the best fits are shown in Figure 3.1(a) and 3.1(c). To quantify the deviation of the model predictions from the experimental data, we calculated the standard deviation of the predicted voltage profiles and the normalized capacities. The calculated average standard deviation between the model predictions and experimental data for the voltage profiles are indicated on Figures 3.1(a) and 3.1(c). The parameters used for the model predictions are listed in Table 3.1. The experimental data and model predictions for the capacity retention at 25 ºC and 60ºC and their estimated standard deviations are also shown in Figures 3.1(b) and 3.1(d),

respectively. The estimated standard deviations are quite small and reflect a high correlation between the model predictions and the experimental data.
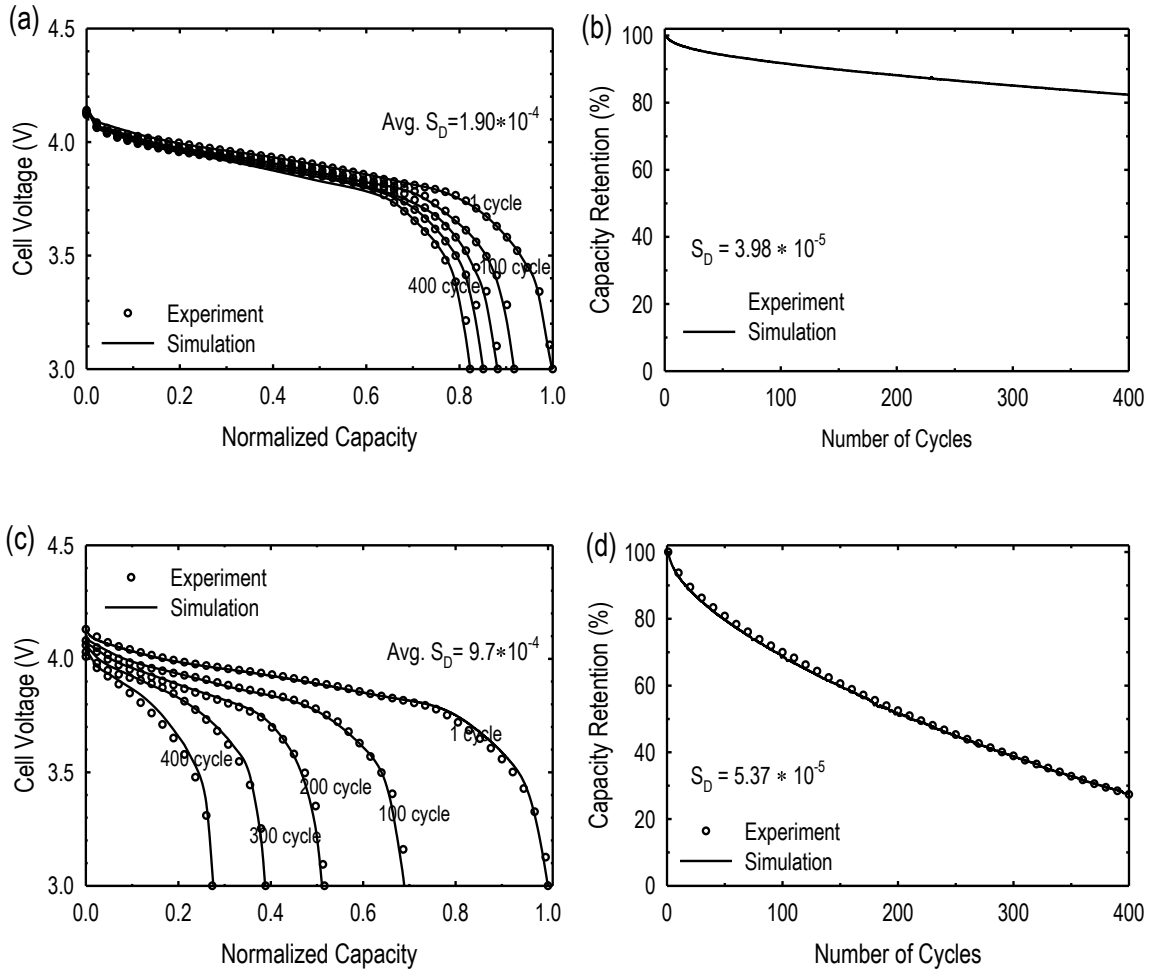
Figure 3.1. Model best fit of experimental data for (a) discharge profiles and (b) capacity retention for 400 cycles at an ambient temperature of 25 ℃, for (c) discharge profiles and (d) capacity retention for 400 cycles at an ambient temperature of 60 ℃.

The correlation between the Li-ion diffusion coefficient constant in the cathode and the number of cycles, and the change in the relative state of charge (SOC) with the number of cycles in the anode at 25 ℃ and 60℃ are shown in Figure 3.2a and 3.2b respectively. The Li-ion diffusion coefficient constant decreased from $1.34{\times}10^{-14}\,\mathrm{m^2s^{-1}}$ to

5.36×10^{-15} m^{2}s^{-1} at 25°C and from 1.22×10^{-14} m^{2}s^{-1} to 2.43×10^{-15} m^{2}s^{-1} at 60°C after 400 cycles. A decrease in the Li-ion diffusion coefficient constant increases concentration polarization, which causes capacity loss in Li-ion battery. This effect is more severe at the higher temperature due to the high rate of dissolution of Mn^{2+} and to the precipitation of the electrolyte-decomposed products in the cathode, resulting in the rapid formation of the cathode electrolyte interphase (CEI). The formation of the CEI due to Mn dissolution reaction and the precipitation of the electrolyte decomposition products retards the transportation of Li ions and decreases the effective Li-ion diffusion coefficient constant. The measured Li-ion diffusion coefficient constant in spinel $LiMn_2O_4$ as reported by Zhang et al. [198] decreased from 9.65×10^{-14} m^{2}s^{-1} to 5.78×10^{-14} m^{2}s^{-1} after 100 galvanostatic cycles with a cut-off voltage range between 3.4 V and 4.4 V as inferred through Warburg impedance analysis. Das et al. [199] observed a similar phenomenon when they studied the kinetics of Li ions diffusion in a $LiMn_2O_4$ thin film electrode using cyclic voltammetry and potential step chronoamperometry measurements. They reported that a solid electrolyte interface formed on the electrode and that this passive layer caused a decrease in the Li-ion diffusion coefficient constant, which reduced the observed capacity.

The relative SOC decreases as the number of cycles increases in Figure 3.2b. The amount of Li ions available for cycling is consumed by the decomposition reaction of the electrolyte to the form the SEI at the anode. After each cycle, the amount of Li ions decreases by a small amount especially after the formation and the stability processes. Nevertheless, the loss rate of usable Li ions becomes more pronounced after many cycles. The SOC was calculated using the relation below.

$$SOC = \frac{\int\limits_{neg} c_{s,n} dS}{c_{s,n\max} L_{neg}}$$ [3.32]
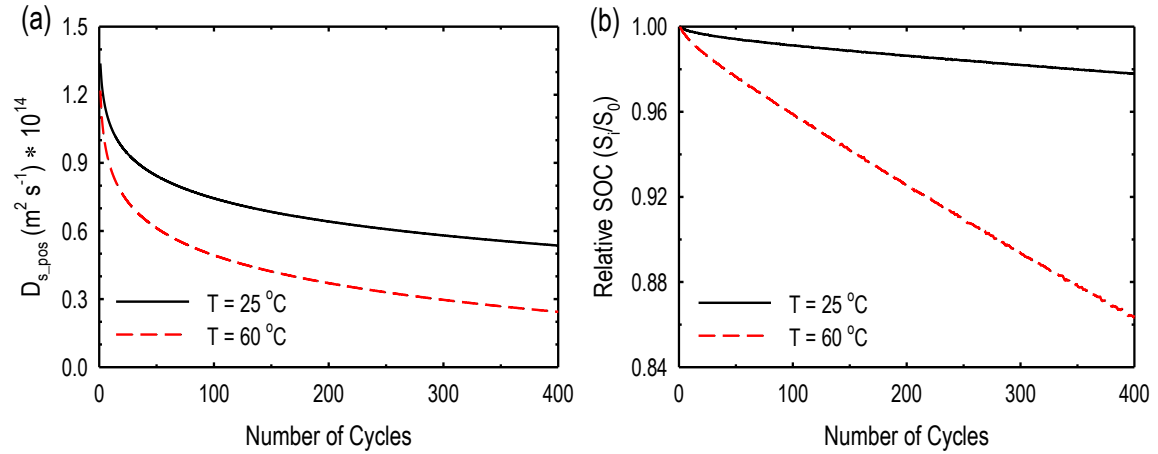
Figure 3.2. Correlation between (a) the Li ion diffusion coefficient constant in the cathode and (b) the relative state of charge (SOC) in the anode as a function of number of cycles at 25 ºC and 60ºC.

Figure 3.3 shows the concentration profile of the solvent species at the film/electrode interphase in both cathode and anode during 400 cycles at 25ºC and 60ºC. The concentration of the solvent species decreases as the cycle number increases with a greater loss rate in the anode. The greater loss rate of solvent in the anode can be attributed to the electrochemical reduction of the Mn^{2+} on the surface of the graphite, which was preceded by the critical decomposition of electrolyte with Mn nanoparticles. Komaba et al. [200] reported the same process experimentally when they investigated the Li-ion intercalation into graphite using a graphite/Li half-cell with electrolyte containing Li and Mn salts in order to clarify their influence on the carbon electrode using cyclic voltammetry. The authors suggested that the presence of reduced Mn on the surface of the graphite could act as an organic catalyst that accelerates the rate of electrolyte decomposition resulting in extreme capacity fading of the cell. At a higher temperature, this effect was more pronounced due to the high rate of Mn^{2+}

dissolution at the cathode coupled with a high rate of electrolyte decomposition with Mn nanoparticles at the anode.
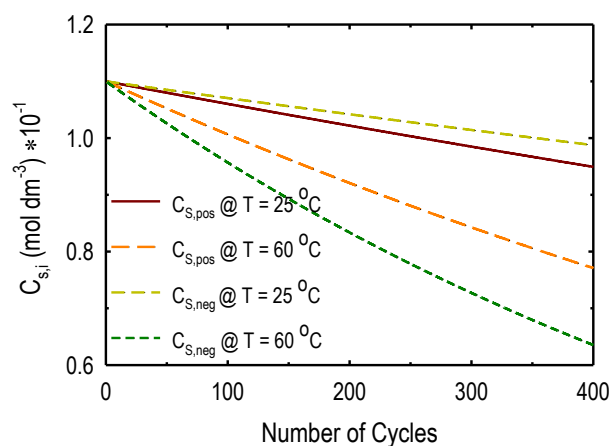
Figure 3.3. Concentration profile of the solvent species at the film/electrode interphase for both the cathode and the anode during 400 cycles at 25 ºC and 60 ºC and a voltage range of 3.0–4.2 V.

The variation in the film resistance with the number of cycles in both the cathode and the anode are presented in Figure 3.4(a) and 3.4(b), respectively. The film resistance increases with an increase in cycle number. Higher film resistance is observed at a higher temperature and higher cut-off potential due to the high rate of Mn^{2+} dissolution. For the higher cut-off voltage, the rate constant for Mn dissolution was increased by a factor of 1.3, which was obtained by fitting the model prediction of the cycle performance to the experimental data. The initial film resistance observed in the cathode and anode in Figure 4(a) and 4(b), respectively, are different because different initial thicknesses were adopted based on the experimental values recorded after pre-cycling [201,202]. The oxidation reaction occurring at the cathode-electrolyte interface limits the cell performance by consuming electrolyte continuously, which continuously increases the cathode SEI thickness as cycling

proceeded. The rate at which the film resistance increases in the anode is observed to be greater than that in the cathode. The rapid increase of the film resistance in the anode can be attributed to the additional thickness of the SEI layer due to deposited Mn as reported experimentally by Zhan et al. [182].
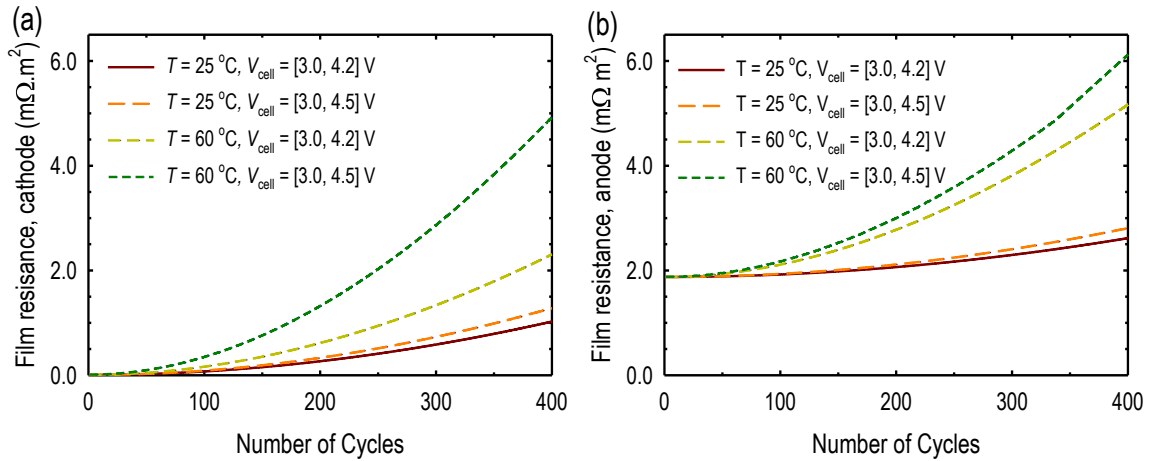
Figure 3.4. Film resistance at the end of the discharge vs. number of cycles in (a) the cathode and (b) the anode at ambient temperatures of 25 ℃ and 60 ℃ and a voltage range of 3.0–4.2 V.

Figure 3.5 shows the changes in the relative volume fraction of the active material in the cathode with cycle number in four case studies. The relative volume fraction of the cathode decreases as the number of cycles increases because of the dissolution of Mn^{2+} from the active material into the electrolyte. At an ambient temperature of 25℃, the relative volume fraction of the cathode decreases slowly, indicating a slow rate of Mn^{2+} dissolution, while the relative volume fraction of the spinel cathode decreases rapidly at an ambient temperature of 60℃, due to a high rate of Mn^{2+} dissolution. Lei et al. [201] have already reported the same effect in experiments where they studied the changes in SEI layer thickness and $LiMn_2O_4$ electrode thickness upon cycling using in-situ spectroscopic ellipsometry. From their study, they found that the $LiMn_2O_4$ electrode thin film decreases

linearly with cycle number. Similarly, as shown in Figure 3.5, the relative volume fraction decreases rapidly when the cell is cycled at a large voltage range between 3.0 and 4.5 V compared to when the cell is cycled at a relatively smaller voltage range between 3.0 and 4.2 V for a given ambient temperature. The acceleration of the decrease in volume fraction can be attributed to the increase in the rate of Mn^{2+} dissolution for the high voltage range and to the difference in the operating time.
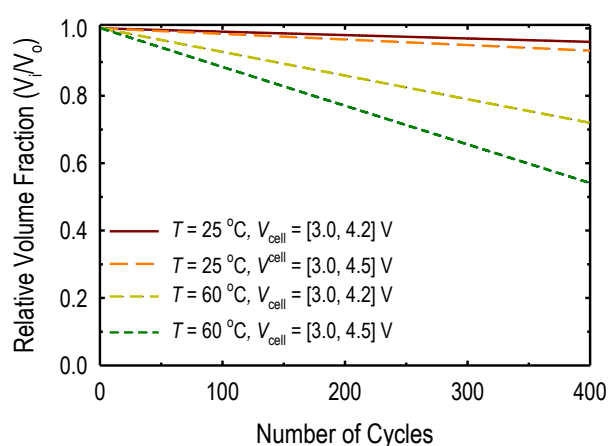
Figure 3.5. Relative volume fraction of the active cathode material at the end of the discharge versus the cycle number at ambient temperatures of 25 ℃ and 60 ℃ and two selected voltage ranges of 3.0–4.2 V and 3.0–4.5 V.

Figure 3.6 shows the variation in cell capacity retention over 400 cycles with two different voltage ranges from 3.0 to 4.2 V and from 3.0 to 4.5 V, and with different ambient temperatures of 25 ℃ and 60℃, and the model best fit of the capacity retention at a voltage range of 3.0 to 4.5V. From Figure 3.6a, charging the cell to a voltage of 4.5 V causes an extreme capacity fade compared to charging the cell to 4.2 V at a given ambient temperature. The rate constant for Mn^{2+} dissolution was treated as a fitting parameter in Figure 3.6b. The value increased by a factor of 1.3 as compared to the initial value used for describing the cycle performance at a voltage range of 3.0 to 4.2V. This factor is comparable to the rate of

increase in the concentration of Mn^{2+} dissolved into the electrolyte when $LiMn_2O_4$ cells were cycled at 3.5 to 4.23V and 3.5 to 4.5V as reported by Xia et al. [180]. In addition, a number of researchers have reported severe capacity fading when Li-ion batteries are overcharged [107]. From the observations of Aurbach et al. [107], cells cycled at an overcharge state of 4.5 V resulted in greater Mn^{2+} dissolution than those cycled at 4.2 V as measured using X-ray diffraction and electroanalytical techniques. As the ambient temperature is increased to 60 °C, the initial capacity for a given voltage range is slightly higher than that at an ambient temperature of 25 °C but the capacity fades more quickly. This rapid loss of capacity at an ambient temperature of 60 °C is due to the acceleration of the Mn^{2+} dissolution in the cathode, to the increase in the SEI thickness at the anode, and a change in the SEI structure at the anode. Wang et al. [203] have also reported acceleration of the Mn^{2+} dissolution rate at an elevated temperature results in severe capacity fade.
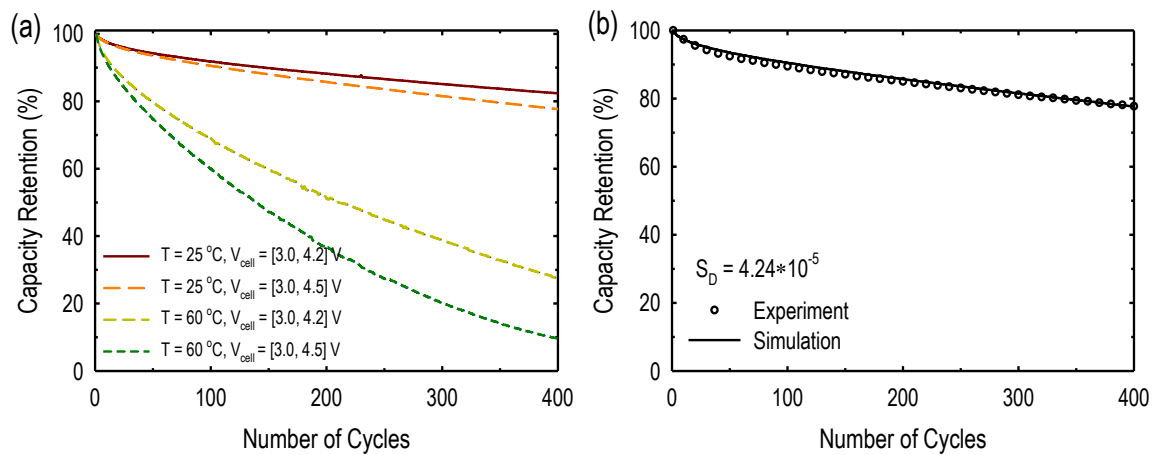
Figure 3.6. (a) Changes in the cell capacity retention over 400 cycles with different voltage ranges of 3.0–4.2 V and 3.0–4.5 V at different ambient temperatures of 25 ºC and 60 ºC and, (b) Model best-fit of experimental data for capacity retention after 400 cycles at an ambient temperature of 25 ºC and a voltage range of 3.0 to 4.5V.

In order to examine the effect of different discharge rates on the rate of capacity fading, we simulated the cycle performance of Li-ion batteries at discharge rates of 1C, 2C, and 3C at an ambient temperature of 25ºC with a voltage range from 3.0 to 4.2 V as shown in Figure 3.7. The rate of capacity fading is faster for the cell system cycled at 2C and 3C discharge rates than the system cycled at a 1C discharge rate. The initial discharge capacity of the cell system cycled at a 3C discharge rate is reduced by ~30% after 400 cycles, while the cell systems cycled at 1C and 2C discharge rates are reduced by ~18% and 24%, respectively. These simulation results are comparable to those obtained by Ning et al. [204], who studied the capacity fade of Li ion batteries (active material $LiCoO_2$) at different discharge rates. The capacity losses they recorded after 300 cycles using discharge rates of 1C, 2C and 3C were 9.5%, 13.2%, and 16.9%, respectively. These values are smaller than those predicted by our model, probably due to the additional contribution to the capacity fade from Mn^{2+} dissolution of the $LiMn_2O_4$ cathode active material, the acceleration of the electrolyte decomposition from the deposited Mn nanoparticles on the anode, and the higher number of cycles.
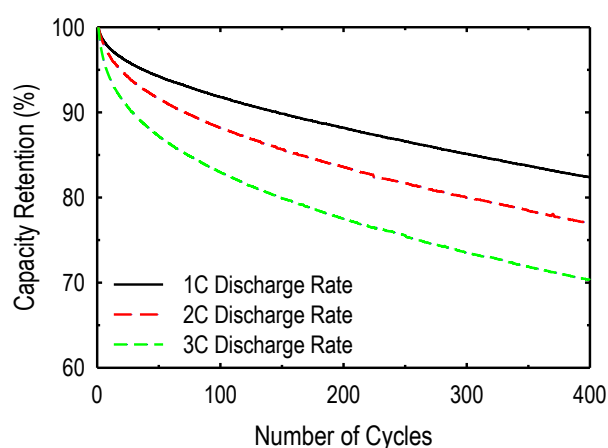
Figure 3.7. Cycle performance at different discharge rates of 1C, 2C, and 3C at an ambient temperature of 25 ºC with a voltage range of 3.0–4.2 V.

Figure 3.8a and 3.8b show the relative contribution of the SEI, CEI and Mn^{2+} dissolution toward the reduction of the capacity in the spinel $LiMn_2O_4$/graphite cells corresponding to the results in Figure 3.1 at 25 and 60 ºC respectively. The SEI contribution is significantly higher as compared to the CEI and Mn dissolution at an ambient temperature of 25 ºC for all number of cycles. While at an ambient of temperature of 60 ºC, the SEI is paramount at the beginning of the cycling and steadily reduces as cycling proceeds in Figure 3.8b. On the other hand, the contribution of the Mn^{2+} dissolution to the capacity fade is small at the beginning but increases linearly with cycling at both ambient temperatures of 25 ºC and 60 ºC. Narayanrao et al. [156] made a similar observation. Based on the simulation results, the SEI, CEI and Mn^{2+} dissolution contributed to ca. 53, 20 and 27 % of the total capacity fade at an ambient temperature of 25 ºC respectively while at an ambient temperature of 60 ºC they contributed 36, 16 and 48 % respectively. This is comparable to experimental results reported by Xia et al. [180] when they investigated the cycle life behavior of $Li/LiMn_2O_4$ cells.
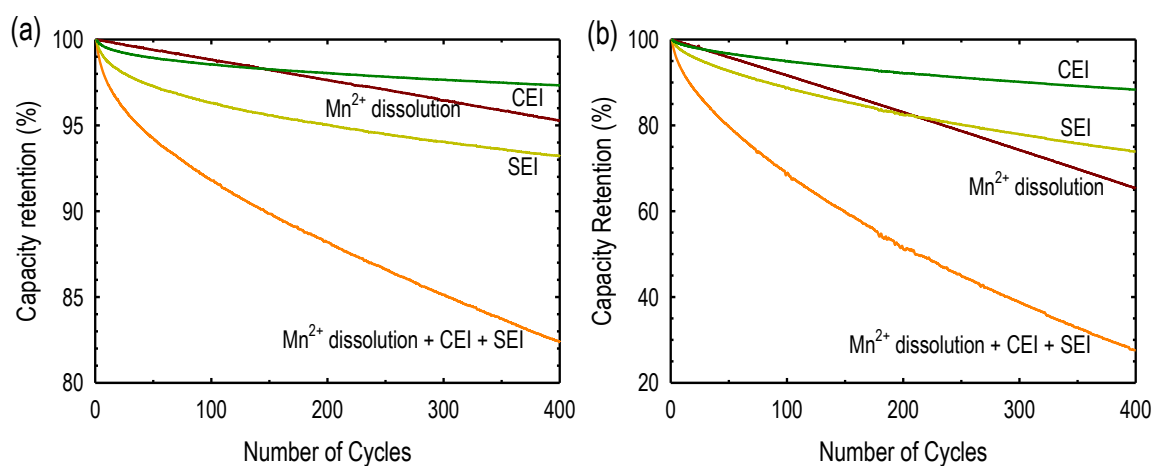
Figure 3.8. Relative contribution of the solid-electrolyte interphase (SEI) at the anode, cathode-electrolyte interface (CEI) and Mn^{2+} dissolution in the cathode to the total capacity fade corresponding to the results in Figure 3.1 at (a) an ambient temperature of 25 ºC and (b) an ambient temperature of 65 ºC.

3.5. Conclusion

A capacity fade model for a spinel-based cathode and artificial graphite anode is developed in this chapter. The model is incorporated into the P2D model Framework in COMSOL Multiphysics, and the capacity fade at different ambient temperatures of 25ºC and 60ºC within two selected voltage ranges from 3.0 to 4.2 V and from 3.0 to 4.5 V is studied. The model considers the formation and dissolution of SEI at the anode, Mn dissolution in the spinel-based active material, electrolyte decomposition, and the formation of SEI in the cathode. The dissolved Mn^{2+} in the electrolyte possibly deposits on the anode, resulting in excessive decomposition of the electrolyte and hence an increase in the SEI thickness. The inactive Mn^{4+} also remains in the solid phase and leads to an increase in the effective resistance. Furthermore, the increase in SEI thickness on the anode and cathode leads to an increase in cell resistance as cycling proceeds. The model in its present state reasonably fits the variation of discharge profiles for different sets of charge-discharge cycles with a negligible standard deviation. Case studies demonstrate that the end of charge voltage (EOCV) and the ambient temperature are critical factors responsible for capacity fading of spinel-based cathode and artificial graphite Li ion batteries. This model could potentially be applied to other cell chemistry with a different cathode active material.

Chapter 4

Application of capacity fade model: Accelerated cyclic aging analysis

4.1 Introduction

In addition to determining the cost, safety, specific energy, power, and reliability issues, lifetime prediction for LIBs under real operating conditions is a major step for dependable integration of LIBs into vehicles and stationary applications, and to eliminate warranty issues. Accelerated aging tests have been regarded as a powerful alternative to replace the cost- and time-intensive aging tests under real-life operating conditions [205,206]. However, many experiments still need to be performed to obtain the maximum operating conditions at which the aging test can be performed without altering the decay mechanisms. In addition, cycle-life prediction models must be used to project the data gathered from accelerated aging tests for estimates of cycle life under real-life conditions.

From previous reports, there is a linear or nonlinear relationship between the capacity fade and the number of cycles in a cycle-influenced capacity fade of LIBs [207,208]. Hence, the mechanisms constituting the nonlinearity must be carefully addressed when developing a capacity fade model. In this regard, a physico-chemical model (PCM) will be suitable as compared to a semi-empirical model. The capacity fade model developed in the previous chapter exhibits such qualities since the capacity fading of $LiMn_2O_4$/graphite cells is a nonlinear function of the number of cycles.

The concept of using temperature as a stress factor for an accelerated aging test has been

employed in previous works [205,206,209,210]. However, most of these previous works concentrate on studying the effect of temperature on the capacity fade mechanism of the specific cell chemistry being used. As an illustration, using an electrochemistry-based model, Leng et al. [210], conducted a thorough study on the effects of temperature on the aging characteristics of cycled LIBs at 25 and 55 °C. However, the authors failed extrapolate the data obtained at 55 °C to that of room temperature. In addition to that, the range of temperatures considered therein, were not enough to develop an empirical model for the extrapolation of the data to normal operating conditions of LIBs. On the other hand, Guan et al. [205], studied the aging behavior of commercial $LiCoO_2$/mesocarbon microbeads cells cycled at different temperatures. Therein, the capacity deteriorated rapidly at high temperature and the capacity retention of the cells cycled at 45 °C was about a quarter of those cycled at 25 °C. Thus, the authors compared their results at elevated temperature to that of room temperature. The authors after comparing their results also concluded that, at an operating temperature of 45 °C, the aging process of the cells deviates from that at room temperature. Nevertheless, for an accelerated aging test based on the principles of time-temperature superposition, the degradation mechanism should not be altered, thus a wide range of temperatures should be considered in estimating the upper temperature limit, which is time consuming.

In an effort to reduce the number of experiments involved in determining the upper temperature limit required for the accelerated cycle test based on the principle of time-temperature superposition, we propose a new framework. In this framework, we used our developed PCM coupled with the P2D model (also known as the porous composite electrode model (PCEM)) (PCM-PCEM) to predict the cycling performance of $LiMn_2O_4$/graphite cells at different temperatures. The PCM–PCEM predictions at the various temperatures of

25, 35, 45, 55, and 60 °C were quantified and used to build a simple empirical life model (SELM). Based on the evaluated values of the fitting parameters using a nonlinear least square method, the maximum temperature limit required for the accelerated cycling test of the LiMn$_2$O$_4$/graphite cells was determined.

A large part of the work presented in this Chapter was published in [211].

4.2 Methodology

The main objective here is to build a framework that can perform an accelerated cyclic aging analysis based on the principle of time-temperature superposition with less experimental data. The detailed proposed framework is summarized in Figure 4.1 and can be described as follows. The experimental discharge profiles and the capacity retention obtained from coin cells cycled at 25 and 60 ˚C and at a current rate of 1C is used to validate a coupled PCM–PCEM model designed to describe the capacity fade mechanism of LiMn$_2$O$_4$/graphite system. The validated PCM–PCEM model is then used to predict the cycling performance at different temperatures and at a current rate of 1C. The PCM-PCEM was well described in the previous chapter. The validated PCM–PCEM model prediction provides enough data for the development an SELM using a parameter estimation technique. The SELM is used to extrapolate the number of cycles obtained at the various temperatures to those at 25 ˚C.
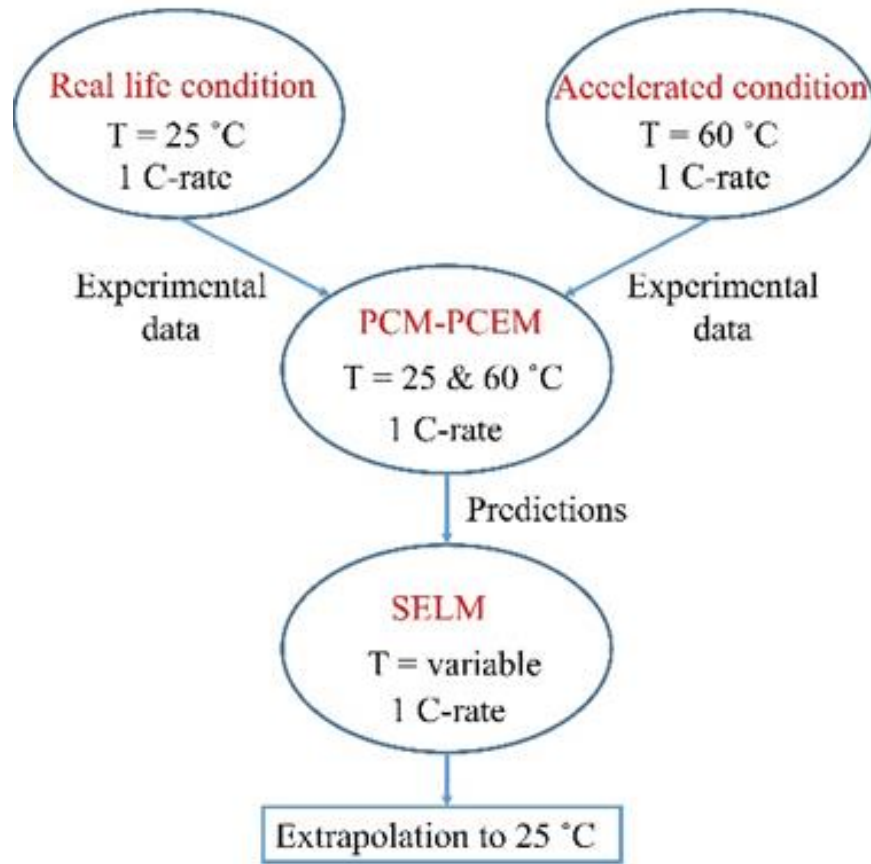
Figure 4.1. Summary of proposed accelerated cyclic aging analysis framework

4.2.1 Experimental data collection

The experimental data for the PCM-PCEM validation were obtained from 2032 coin-type full cells. The electrode and cell making process are similar to those described in the previous chapter. After aging the cells for 12 h, we proceeded with the formation step that involved cycling the cells at a charge/discharge constant current (CC) rate of 0.1C at 25 °C. The cells were then stabilized at a charge/discharge rate of 0.2C for three cycles. The cycling performance of the cells were conducted at 1C constant current (CC) charging rate and 1 C constant current-constant voltage (CC-CV) discharging rate at 25 and 60 °C. 1C rate means the current is 1.32 mA cm^{-2}. The resting time between the charge and discharge was 10 min. The charge-discharge cycles were conducted between 4.2 V and 3.0 V.

4.2.2 Simple empirical life model (SELM) development

The PCM–PCEM predictions were used to quantify the rate of capacity fade for the development of SELM. The functional form of the SELM in terms of the percentage capacity loss Q_{loss} can be expressed as

$$Q_{\text{loss}} = f\left(N_{\text{cycle}}, T\right)$$
[4.1]

where N_{cycle} denotes the number of cycles, and T is the operating temperature for the cycling.

Since only the number of cycles and temperature affects the capacity fade, we adopted a previously developed battery-life model [135] in which the capacity fade depends on time and temperature, and simplified Eq. (4.1) into

$$Q_{\text{loss}} = k\left(T\right) \cdot N_{\text{cycle}}^{z}$$
[4.2]

where $k(T)$ is the capacity-fade constant as a function of T, and z is the power-law factor

4.3 Results and discussion

To study the influence of temperature on the capacity fading of the LiMn$_2$O$_4$/graphite cells, the cells were cycled at 25 and 60 °C and the results are presented in Figure 4.2. The cells cycled at 60 °C reached almost half of their initial discharge capacity, which deviates from that of the cells cycled at 25 °C, whose capacity retention was ~90% of the initial discharge capacity. The fatal capacity fade of the cells at 60 °C compared to those at 25 °C can be mainly attributed to the high dissolution of Mn^{2+} from the cathode into the electrolyte at elevated temperatures [177,212].
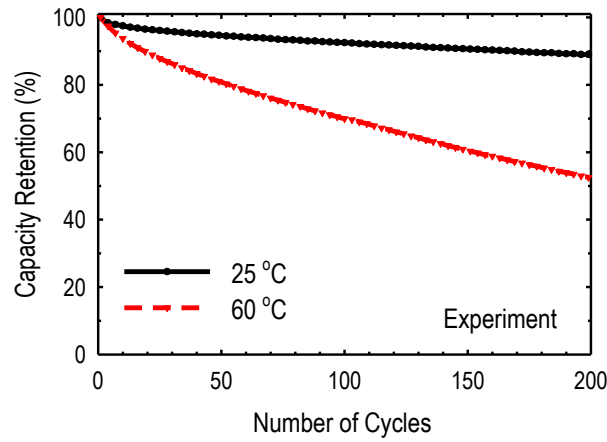
Figure 4.2. Experimental results of discharge-capacity retention of $LiMn_2O_4$/graphite cells cycled at temperatures of 25 and 60 ºC, with upper and lower cut-off voltages of 3.0 and 4.2V.

The experimental data obtained at the two temperatures were used to validate the simulations performed using PCM coupled with the PCEM equations. This coupled model equations, hereafter referred to as PCM–PCEM, were solved by performing numerical simulations using COMSOL Multiphysics 5.2 (COMSOL, Inc., USA). The cycle performances and the discharge profiles were simultaneously simulated with the PCM-PCEM model equations, respectively. The model validation was performed by comparing the experimental cell-voltage curves obtain at 25 and 60 °C to those of the PCM–PCEM predictions for the 1st, 20th, 100th, and 200th cycles, with lower and upper cut-off voltages of 3.0 and 4.2 V, respectively. The fitting parameters were extracted via numerical fitting and optimization; the best fits to the experimental voltage profiles are shown in Figure 4.3a and 4.2c. The average standard deviations of the predicted voltage curves and normalized capacities from the experimental data were calculated, and they are also shown in Figure 4.3a and 4.2c. The simulation parameters are the same as those in Table 3.1. Figure 4.3b and 4.2d show, the experimental and simulated capacity retention, as well as their

standard deviations, at 25 and 60 °C, respectively. The estimated standard deviations are small indicating a high correlation between the model predictions and the experimental results.
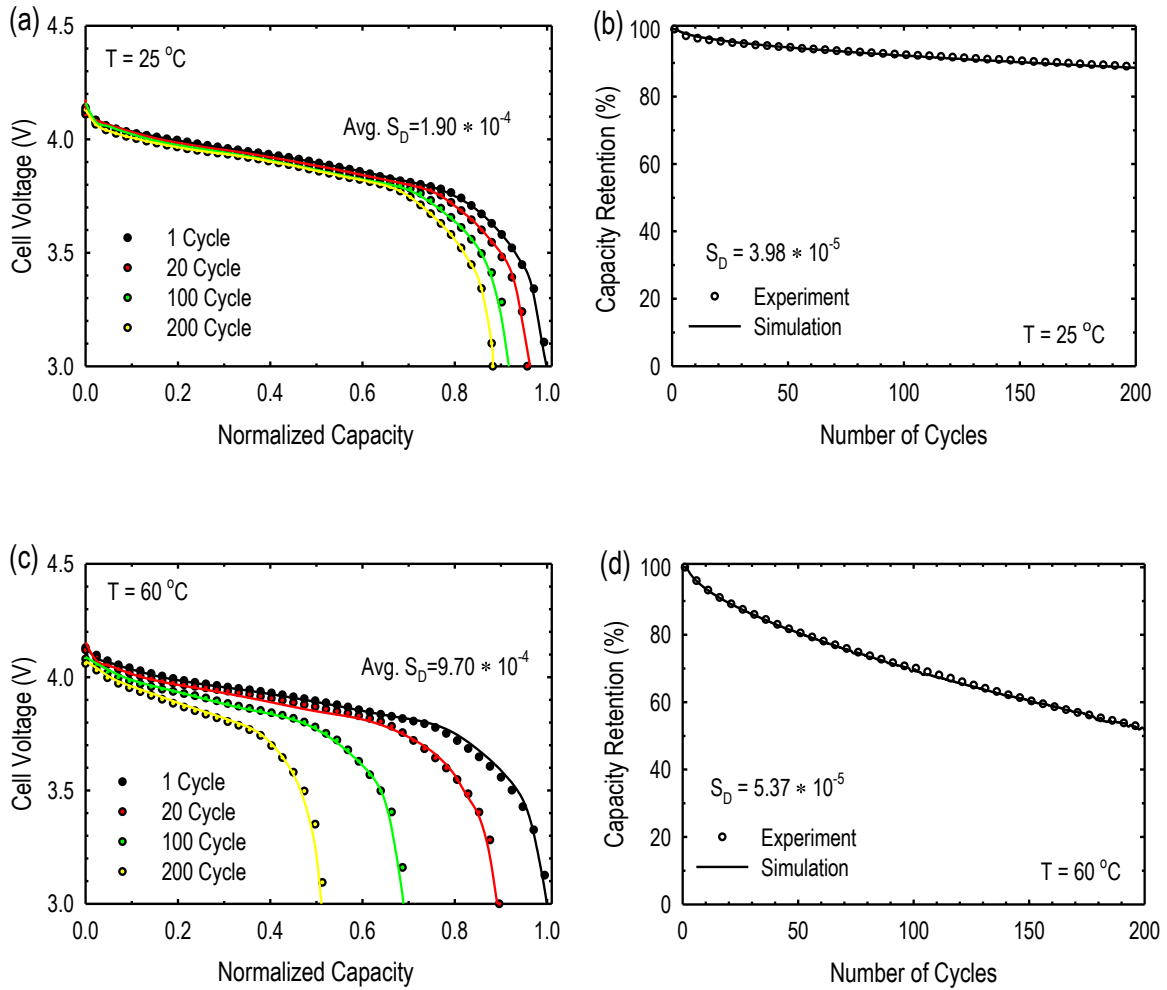
Figure 4.3. Model best fit to experimental data: (a) discharge profiles (b) capacity retention over the course of 200 cycles at a temperature of 25 ℃ (c) discharge profiles (d) capacity retention over the course of 200 cycles at a temperature of 60 ℃.

The validated model was used to predict the cycling performance of the LiMn$_2$O$_4$/graphite cells at various temperatures, with lower and upper cut-off voltages of 3.0 and 4.2 V. The outcome of the prediction is presented in Figure 4.4a. The rate at which the

capacity faded in the simulated results increased with increasing temperature. The rapid capacity fading as the temperature increased can be ascribed to the increase in the rate of Mn dissolution and the precipitation of the products of the decomposed electrolyte on the cathode, leading to a rapid formation of the CEI, which slows down the movement of Li ions. This effect leads to a reduction in the Li-ion diffusion coefficient constant as shown in Figure 4.4b. Figure 4.4c and 4.3d demonstrate the dependency of the CEI and SEI resistance on temperature. The CEI and SEI resistance increased with temperature with SEI resistances being higher than CEI resistances. The reduced Mn nanoparticles catalytically facilitate electrolyte decomposition, which leads to an increase in the SEI resistance, and contribute to the fatal capacity fade [200]. Moreover, as reported in the experimental study of Zhan et al., an increase in both the CEI and SEI resistance also contributes to the capacity fade, and the rate of increase was found to be dependent on temperature [182].
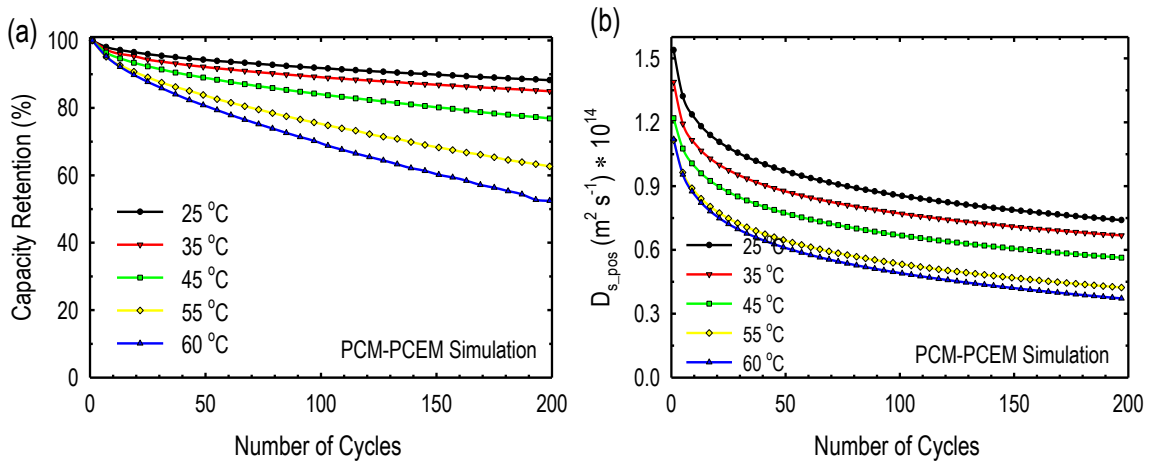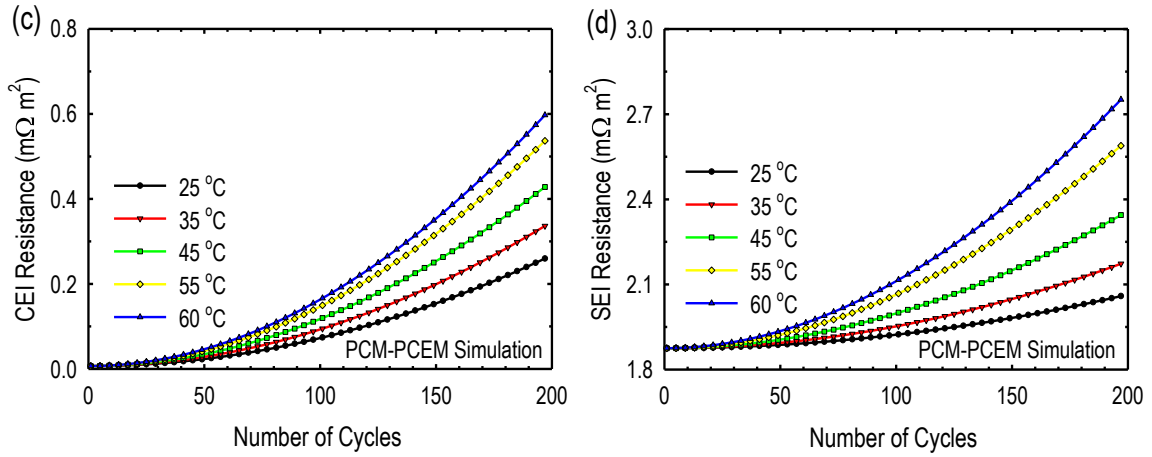
Figure 4.4. Simulated (a) cycling performance of the LiMn$_2$O$_4$/graphite cells, (b) diffusion coefficient constant of the cathode, (c) cathode electrolyte interphase (CEI) resistance and (d) solid electrolyte interphase (SEI) resistance, at various temperatures.

Figure 4.5 illustrates the percentage capacity loss plotted as a function of the number of cycles at 25, 35, 45, 55, and 60 °C. The solid lines represent the best fit of the SELM, while the symbols represent the data extracted from simulation results using PCM–PCEM at each temperature. To ensure a good agreement between the simulations using SELM and the coupled PCM–PCEM, a nonlinear least-square technique known as the Levernberg–Marquardt method was used to fit the SELM prediction to that of the PCM–PCEM simulation, with $k(T)$ and z as the fitting parameters. The values of the fitting parameters at various temperatures are presented in Table 4.1.

Table 4.1. Equations for predicting the accelerated capacity-fade at different temperature

Temperature (°C)	Life model
25	$Q_{loss} = 0.830 \times N_{cycle}^{0.5000}$
35	$Q_{loss} = 1.139 \times N_{cycle}^{0.5010}$
45	$Q_{loss} = 1.437 \times N_{cycle}^{0.5245}$
55	$Q_{loss} = 1.639 \times N_{cycle}^{0.5912}$

60                                    $$Q_{loss} = 1.695 \times N_{cycle}^{0.6300}$$
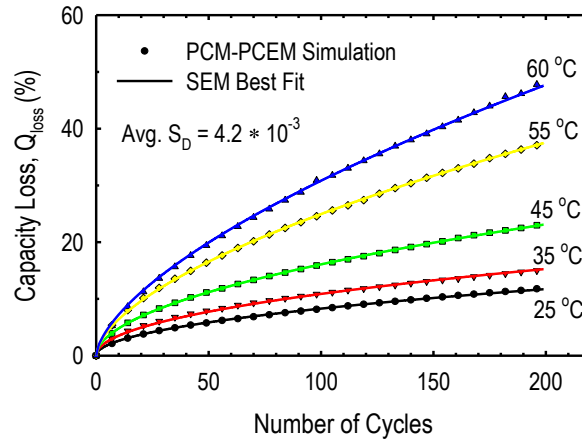
Figure 4.5. Simulations using a simple empirical cycle-life model (SELM) (solid line) and that of the coupled model, PCM–PCEM, (symbols) at 25, 35, 45, 55, and 60 °C at a discharge rate of 1C.

The dependence of the capacity-fade constant and that of the power-law factor on temperature are shown in Figure 4.6a and 4.5b, respectively. In Figure 4.6a, the solid line represents the best fit of the Arrhenius equation to the extrapolated values of k from the SELM fittings. The effect of temperature on the capacity-fade parameters is manifested as an Arrhenius-type dependence for the capacity-fade constant, with an activation energy of E_a of 263.5 J mol^{-1} and a pre-exponential factor of 2.889. The low magnitude of E_a indicates that the factors responsible for the capacity fade include not only a chemical process, as in the case of LiCoO$_2$/graphite cell [159], but also other physical processes, as described in the PCM. The values of z at 25, 35, and 45 °C were determined from Figure 4.6b to be approximately 0.5, which correlate with a dependence on the square-root of time (number of cycles). Previous studies [136,159] showed that the reliance of capacity fade on the square root of time is an indication that the irreversible capacity loss is because of SEI growth that consumes active Li ions, and it is often a diffusion-controlled process. However, further

increases in temperature to 55 and 60 °C yielded power-law factors of ~0.59 and ~0.63, respectively. These values indicate that at temperatures greater than or equal to 55 °C, the capacity-fade mechanisms are no longer dominated by SEI growth, but by other factors such as Mn dissolution, as previously demonstrated by both experimental [180] and modeling [192] approaches.
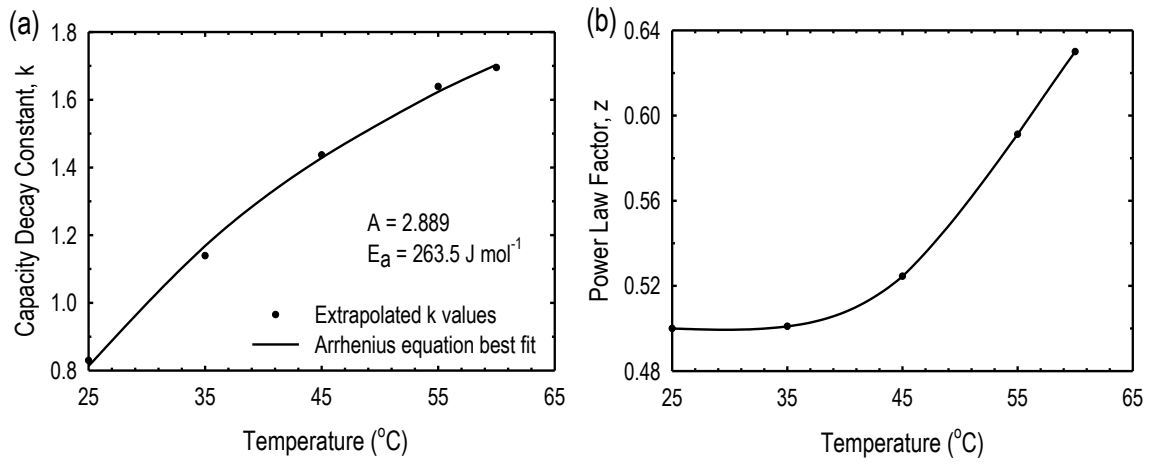
Figure 4.6. Dependence of (a) capacity-fade constant (k), and (b) power-law factor (z) on temperature. The capacity-fade constant is fitted to the Arrhenius equation (solid line in (a)).

Owing the large potential window considered in this study, a comparison between the model predictions and the experimental data using the discharge profiles alone is not enough to claim that the model effectively replicated the electrochemical behavior of the cells. Thus, we conducted a qualitative analysis of electrochemical voltage spectroscopy on the experimental and simulated discharge profiles and presented the results in Figure 4.7. The model predictions overlap quite well with experimental data with a low standard deviation (Figure 4.7a and 4.6b). The various experimental peaks are well matched with those of the model predictions. This indicate that the electrochemical characteristics of the $LiMn_2O_4$/graphite cells are well replicated by the PCM-PCEM as suggested by Barai et al. [116]. Figure 4.7c shows the predicted incremental capacity (IC) as a function of cell voltage

at different temperatures and at an equivalent capacity. At 25, 35 and 45 ˚C, the IC curves

showed similar peaks at the same voltage. However, there were additional peaks at 3.6 V

for the cells cycled at 55 and 60 ˚C. Thus, the capacity-fading mechanisms are similar at 25,

35, and 45 ˚C but changes as the temperature increases above 45 ˚C. In addition, since the

IC curves are the same for a temperature range of 25 to 45 ˚C, the cycling aging was

accelerated without changes in the degradation mechanisms [116]. This confirms the results

obtained based on the calculated values of z in eq. (4.2).
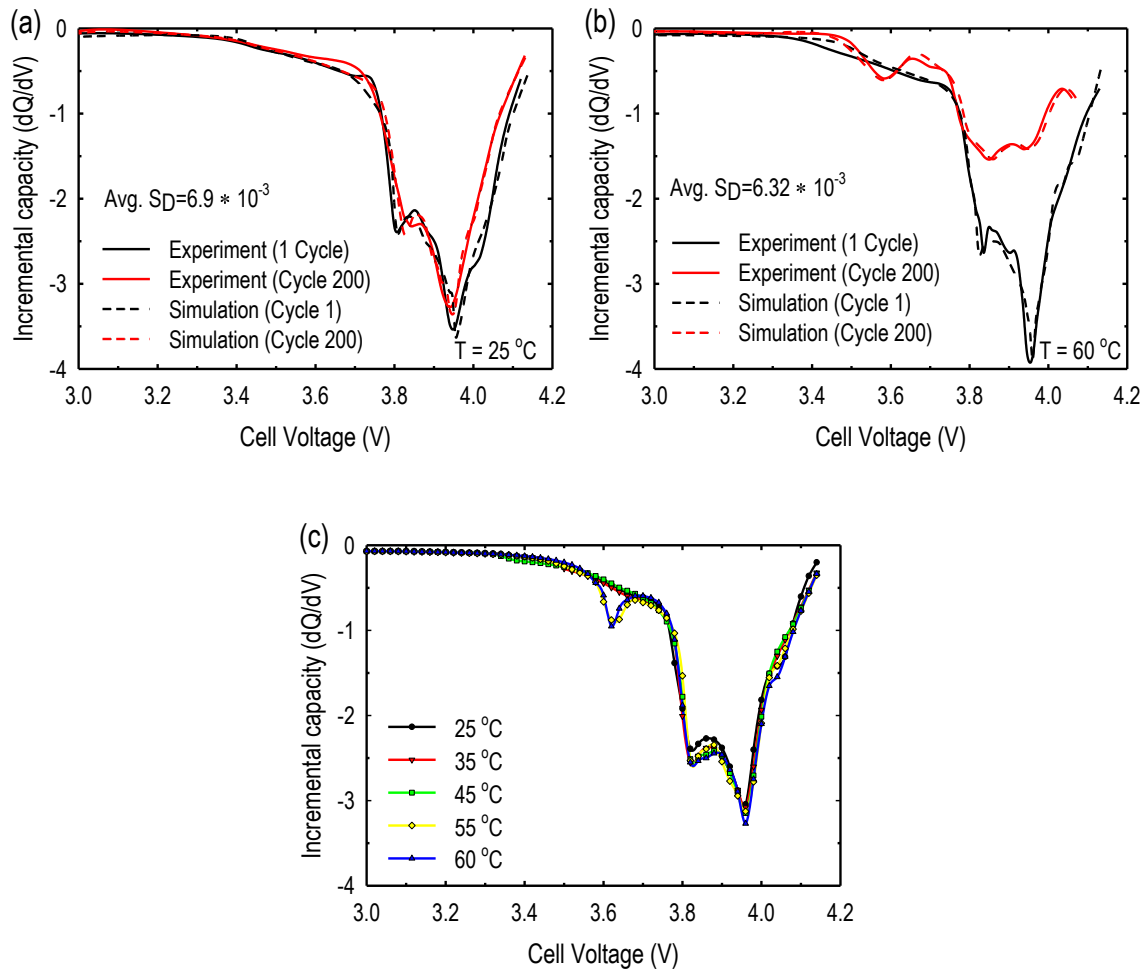
Figure 4.7. Qualitative analysis of electrochemical voltage spectroscopy for experimental

and PCM-PCEM prediction of cells cycled at (a) 25 ˚C (b) 60 ˚C and (c) at different

temperatures and similar capacities.

In this study, we adopted the time–temperature superposition accelerated testing method for our analysis. This method is based on the premise that if a higher temperature accelerates but does not change the degradation mechanisms, then the testing duration can be reduced by testing at higher temperatures [159]. However, this method is bound by the upper temperature limit that a cell can be subjected to without altering the degradation mechanisms. Estimation of z by fitting the SELM to either experimental data or an experimentally validated PCM-PCEM with negligible standard deviation and estimation of IC curves can be an effective way to determine the upper limit of the temperature that is appropriate for time–temperature superposition accelerated analysis. Therefore, it can be clearly inferred from Table 4.1 that the maximum temperature suitable for accelerated cyclic aging analysis without altering the capacity-fade mechanisms is 45 °C. However, a significant increase in z occurs at 55 and 60 °C, indicating a significant alteration in the capacity-fading mechanisms. This result agrees well with the experimental results reported by Broussely et al. [60]. Nevertheless, we used our developed SELM to predict the accelerated number of cycles at 55 and 60 °C, as well as those at 35 and 45 °C. Figure 4.8 shows a plot of the predicted accelerated number of cycles as a function of the number of cycles at 25 °C. As expected, the accelerated number of cycles decreases with an increase in temperature. However, it should be noted that at temperatures of 55 and 60 °C, the capacity-fade mechanisms are altered and, therefore, are not suitable for predicting the accelerated number of cycles. At the upper temperature limit of 45 °C, the number of cycles can be reduced by a factor of ~3.6, and it can be reduced by a factor of ~1.7 at 35 °C.
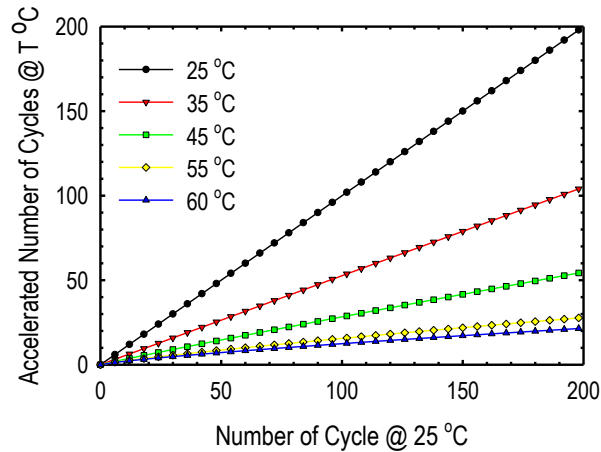
Figure 4.8. Predicted number of cycles at 25, 35, 45, 55, and 60 °C as a function of the number of cycles at 25 °C.

4.4 Conclusion

We proposed a simple but time-effective accelerated cyclic aging analysis framework using a coupled PCM-PCEM to predict the life cycle performance of Li ion batteries at different temperatures. An SELM was then used to extrapolate the obtained data at higher temperatures to real life operating conditions. The accelerated aging analysis technique can be applied to any Li ion battery system with capacity mechanism like that of $LiMn_2O_4$/graphite, and different systems as well with slight modification. The capacity-fading mechanisms based on the extrapolated z values (0.5) strongly depended on the SEI formation at temperatures ranging from 25 to 45 °C. At higher temperatures, the z values are well above 0.5, indicating that another mechanism other than SEI formation are dominant. The accelerated number of cycles is reduced by a factor of 3.6 at the upper temperature limit of 45 °C for the time–temperature superposition accelerated testing of the $LiMn_2O_4$/graphite cells. This work will serve as a guide for battery engineers and scientists who wish to use temperature as a parameter for accelerated cycle-life prediction.

Chapter 5

Capacity fade analysis of anode materials with huge volume expansion

5.1 Introduction

As one of the most promising anode material candidates to be used in LIBs, Si has a relatively higher theoretical specific capacity (3579 mAh g^{-1}) as well as other advantages such as environmental friendly and terrestrial abundance [213–215]. However, large volume expansion (up to 275 %) of silicon during (de)lithiation particles, formation of unstable solid electrolyte interphases (SEIs), and permanent capacity losses, [213,216,217] hinders the commercialization of silicon anode material for LIBs as mentioned in Chapter 1. One of the method adopted to address this issue is the coating of the current collector with an adhesive interlayer such as polydopamine (PD) thin film to prevent the delamination of the composite electrode [218]. Nevertheless, the analytical and quantitative effect of the presence of the PD thin film on the surface of the copper current collector on the capacity-fading mechanisms of Si anodes are complex and not well understood. The analyses and quantification of the role of the polydopamine interlayer on the degradation processes will improve the prediction of the cell capacity during operations.

In this chapter, we extended the non-destructive capacity-fading analysis method used in Chapter 2 to Si-based anodes with different adhesion strength between the composite electrode and the current collector. The main objective of this work was to identify the degradation mechanisms, and to study the effect of the PD thin film on the long-term cycle

performance of Si-based anode LIBs. Similar to the capacity fade analysis method used in Chapter 2, we adopted the P2D model to analyze the cycle performance of Li ion cells made with Si anode and Li metal and a bare and PD-treated copper current collectors via a parameter estimation technique. Based on the estimation of the parameters that change with cycling, the various mechanisms associated with the capacity fade in the bare and PD-treated copper current collector were investigated. A quantitative analysis of the aging mechanism of Si-based anodes in terms of Li ions loss is performed and discussed for the two cell configurations. The percentage contributions of the various identified mechanisms were estimated for the cells with the bare and PD-treated copper current collector. By extrapolating the parameters that changed with cycling, the maximum number of cycles required for the complete deterioration of the limiting cell configuration in terms of cycle performance were determined.

A large part of the work presented in this Chapter was published in [219] and presented at the Electrochemical Conference on Energy and the Environment (ECEE 2019) held at Glasgow, Scotland.

5.2 Experiment

5.2.1 Treatment of Cu current collector with Polydopamine

The coating process described by Ryou et al. [220] was adopted to coat the PD on the Cu current collector. The mixture used to make the dopamine solution (2 mmg mL^{-1}) contained Tris buffer solution (pH 8.5, 10 mM) and methanol (CH3OH/buffer = 1/1 wt%).

5.2.2 Preparation of Electrode

The composition of the slurry used to make the Si electrode was 60 wt% Si active material (30 nm; Nanostructured & Amorphous Materials, Inc, Houston, USA), 20 wt% conductive material (Super-P, Timcal, Switzerland) and 20 wt % poly (acrylic acid) (MW = 450,000; Sigma-Aldrich, South Korea) binder in deionized water. The prepared slurry was casted onto the bare current collector (8 μm; Iljin Materials, South Korea) and PD-treated Cu current collector using a doctor blade and dried in a convection oven at 80 ˚C for 2 h. The loading level and thickness of the Si electrode were controlled to 0.53 mg cm^{-2} and 8 μm respectively.

5.2.3 Assembling of cell

2032 coin half-cells were fabricated with the prepared Si electrodes (diameter: 12 mm; dried in a vacuum oven at 60 °C for 12 h before use), Li metal (450 μm; Honjo Metal Co., Japan) as the counter electrode, and a polyethylene separator ((ND420, Asahi Kasei, Japan). The porous part of the separator was filled with a liquid electrolyte (1.15 M LiPF6 in ethylene

carbonate/ethyl methyl carbonate; EC/EMC = 3/7 vol%; Panax Etec, South Korea). The electrolyte contained 5 wt% fluoroethylene carbonate (Panax Etec, South Korea). The coin cells were assembled in an argon-filled glove box with constant dew point less -80 ℃.

5.2.4 Measurement of electrochemical performance

The assembled coin cells made of were aged for 12 h prior to the evaluation of the formation step and cycle performance using a battery tester (PNE Solution, South Korea). The cells were cycled between 0.05 and 2.0 V at a constant current density of 0.2 A g^{-1} at room temperature during the formation step. The cells were then cycled at a constant current density of 1.2 A g^{-1} for 500 cycles.

5.3 Results and discussion

5.3.1 Parameter Estimation

The parameters that change with cycling were estimated by fitting the physics-based model predictions of the voltage profile to those of experimental data obtained from 2032 coin-type cells consisting of silicon electrodes prepared with bare and polydopmine-treated (PD-treated) Cu current collectors at some selected number of cycles. The fittings were done using a nonlinear least square regression technique, the Levernberg Marquardt method. The results of the fitting are shown in Figure 5.1. The symbol and the solid lines represent the experimental data and model predictions, respectively. The model predictions were executed using the parameters in Table 5.1. There is a high correlation between the model predictions and the experimental voltage profiles as confirmed by the lower values of the estimated average standard deviation shown in Figure 5.1.

Table 5.1. Model parameters used in this study

Symbol	Parameters	Value
L_p	Si electrode thickness, μm [a]	8×10^{-6}
L_n	Li metal electrode thickness, μm [a]	450×10^{-6}
L_s	Separator thickness, μm [a]	20×10^{-6}
r	Si particle radius, m [a]	30×10^{-9}
ε_e	Volume fraction electrolyte [a]	0.73
$D_{s,p}$	Diffusion coefficient constant of Li in Li$_x$Si, m^2 s^{-1} [d]	3×10^{-16}
D	Diffusion coefficient constant of Li in electrolyte, m^2 s^{-1} [c]	3.93×10^{-10}
k_n	Reaction rate constant on Li metal, mol$^{0.5}$ m$^{-0.5}$ s [c]	6.2×10^{-6}
K_1	Electronic conductivity of Si electrode, S m^{-1} [d]	33
k_p	Reaction rate constant on Si electrode, m$^{2.5}$ mol$^{-0.5}$ s^{-1} [b]	2×10^{-12}
c_{smax}	Maximum Li concentration, mol m^{-3} [d]	3.11×10^5
α_c	Cathodic apparent transfer coefficient [b]	0.26
α_a	Anodic apparent transfer coefficient [b]	0.74
R_{film}	Film resistance, Ω m^2 [d]	4.7×10^{-4}
A	Geometric area of Si electrode, m^2 [a]	1.131×10^{-4}

[a] Parameter set in the cell design
[b] Fitted parameter
[c] Obtained from COMSOL library
[d] Parameters based on literature [32]
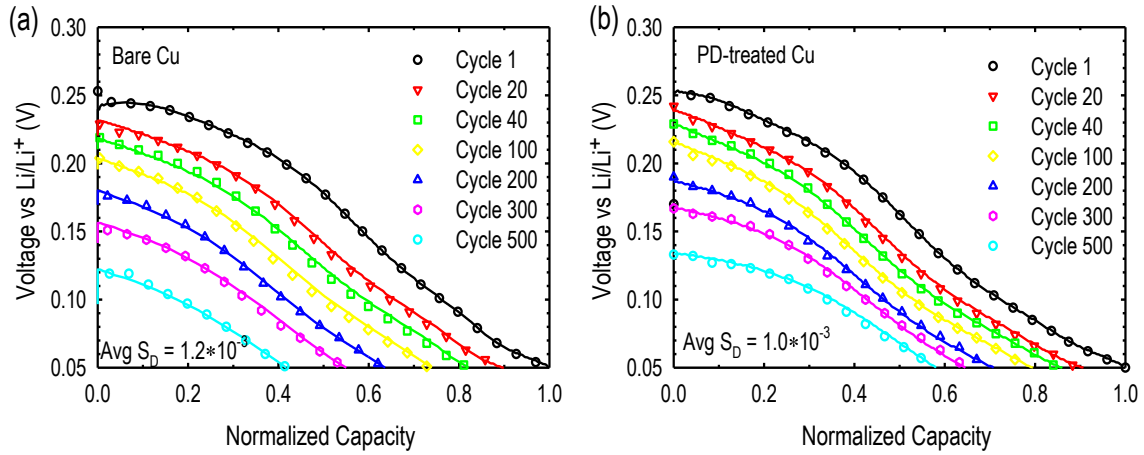
Figure 5.1. Comparison of experimental discharge profiles and P2D model predictions for Si/Li half-cells with (a) bare Cu current collector and (b) (PD)-treated Cu current collector. The symbols and the solid lines represent the experimental data and model predictions, respectively.

To achieve the high correlation between the physics-based model predictions and the experimental voltage profiles of the two cell configurations considered in this study, an optimization technique, which employs the non-linear least square method, was used to estimate the parameters that changed with cycling. For the cells with the bare Cu current collector, three parameters changed with cycling. These parameters are the total film resistance (R_{film}), the initial state of charge ($x_{0,Si}$) of the silicon electrode, and the maximum Li ion concentration in silicon electrode ($c_{max,Si}$). On the other hand, in addition to the three parameters that changed with cycling for the cells with the bare Cu current collector, the reaction rate constant (k_{Si}) varied with cycling for the cells with the PD-treated Cu current collector. The variations in the parameters with cycling for the two cell configurations are shown in Figure 5.2. The total resistance increased monotonically with cycling and was higher in the cells with the bare Cu current collector compared to the cells with PD-treated Cu current collector (Figure 5.2a). The film resistance is the sum of the resistance due to the SEI and that due to the contact between the silicon composite material and the Cu current collector. Moreover, the initial SOC of the silicon electrode ($x_{0,Si}$) increased with cycling for the two cell configurations (Figure 5.2b). The rate of increase was high during the initial stages of the cycling but reduces as the cycling proceeds and eventually becomes almost constant at the later part of cycling. The rate of increase was higher for the cells with bare Cu current collector relative to the cells with PD-treated Cu current collector. Figure 5.2b indicates that the silicon electrode becomes less discharged with cycling. The maximum Li ion concentration of silicon for the two cell configurations also increased with cycling and it was higher for the cells with bare compared to the cells with the PD-treated Cu current collector (Figure 5.2c). The increase in the maximum Li ion concentration can be attributed to the additional supply of Li ions from the reference Li metal electrode as cycling

progressed. Lastly, the reaction rate constant also decreased with cycling for the cell with the PD-treated Cu current collector but remains constant for the cells with the bare Cu collector (Figure 5.3d). This was due to the insulating nature of the polydopamine interlayer and a detailed discussion will be given in the subsequent section. The changes in the film resistance (contact) reflects the mechanical degradation while that in the initial SOC reflects both chemical (SEI formation) and mechanical degradation (Li ions loss due to particle isolation).
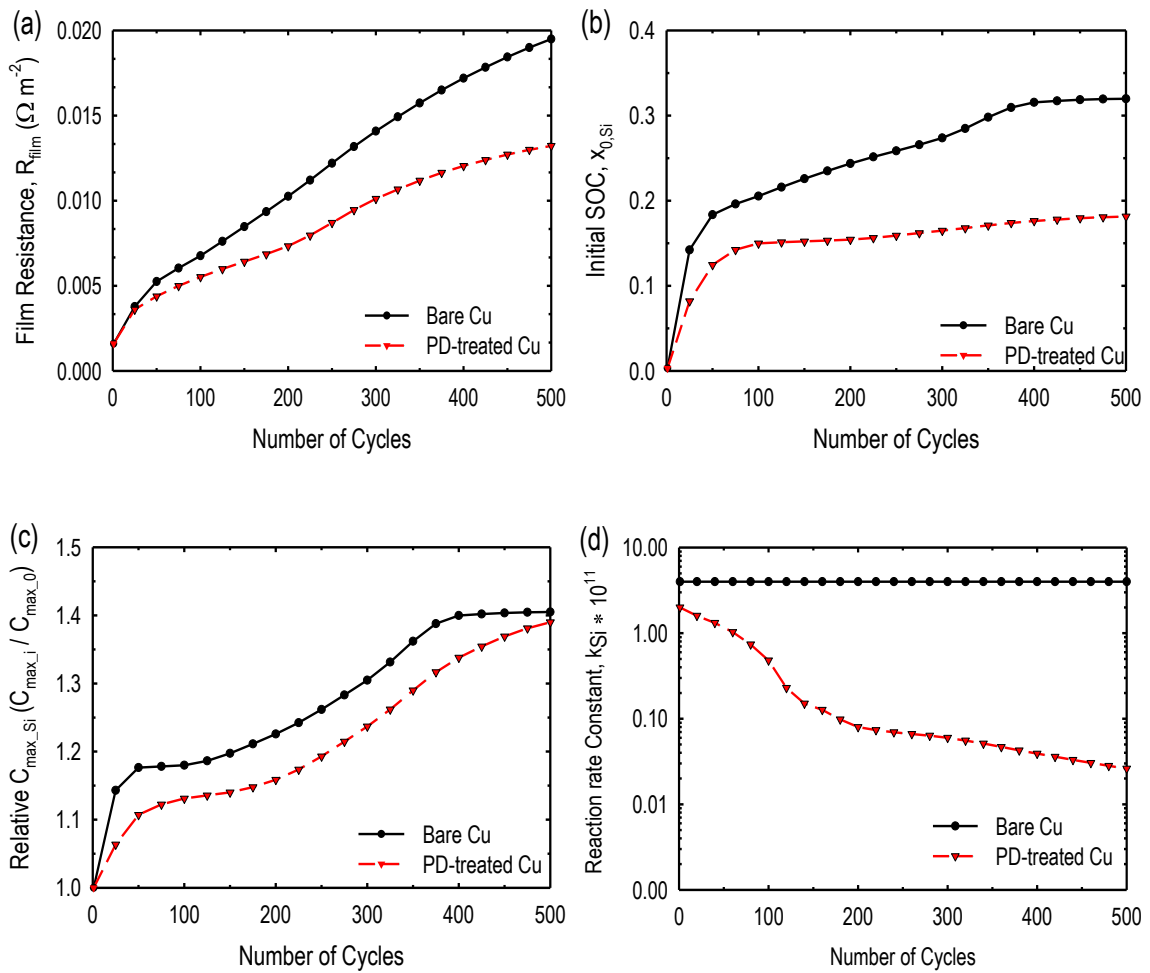
Figure 5.2. The changes of model parameters with cycling (obtained from fitting the experimental voltage profiles for each cycle).

The predicted SOCs of the silicon electrode at the end-of-charge (EOC) (x_{Si}) for the cells with bare and PD-treated Cu current collectors is shown in Figure 5.3. At EOC, the silicon electrode in both cell configurations becomes less charged (x_{Si} decreases). The rate at which the SOC at EOC decreased was high during the initial cycles (1 to 40) but reduced at midway (40 to 400) through the cycling and became lesser at the later part of cycling (400 to 500). The PD interlayer did not have any significant effect on the rate at which the silicon electrode became less lithiated at the end of the 500 cycles.
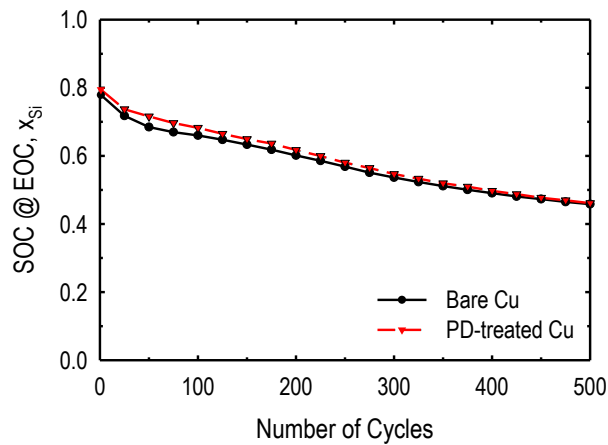
Figure 5.3. The simulated SOCs for the Si/Li half-cells with bare and polydopamine (PD)-treated Cu current collectors at the end of charge (EOC).

5.3.2 Model Predictions

To conduct further analysis beyond the 500 cycles, we tried to predict the cycle performance of the cells with bare and the PD-treated Cu current collectors at higher number of cycles by extrapolating the model parameters that change with cycle number to 1000 cycles. The parameter extrapolation was done based on the assumption that the capacity-fading mechanism remained the same during the period of the predictions. The extrapolated model parameters are presented in Figure 5.4.
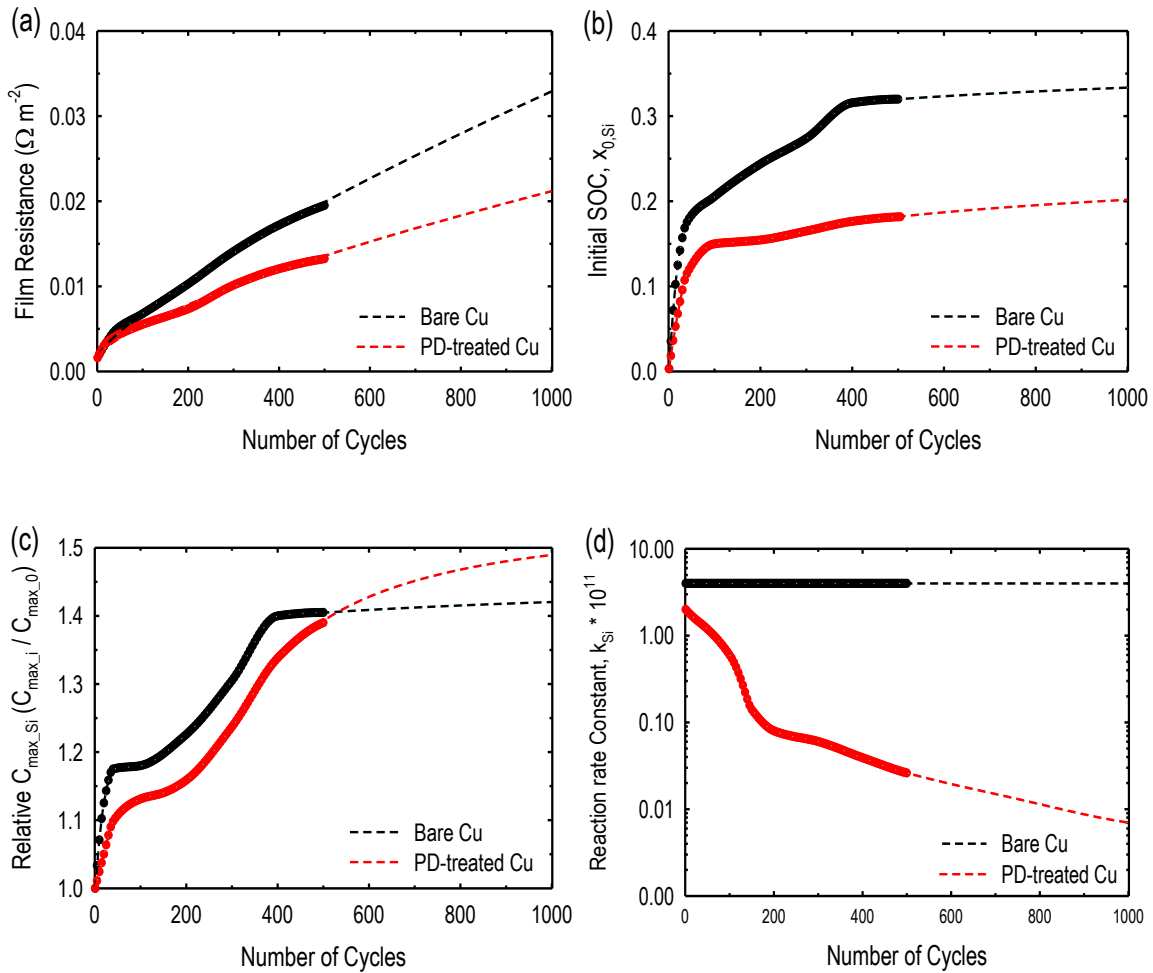
Figure 5.4. The extrapolation of the physics-based P2D model parameters that changed with cycling in Figure 5.2. The extrapolations were obtained using the curve-fitting tool in Matlab.

The extrapolated model parameters in Figure 5.4 were used to predict the cycle performance of the cells with bare and PD-treated Cu current collectors. The outcomes of the predictions are shown in Figure 5.5. A comparison between the experimental normalized charge capacity retention and the model predictions during the first 500 cycles for the two cell configurations are presented in Figure 5.5. There was a good match between the experimental data and model predictions. In addition, a prediction of the normalized charge capacities using an empirical model (Table 5.2) is shown in Figure 5.5. A stage of

accelerated capacity deterioration is predicted after ca. 690 cycles for the cells with the bare Cu current collector (Figure 5.5a). This is in agreement with previously published experimental results by Mazouzi et al. [221], where they observed a drastic capacity decay for Si/Li cell after 700 cycles. A continuous accelerated capacity decay is predicted for the cells with PD-treated Cu current collector. The shape of the capacity fade pattern predicted in Figure 5.5b is similar to that observed experimentally by Song et al. [222].

Table 5.2. Empirical model expressions and parameters

Cell Design	Model	A	B	C	D
Bare Cu	$Ax^B + Cx + D$	−0.1659	0.1973	−0.0004228	1.193
PD-treated Cu	$Ax^B + Cx + D$	−0.0299	0.4861	0.0003641	1.026
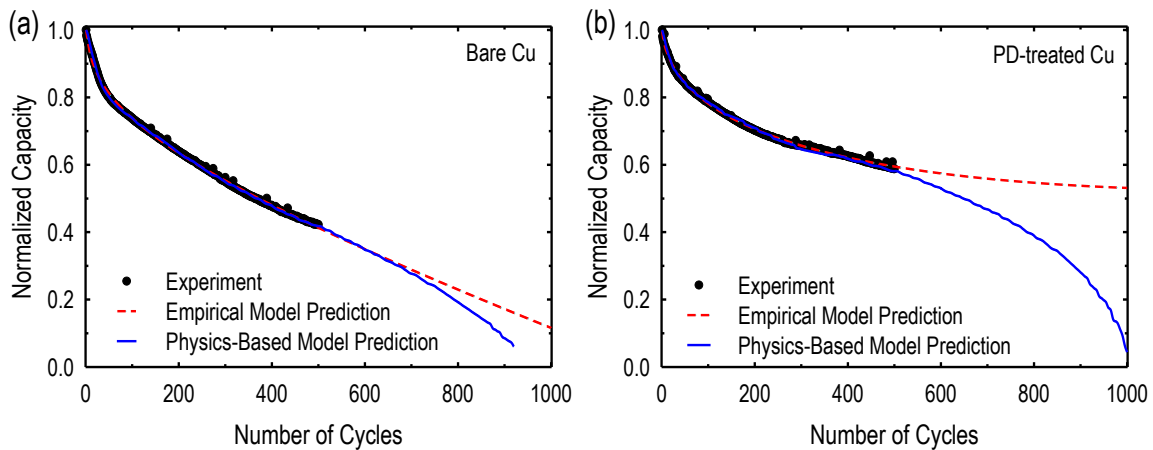
Figure 5.5. Comparison of the normalized charge capacity as a function of number of cycles predicted by the physics-based model and empirical model for the Si/Li half-cells with (a) bare and (b) PD-treated Cu current collectors.

Figure 5.6 shows the simulated silicon electrode SOC at the EOC for cells with bare and PD-treated Cu current collectors using the extrapolated model parameters in Figure 5.4. The SOC at EOC decrease steadily for both cell configurations. The prediction did not show any significant changes in the SOC at EOC for the extended number of cycles. Thus, the capacity-mechanisms remained the same as that predicted during the initial 500 cycles. The

capacity fade of the two cell configurations will be analyzed using the information obtained from the physics-based model.
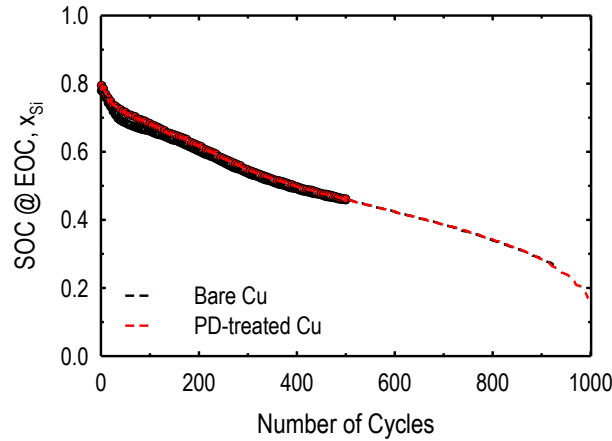
Figure 5.6. The predicted SOCs for the bare and PD-treated Cu current collectors at the EOC using the extrapolated physics-based model parameters presented in Figure 5.4. The symbols show the SOC at EOC in Figure 5.3.

5.3.3 Capacity fade analysis

The results presented in the previous sections suggests that, the presence of the PD interlayer between the silicon composite electrode and the Cu current collector has a significant positive effect on the capacity fade of Li/Si cells. In this section, we try to discuss the phenomenon constituting these effects.

The study performed on the parameters that change with cycling shows that, the film resistance increases with cycling for both cell configurations with the rate of increase being higher in the cells with bare Cu current collector (see Figure 5.2). Here, the film resistance is the sum of the resistance due to the formation of the SEI and the contact resistance between the silicon composite electrode and the Cu current collector. However, since the cells with both bare and PD-treated Cu, current collectors have silicon as their anode active material;

there will be no significance difference between the increases in resistance due to the formation of SEI. Thus, the main difference between the film resistance of the bare and PD-treated Cu current collector can be attributed to the different contact resistances between the silicon composite electrode and the Cu current collector. Cho et al. [218] have demonstrated this experimentally, where they attributed the improvement in the cycle performance of the cells with PD-treated Cu current collector, to the enhanced adhesion strength between the silicon composite electrode and Cu current collector. The increase in the adhesion strength resulted in a lower contact resistance as demonstrated in Figure 5.2.

In addition, many previous reports have been made on the occurrence of side reactions on silicon electrodes during (de) lithiation processes [223–226]. These side reactions are known to consume Li ions resulting in the formation of the SEI on the surface of the Si electrode. Two types of SEI have been reported to form during the (de) lithiation processes [227]. First is the formation of diethyl 2,5-dioxahexane dicarboxylate (DEDOHC) during the early stage of cycling when 1M LiPF6/EC: DEC (1:2 v/v) electrolyte is used. The DEDOHC is known to be non-conductive and increases the impedance of the cell. The co-product of the formation of DEDOHC, Li propionate also traps Li ions contributing to low columbic efficiency of the cell. In this work, we used 1.15 M LiPF6/EC: EMC (3:7 v/v) electrolyte. Hence the SEI product formed, assuming that the formation mechanism is like that of DEDOHC, will be ethyl methyl 2,5-dioxahexane dicrarboxylate (EMDOHC) which is assumed to have similar properties as the DEDOHC. Second is the formation of lithium ethylene dicarbonate (LiEDC), when lithiated silicon is exposed to the electrolyte because of crack formation owing to volume expansion in silicon electrodes. The formation of the two types of SEI leads to the loss of cyclable Li ions. The mechanism for the formation of the EMDOHC and LiEDC can be described as,
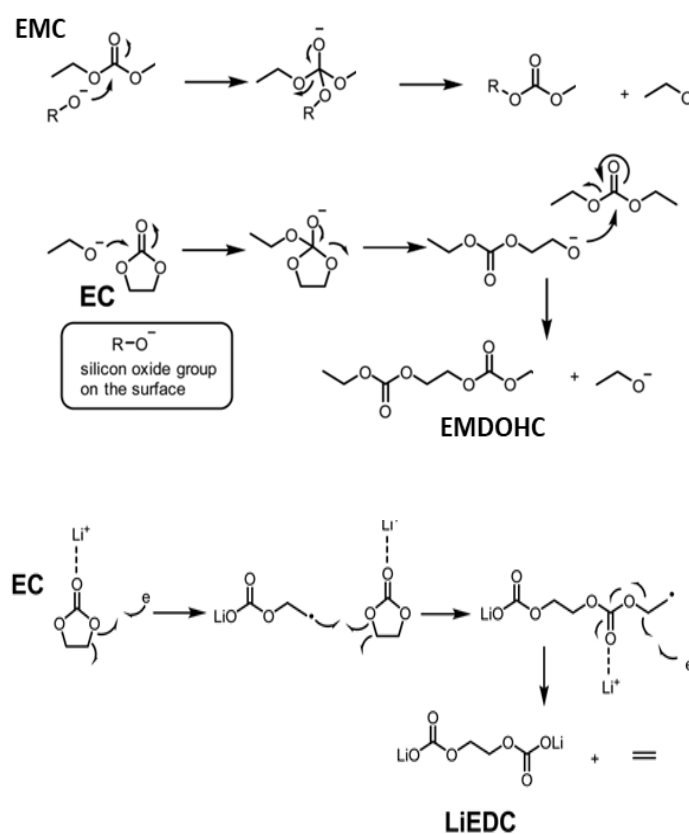
Figure 5.7. The formation mechanism of EMDOHC and LiEDC.

In addition, the volume expansion in silicon electrodes causes the physical or electrochemical isolation of active materials from the conduction pathway, dead silicon that cannot contribute to capacities. The dead silicon also traps cyclable Li ions leading to capacity fade [11,217,228].

We address the capacity loss to the formation of the SEI and dead silicon particles for the Si/Li cells with bare and PD-treated Cu current collectors in terms of percentage of Li ions loss to the capacity fade. To do this, we considered two main cases. In the first case, we assume that, there is no supply of excess Li ions from the Li metal, thus the capacity retention depends on the initial capacity of the cell after the first cycle. During the first cycle, the silicon electrode is charged from $Li_{(0.01)}Si$ to $Li_{(2.6)}Si$ ($x_{0,Si} = 0.003$, $x_{Si} = 0.78$ in Figure 5.2b

and Figure 5.3 respectively). After 40 cycles the silicon electrode is lithiated from $Li_{(0.59)}Si$

to $Li_{(2.31)}Si$ ($x_{0,Si} = 0.18$, $x_{Si} = 0.69$ in Figure 5.2b and Figure 5.3, respectively). The fraction

of the total Li ions loss after the 40th cycle is

$(2.6-(2.31-(0.59-0.01)))/(2.6-0.01)=0.34$ for the cells with bare Cu current

collector. The capacity loss of the cell in terms of Li ions trapped in the isolated silicon is

$(0.59-0.01)/(2.6-0.01)=0.22$. The remaining fraction of Li ions loss is to the formation

of the SEI. Similar calculations were done for the cells with the PD-treated Cu current

collector and the results are displayed in Figure 5.8a and 5.7b. The rate of SEI formation on

just produced lithium ion cells are very high and it is known to control the capacity fade

during pre-cycling [229]. However, we conducted the capacity-fading analysis after the pre-

cycling stage. Hence, from Figure 5.8a, the capacity fading due to the loss of Li ions in cells

with the bare Cu current collector is controlled by the Li ions trapped in the isolated silicon

during cycling but becomes almost the same at the end of the 500 cycles. In Figure 5.8b, the

capacity fading due to loss of Li ions in the cells with PD-treated Cu current collector is

dominated by the Li ions trapped in isolated silicon during the initial stages of cycling, but

it was overtaken by the Li ions loss to the SEI formation after 150 cycles. The loss of Li ions

to SEI formation was similar for the two cell configurations as shown in Figure 5.8. The

only difference was in the loss of Li ions to the isolation of the silicon active material and

was higher in the cells with bare Cu current collector. Thus, the presence of the PD interlayer

between the silicon composite electrode and Cu current collector aids in the reduction in the

formation of dead silicon and hence improves the capacity of the cell.
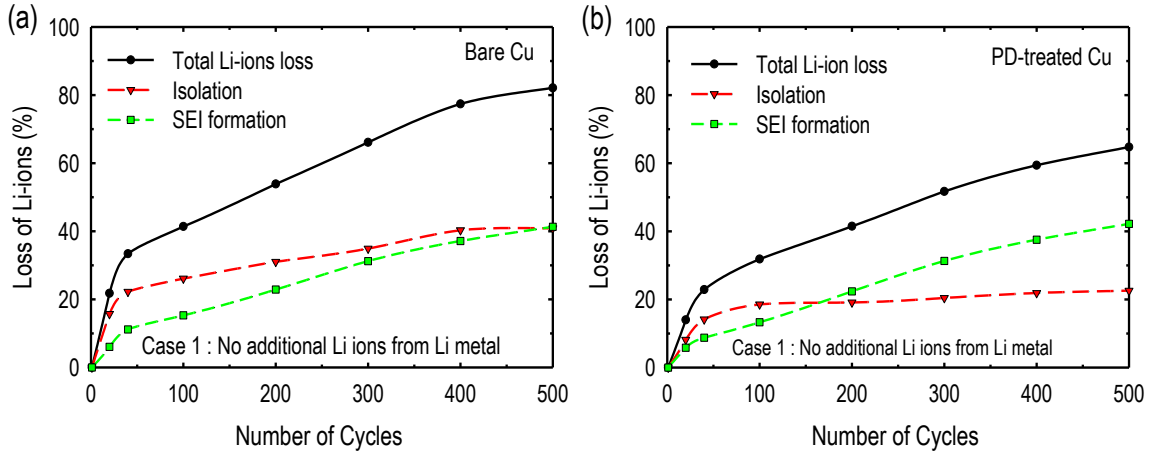
Figure 5.8. The percentage of Li ion loss in Si/Li cells with (a) bare Cu current collector and (b) PD-treated Cu current collector, estimated based on the assumption that, no additional Li ions are supplied from the Li metal.

In the second case, we considered the effect of the additional Li ions from the Li metal and presented the results of the net loss of Li ions as function of number of cycles for the bare and PD-treated Cu current collectors in Figure 5.9a and 5.9b, respectively. From the model parameters that change with cycling in Figure 5.2, the maximum Li ion concentration ($c_{\max,Si}$) was found to increase with cycling (Figure 5.2c). The increase in $c_{\max,Si}$ is due to the additional supply of Li ions from the Li metal after the first cycle. Similar to the estimation of Li ion loss in the first case, the silicon electrode was charged from $Li_{(0.01)}Si$ to $Li_{(2.6)}Si$. However, during the 40th cycle, the silicon electrode was charged from $Li_{(0.59)}Si$ to $Li_{(3.05)}Si$ ($x_{0,Si} = 0.003$, $x_{Si} = 0.92$ ($x_{Si} = x_{Si}^0 \times \left(c_{\max\_i}/c_{\max\_0}\right)$,where x_{Si}^0 is the SOC at EOC during the first cycle). There was a 0.74 increase in the stoichiometric content of Li ions in the charged state relative to when the effect of Li metal was not considered. Thus, the fraction of total Li ions loss after the 40th cycle is reduced from 0.34 to 0.17. This excess Li ion is assumed to replenish the Li ion loss to the SEI formation. This assumption was made

based on the fact that, the amount of Li ions trapped in the film formation cannot account for the cumulative capacity retention of the cells due to the unlimited supply of Li ions from the Li metal as demonstrated experimentally by Delpuech et al. [225] by using quantitative Li NMR [230] spectroscopy. On the other hand, the Li ions trapped in the isolated silicon particles contributes to the cumulative capacity retention due to the reduction in the holding capacity of the silicon electrode. The net loss of Li ions to SEI formation in the cells with the bare Cu current collector is ca 0 % at the 500 cycle (Figure 5.9a) while that in the cells with the PD-treated is ca. 4 % (Figure 5.9b). This is because the amount of the silicon particles in the cells with PD-treated Cu current collector after the 500 cycles is quite higher and most of them are exposed to the electrolyte after lithiation leading to high LiEDC formation. Thus, the excess Li ions supplied from the Li metal were not enough to replenish those losses to the SEI formation.
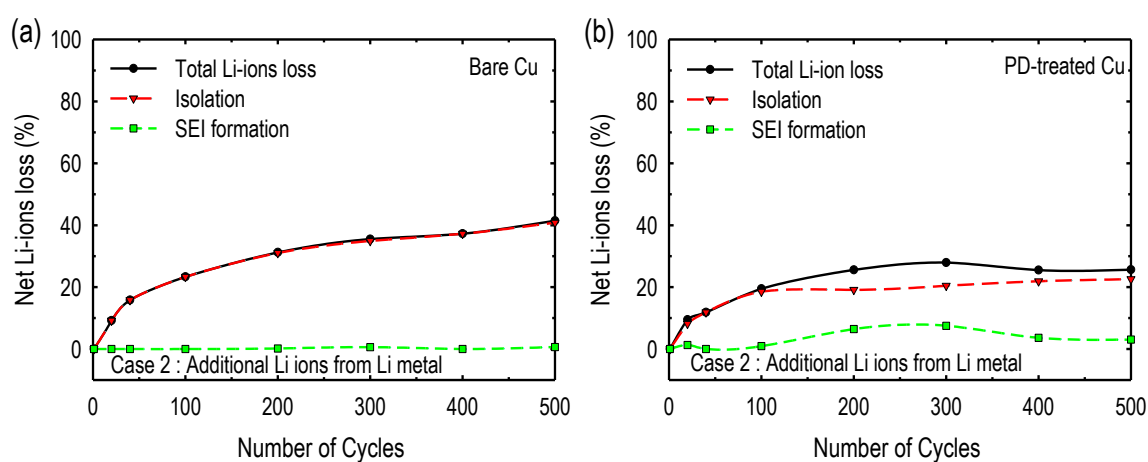
Figure 5.9. The net loss of Li ions in Si/Li cells with (a) bare Cu current collector and (b) PD-treated Cu current collector, estimated considering the effect of the excess Li ions from the Li metal.

Figure 5.10 shows the percentage contribution of the film resistance (SEI resistance and contact resistance), Li ion loss to SEI formation and Li ions trapped in the isolated silicon

particles towards the reduction of the capacity retention of the cells with the bare and PD-treated Cu current collector corresponding to the result in Figure 5.1. The calculations of the percentage contribution of the Li ion losses were done based on the assumption used in the second case in Figure 5.9. The film resistance contributed to ca. 41.4 and 19.51 % in the capacity reduction in the cells with bare and PD-treated Cu current collectors, respectively. Thus, the presence of the PD-interlayer reduces the effect of the film resistance (contact resistance) by ca. 22 % at the end of 500 cycles. This reduction in the contact resistance can be attributed to the increase in adhesion strength [218] owing to the ability of the polydopamine interlayer to form covalent bonds [231] with polyacrylic acid binder in the silicon composite. The loss of the capacity to isolation of the silicon active material contributed to 16.7 and 6.6 % in the bare and PD-treated Cu current collectors, respectively. Thus, the polydopamine interlayer also reduces the capacity loss to the isolation of the silicon particles by ca. 10 %. Owing to the strong adhesion between the silicon composite electrode and the Cu current collector by the PD interlayer, the silicon particles at the surface of the electrode prone to isolation experiences a higher force of attraction as compared to those in the cells with the bare Cu current collector. A schematic representation of this phenomenon is presented in Figure 5.11. Since the amount of Li ion loss to the formation of the SEI cannot account for the capacity retention due to the unlimited supply of Li ions from the Li metal, its percentage contribution was almost negligible with a value less than 1 % in the two cell configurations. The reduction in the reaction rate constant in Figure 5.2d can be attributed to the continuous passivation of the surface of the electrode by an insulating film during cycling [232]. The reduction in the electrochemical rate constant result in a slow charge transfer process at the electrode/electrolyte interface (reduction in the j_p in the P2D model). This results in an increase in the charge transfer resistance, which contributes to a ca. 15 % reduction in the capacity retention.
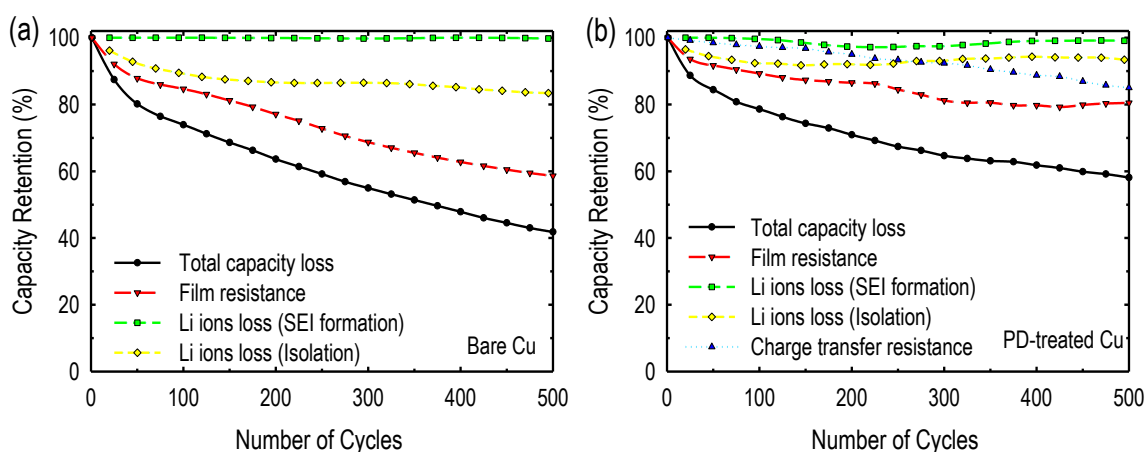
Figure 5.10. Relative contribution of the film resistance (SEI resistance and contact resistance), Li ions loss to SEI formation and Li ions trapped in the isolated silicon active material to the total capacity fade corresponding to the results in Figure 1 in Si/Li half-cells with (a) bare Cu current collector and (b) PD-treated Cu current collector.
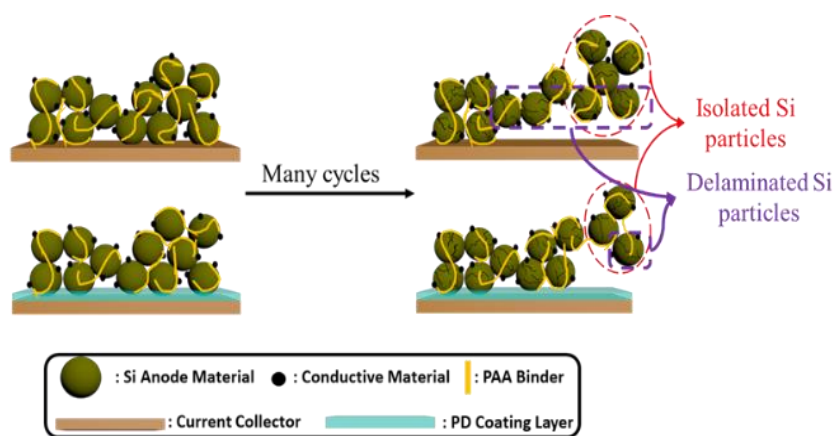
Figure 5.11. Schematic diagram showing the effect of the polydopamine interlayer on the number of isolated particles after several cycles. Less number of Si particles are isolated due to the stronger attraction force exerted on the Si particles at the surface of the electrode by those in contact with the Cu current collector.

5.4 Conclusion

The effect of PD thin film interlayer between silicon composite electrode and Cu current collector on the cycle performance of Si-based anode was analyzed by fitting the predictions of a physics-based model to experimental discharge curves obtained from cycling Si/Li cells with bare and PD-treated Cu current collectors. By examining the model parameters that change with cycling, the various capacity-fading mechanisms in the Si/Li cells with bare and PD-treated Cu current collector were established and discussed. Based on our analysis, the major capacity-fading mechanisms in Si/Li cells are the increase in the film resistance (SEI resistance and contact resistance) and the isolation of silicon active materials. The presence of the PD thin film interlayer resulted in the reduction in the capacity loss to the film resistance (contact resistance) and the Li ions trapped in the isolated silicon active material by ca. 22 and 10 %, respectively. The Li ion loss to the formation of the SEI did not have any profound effect on the capacity retention owing to the unlimited supply of Li ions from the Li metal in the cell. The insulating-nature of the PD thin film interlayer lead to a reduction in the reaction rate constant resulting in an increase in the charge transfer resistance. This contributed to ca. 15 % reduction in the capacity retention. Thus, for a further improvement in the cycle performance of the silicon-based anode, a more conductive interlayer between the silicon composite material and the copper current collector should be employed.

Chapter 6

A chemo-mechanical degradation model

6.1 Introduction

As observed from the capacity fade analysis in Chapter 5, the main capacity-fading mechanisms of anode materials with high volume expansion such as silicon are the loss of Li ions to SEI (EMDOHC and LiEDC) formation, film resistance (contact resistance and SEI resistance) and Li ions loss to particle isolation. Coating of the surface of the current collector with a thin adhesive material improved the electrochemical performance by reducing the capacity loss to contact resistance and Li ions loss to particle isolation but also lead to a loss of capacity to charge transfer resistance owing to the insulating nature of the PD thin film. Thus, the capacity fading of the cells with both bare and PD-treated Cu current collector are caused by chemical and mechanical degradation mechanisms. Hence, to adequately describe and quantify the contributions of each mechanism to the capacity fade, a capacity fade model that couples chemical and mechanical degradation must be developed.

Deshpande et al. [14] proposed a mathematical model to describe the Li ion loss caused by coupled chemical and mechanical degradation for graphite-LiFePO$_4$ cells at different temperatures. Xie et al. [233] developed an integrated LIB stress model for commercial LixC$_6$ anode by considering both battery multi-transport process and cycling induced chemical degradation. Li et al. [234] modified a capacity degradation model with chemical/mechanical degradation and integrated it with an advanced single particle model to predict battery capacity loss as a function of number of cycle and temperature, and SEI layer formation and

growth coupled with mechanical fatigue. Almost all the chemo-mechanical models for cycle life prediction reported are for graphite-based electrodes. On the part Si-based electrodes, mechanical degradation due to diffusion-induced stress because of the volume expansion has been modeled to investigate the Li diffusivity in amorphous Si (a-Si) [235], chemo-mechanical coupling in (de) lithiation of amorphous Si via simulation of Si thin films and nanospheres [236], and the lithiation kinetics in Si [237]. However, there have been no reports on the development of a model to describe and predict the long-term cycle life of Si-based anodes. Wang et al. [238], used a multiphysics microstructure-resolved model (MRM) incorporated with Si anodes to investigate various cell design parameters on the electrochemical performance of amorphous Si-anode-based LIBs but did not consider the degradation mechanisms.

In this Chapter, our objective is to develop and validate a chemo-mechanical degradation model to describe the capacity-fading mechanisms of Si-based LIBs with different adhesion strength between the composite electrode and the copper current collector. The developed model is based on the degradation mechanisms identified in Chapter 5. The developed model is validated with experimental data from coin cells consisting of Si and bare and PD-treated Cu current collector with Li metal as the reference electrode. The P2D model is used as the basis for this model and the model will be solved in COMSOL Multiphysics module.

6.2 Model development

The main capacity-fading mechanisms considered in this study are the contact resistance between the Si composite electrode and the copper current collector due to volume expansion, the formation and dissolution of SEI in the Si electrode, physical isolation of Si active material and the reduction in the rate of charge transfer in the cell with PD-treated

copper current collector. Figure 6.1 shows the degradation mechanisms of Si electrode with PD-treated copper current collector. The effect of the excess Li ions supplied by the Li metal during cycling is also considered in this model. The various mechanisms have been thoroughly discussed in previous work [13,217,218,227,239].
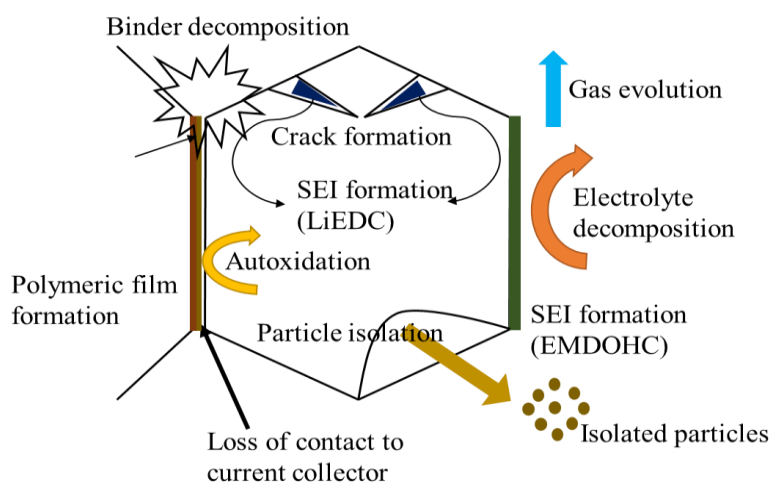
Figure 6.1. Degradation mechanisms of Si electrode with PD-interlayer between the Cu current collector and the composite electrode.

6.2.1 Modeling of SEI formation

From Chapter 5, two types of SEI are formed during the (de) lithiation processes of Si electrodes. First is the formation of ethyl methyl 2, 5-dioxahexane dicarboxylate (EMDOHC) [219] during the initial stages of cycling when a mixture of ethylene carbonate/ethyl methyl carbonate (EC:EMC) related solvents are used. Second is lithium ethylene dicarbonate (LiEDC) [219,227] which is formed when the lithiated Si is exposed to the electrolyte due to crack formation because of volume expansion.

6.2.1.1 Modeling of EMDOHC formation

The electrolyte species involved in the formation of the SEI is a 1.15 M LiPF$_6$/EC:EMC (3:7 v/v) thus we assumed that the SEI product formed is EMDOHC and that the growth of the EMDOHC layer is one-dimensional. We also assume that the solvent species produced during the dissolution reaction at the film/electrolyte interphase diffuses back to the electrode/film interphase where it reacts with Li ions to form EMDOHC. The formation and dissolution of the EMDOHC because continuous expansion and contraction of the Si electrode [240] is assumed to be

$$S + \text{Li}^+ + e^- \underset{k_{S,2}}{\overset{k_{S,1}}{\rightleftharpoons}} S_p + P \qquad\qquad [6.1]$$

where S_p and P are the EMDOHC product and lithium propionate (CH$_3$CH$_2$CO$_2$Li) by-product formed due to the solvent reduction reaction at the surface of the Si electrode.

Assuming the rate of SEI formation and dissolution is a first-order reaction to the concentration of the reacting solvent species, the rate of solvent decomposition can express as

$$-R_{S,1} = k_{S,1} C_S - k'_{S,2} C_{S_p} C_p \qquad\qquad [6.2]$$

where $k_{S,1}$ and $k_{S,2}$ are the rate constants for the formation and dissolution of the SEI respectively, and C_S, C_{Sp} and C_p are the concentrations of the solvent species at the Si electrode, the EMDOHC products and the lithium propionate respectively.

We assume that the electrode/film interphase is the moving boundary and the film/electrolyte interphase is stationary. The corresponding total material balance of the solvent species is given as

$$\frac{\partial C_S}{\partial t} - D_S \frac{\partial^2 C_S}{\partial x^2} = k'_{S,2} C_{S_p} C_p - k_{S,1} C_S \qquad [6.3]$$

where D_S is the diffusion coefficient constant for Li through the SEI. The concentration of the propionate is assumed constant, hence $k'_{S,2} C_p = k_{S,2}$. At any point in time t,

$$C_S + C_{S_P} = \text{constant} = C_0 \qquad [6.4]$$

Hence, equation 6.3 can be expressed as

$$\frac{\partial C_S}{\partial t} - D_S \frac{\partial^2 C_S}{\partial x^2} = k_{S,2} C_0 - \left(k_{S,1} + k_{S,2} \right) C_S \qquad [6.5]$$

The boundary conditions for Eq. 6.5 at the electrolyte/film and film/electrode interphase are given by

$$C_S = C_0 \text{ at } x = 0, \qquad [6.6]$$

$$C_S = C_0 e^{-(k_{S,1}+k_{S,2})t} - \frac{k_{S,2} C_0}{k_{S,1} + k_{S,2}} e^{-(k_{S,1}+k_{S,2})t} + \frac{k_{S,2} C_0}{k_{S,1} + k_{S,2}} \text{ at } x = L(t) \qquad [6.7]$$

From Eq. 6.2, the reaction between the solvent species and the Li ions is an equimolar reaction. Thus, the fractional capacity loss due to the reduction in solvent concentration at the electrode SEI interphase is equal to the fractional loss of Li ions consumed by the by-product (CH₃CH₂CO₂Li) during the formation of SEI (EMDOHC) and is expressed as

$$x_{\text{EMDOHC}} = \frac{C_0 - C_S}{C_0} \qquad [6.8]$$

and the active Li ions loss due to the formation of EMDOHC can be expressed as

$$C_{\text{EMDOHC}} = x_{\text{EMDOHC}} C_{mean,0} \qquad [6.9]$$

where $C_{mean,0}$ is the initial mean concentration of Li ions at the beginning of cycling

The resistance, R_{SEI}, due to the continuous formation of EMDOHC can be estimated using an expression of the SEI thickness proposed by Sankarasubramanian and Krishnamurthy [196] and is given by

$$R_{SEI}(t) = \frac{x_{EMDOHC}(N)n_0}{Z_p C_p A_i \kappa_{SEI}}$$
[6.10]

where n_0, Z_p, C_p, A_i and κ_{SEI} are initial number of moles of Li ions in the electrolyte, the stoichiometric coefficient of Li in the solvent decomposition reaction, the concentration of Li ions in the solvent decomposition reaction, the area of the Si electrode and the conductivity of the SEI, respectively.

6.2.1.2 Modeling of LiEDC formation

To calculate the fractional Li ions loss due to the formation of LiEDC, the area of the cracks generated in the electrode after discharge was first evaluated. Using Paris Law formulation to describe a surface crack of length a, growing with each charge/discharge cycle N,

$$\frac{da_{cr}}{dN} = k_{cr}\left[\sigma_{\theta,\max} b\sqrt{\pi a_{cr}}\right]^{m_{cr}}$$
[6.11]

where k_{cr} m_{cr} and b are constants. The maximum tangential stress, $\sigma_{\theta,\max}$ at the surface of the electrode can be expressed as [14]

$$\sigma_{\theta,\max} = -\frac{1}{45}\frac{E\Omega}{(1-\upsilon)}\left(\frac{R^2}{FD_s}\right)\frac{I_{cell}}{\varepsilon_s(AL)_{PE}}$$
[6.12]

where E is Young's modulus, υ is Poisson's ratio, Ω is partial molar volume, R is the radius of the Si particles, I_{cell} is current density, ε_s is the volume fraction of the Si active material, A is the geometric area and L is the thickness of the Si thin film. Integrating Eq. 6.20 yields

$$\tilde{a} = \frac{a_{cr}}{a_{cr,0}} = \left(1 + \frac{2-m_{cr}}{2} k_{cr} \left[\sigma_{\theta,\max} b \sqrt{\pi} \right]^{m_{cr}} a_{cr,0}^{\left(\frac{m_{cr}-2}{2}\right)} N \right)^{\frac{2}{2-m_{cr}}} \qquad [6.13]$$

The number and length of cracks are assumed to be the same throughout the particle and grow in depth into the particle during each charge half cycle. The initial number of cracks over the particle surface assuming the density of cracks, ρ_{cr} is constant can be expressed as

$$N_{cr} = 4\pi R^2 \rho_{cr} \qquad [6.14]$$

The newly exposed surface area as the crack grows is given as $2l_{cr}\left(da_{cr}\right)$ where l_{cr} is the length of the crack. Hence, the total area related to the growth of cracks is given by $A_{cr} = 8\pi R^2 \rho_{cr} a_{cr} l_{cr}$ and the changes in the total area after each charge cycle can be expressed as

$$\frac{dA_{cr}}{dN} = \frac{dA_{cr}}{da} \frac{da_{cr}}{dN} = 8\pi R^2 l_{cr} \rho_{cr} k_{cr} \left[\sigma_{\theta,\max} b \sqrt{\pi a_{cr,0}} \right]^{m_{cr}} \tilde{a}^{m/2} \qquad [6.15]$$

The newly exposed lithiated surface of the Si particle is assumed to be covered by SEI (LiEDC) of thickness L^0_{LiEDC}. Hence, the total capacity loss due to the formation of LiEDC can be expressed as

$$\frac{dQ_{LiEDC}}{dN} = \frac{n_{LiEDC} L^0_{LiEDC} \rho_{LiEDC} F}{M_{LiEDC}} \left(8\pi R^2 l_{cr} \rho_{cr} k_{cr} \left[\sigma_{\theta,\max} b \sqrt{\pi a_{cr,0}} \right]^{m_{cr}} \tilde{a}^{m/2} \right) \qquad [6.16]$$

and the fractional capacity loss in terms of Li ions loss due to the formation of LiEDC is given as

$$x_{LiEDC} = \frac{Q_{LiEDC}}{Q_0} \qquad [6.17]$$

where n_{LiEDC} is the number of Li atoms lost per LiEDC molecule formed, ρ_{LiEDC} is the density of LiEDC, M_{LiEDC} is the molecular weight of LiEDC and Q_0 is the initial capacity of the cell. The active Li ions loss due to the formation of LiEDC is expressed as

$$C_{LiEDC} = x_{LiEDC} C_{mean,0} \qquad [6.18]$$

6.2.2 Modeling of contact resistance

The contact resistance between the Si composite electrode and the copper current collector was modeled using the idea of flux tubes, which was originally used in thermal and electrical contacts [241−243]. The resistivity R_i of a single spot on the current collector is given by [244]

$$R_i = \frac{1.05}{4K_{mean}a_i} \qquad [6.19]$$

where the mean electrical conductivity of the K_{mean} is the individual conductivities of the silicon composited electrode K_1 and the copper current collector K_2 and a_i is the radius of the contact spot of the flux tube. Using parallel connection of resistivities, the total contact resistance R_c, can expressed as

$$\frac{1}{R_c} = \sum_{i=1}^{N_{sp}} \frac{1}{R_i} = \frac{4K_{mean}}{1.05} \sum_{i=1}^{N_{sp}} a_i \qquad [6.20]$$

where N_{sp} is the complete number of spots.

Since there is no external force exerted on the cell after assembly, the total number of the contact spots is mainly due to the adhesion strength of the binding material between the silicon composite electrode and the copper current collector. Hence, the total number of contact spots depends on the coefficient of adhesion $\beta_a = F_1/F_{crit}$ and can be expressed as:

$$\sum_{i=1}^{N_{sp}} \pi a_i^2 = A_a \left(1 - \beta_a\right) \qquad [6.21]$$

where A_a is the apparent contact area, and by inserting Eq. 6.31 into Eq. 6.30 we obtain

$$\frac{1}{R_c} = \frac{4K_{mean}}{1.05} \left(\frac{A_a \left(1 - \beta_a\right)}{\pi}\right)^{1/2} \qquad [6.22]$$

The apparent contact area, A_a reduces as cycling proceeds owing the loss of contact between the Si composite electrode and the copper current collector [218] and it is expressed as

$$A_a = A_{a,0} - A_{a,loss} \qquad [6.23]$$

The contact radius between the Si particles and the copper current collector was evaluated using a mathematical model that accounts for the attractive forces inside and outside the actual contact area to calculate the elastic deformation of a sphere on a flat surface [245]. The model was adopted based on the following assumptions:

1. The deformations are purely elastic and are governed by Hooke's law.

2. The materials in contact are elastically isotropic.

3. The Young's modulus E and the Poisson's υ ratio remains constant under load.

4. The contact radius ac is relatively smaller compared to the radius of the silicon particles

5. The atomic structure of the silicon particles is not considered

The contact radius can be expressed as

$$a_c = a_{c,0} \left(\left(\frac{1}{2} \right) \left(1 + \left(1 - \frac{F_1}{F_{crit}} \right)^{1/2} \right) \right)^{2/3} \qquad [6.24]$$

where $F_{crit}^{JKR} = -1.5\pi R \gamma_c$ based on Johnson, Kendall, and Roberts (JKR model) [246] limit for force attraction inside contacts, γ_c is the adhesion force determined experimentally using surface and interfacial cutting analysis system (SAICAS) and peel test [247,248], and $a_{c,0}$ is the contact radius under zero external load which is expressed as

$$a_{c,0} = \left(\frac{R}{K} \right)^{1/3} \left[2\sqrt{-F_c} \right]^{2/3} \qquad [6.25]$$

where R is the radius and K is a function of the Young modulus E_1, E_2 and Poison's ratio v_1, v_2 of the two materials in contact and is expressed as

$$K = \frac{4}{3} \left[\frac{\left(1 - v_1^2 \right)}{E_1} + \frac{\left(1 - v_2^2 \right)}{E_2} \right]^{-1} \qquad [6.26]$$

The applied force, F_1 by the maximum tangential stress, $\sigma_{\theta,max}$ generated during Li ion insertion owing to the volume expansion of Si has been reported to be tensile at the center and compressive at the surface with the same magnitude [249] and can be expressed as

$$F_1 = -\frac{\pi}{45} \frac{E\Omega}{(1-v)} \left(\frac{R^4}{FD_{s,p}} \right) \frac{I_{cell}}{\varepsilon_s \left(AL_{Si} \right)_{PE}} \qquad [6.27]$$

We assumed that, the reduction in the contact radius, a_c between the Si particles and the copper current collector takes the form of a crack propagation. Thus, we adopted an expression in the form of the Paris' law formulation to represent a loss of contact of length, $a_{c,loss}$ increasing with each charge/discharge cycle N

$$\frac{da_{c,loss}}{dN} = k_c \Delta a_c{}^{m_c}$$ [6.28]

where k_c and m_c are constants and the changes in the contact area can be expressed as

$$\frac{da_{c,loss}}{dN} = k_c a_{c,0} \left[1 - \left(\left(\frac{1}{2} \right) \left(1 + \left(1 - \frac{F_1}{F_{crit}} \right)^{1/2} \right) \right)^{2/3} \right]^{m_c}$$ [6.29]

The contact density, ρ_c is define as the number of contacts per unit area of the electrode. The contact density is assumed a constant and the initial number of contacts in the electrode is given as

$$N_c = \pi R^2 \rho_c$$ [6.30]

where R is the radius of the silicon composite electrode. The area of the newly detached surfaces during the charge/discharge process is expressed as $2\pi l_{c,loss} \left(da_{c,loss} \right)$, where $l_{c,loss}$ is the length of loss in contact. Hence, the total surface area associated with the loss of contact is given as

$$A_{a,loss} = 2\pi^2 R^2 \rho_c a_{c,loss} l_{c,loss}$$ [6.31]

Thus, the loss in the apparent contact surface area as a function of the number of cycles can then be expressed as:

$$\frac{dA_{a,loss}}{dN} = \frac{dA_{a,loss}}{da_{c,loss}}\frac{da_{c,loss}}{dN} = 2\pi^2 R^2 \rho_c k_c l_{c,loss} a_{c,0} \left[1 - \left(\left(\frac{1}{2}\right)\left(1 + \left(1 - \frac{F_1}{F_{crit}}\right)^{1/2}\right)\right)^{2/3}\right]^{m_c} \quad [6.32]$$

6.2.3 Modeling of particle isolation

Li ions are trapped in physically isolated Si composite electrode during (de) lithiation process. The effects of the physical isolation are considered under one variable, apparent porosity and it is given as

$$\theta_{app} = \frac{V_{iso}}{V_{total}} = \frac{A_{iso}}{A_i} \quad [6.33]$$

where A_i and A_{iso} are the initial surface area and the unavailable surface area due to isolation.

To evaluate A_{iso}, we adopted and modified a previously phenomenological developed model [156] to include the effect of the adhesion force between the Si particles in the form of the coefficient of adhesion [250], $\beta_a = F_1/F_{crit}$ and is given as

$$A_{iso} = A_i \left[(1-\beta_a)(1-e^{-k_{iso}N})\right] + A_i k_{frac} N \quad [6.34]$$

where k_{iso} and k_{frac} are dimensionless evolution parameter for isolation and fracture, respectively.

The concentration of Li ions loss to the physical isolation of Si particles can be expressed as

$$C_{iso} = \theta_{app} C_{mean,0} \quad [6.35]$$

Owing to the increase in the apparent porosity, θ_{app} with cycling, the effective electronic conductivity is expected to decrease according the expression

$$K_{eff}^{iso} = K_1 \left[1 - \left(\varepsilon_s + \theta_{app} \right) \right]^{Brugg}$$ [6.36]

where the Bruggeman's constant, *Brugg* is 1.5.

6.2.4 Modeling of Li ions inventory

The Li ions available after SEI formation and Si particle isolation is given by

$$C_{mean} = C_{mean,0} \left(1 - \left(x_{SEI} + \theta_{app} \right) \right)$$ [6.37]

However, due to the abundant Li ions supplied by Li metal, the mean Li ions concentration increases with cycling. The excess Li ions is accounted for by modifying Eq. 6.37 to include a step input in Li ion concentration, $C_{mean}(N)$. The Si electrode is modeled as a plug flow reactor with a recycling ratio, R_{cycle} as shown in the block diagram in scheme 6.2.
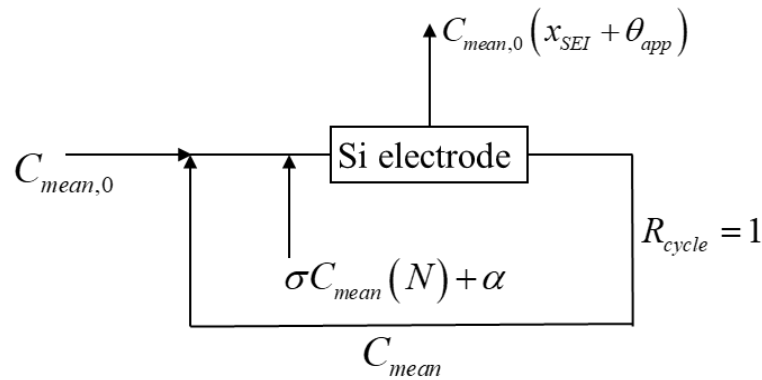
Figure 6.2 Block diagram of Li ions inventory in the Si electrode

The steady-state output of the system shown in scheme 1 is given by:

$$C_{mean} = \frac{C_{mean,0}\left(1-\left(x_{SEI}+\theta_{app}\right)\right)}{1+R_{cycle}\left(x_{SEI}+\theta_{app}\right)} \qquad [6.38]$$

Considering a step input to the system defined according to the following conditions:

$$\text{at } N<0, C_{mean}=C_{mean,0} \text{ and } N>0, C_{mean}=C_{mean}\left(N\right) \qquad [6.39]$$

where the expression for the step input concentration, $C_{mean}\left(N\right)$ is determined by fitting the

excess concentration of Li ions from our previous report [219] and is given by

$$C_{mean}\left(N\right)=C_{mean,0}\left(1-e^{-k_{Li,1}N}\right)+k_{Li,2}N^{\alpha_{Li}} \qquad [6.40]$$

where $k_{Li,1}$, $k_{Li,2}$ and α_{Li} are the fitting parameters.

The effect of this step is a step in the outlet concentration of Li ions during charging at

$N=1$. This result in a step to the inlet concentration during charging at $N=1$. The considered

input step becomes manifest in the outlet Li ions concentration during charging at $N\geq2$.

The solution of a material balance of Li ions entering the Si electrode at any time can be

expressed as

$$C_{mean,in}=\sigma C_{mean}+\alpha \qquad [6.41]$$

Where $\sigma=\dfrac{R_{cycle}}{R_{cycle}+1}$ and $\alpha=\dfrac{C_{mean}}{R_{cycle}+1}$. Assuming the excess Li ions from the Li metal after

the cycle is not consumed during the subsequent cycles, the concentration of the cyclable Li

ions can be expressed as

$$C_{mean}=\frac{R_{cycle}}{\left(1+R_{cycle}\right)}\frac{C_{mean,0}\left(1-\left(x_{SEI}+\theta_{app}\right)\right)}{1+R_{cycle}\left(x_{SEI}+\theta_{app}\right)}+\frac{C_{mean,0}\left(1-e^{-k_{Li,1}N}\right)+k_{Li,2}N^{\alpha_{Li}}}{1+R_{cycle}} \qquad [6.42]$$

6.2.5 Modeling the effect of the PD interlayer

The PD film may inhibit charge transfer at the surface of the electrode by completely blocking the surface of the copper current collector so that charge transfer occurs at the surface of the uncovered fraction, $(1-\theta)$. These effects are treated by assuming that the rate constant for an electron transfer, k_p, is a linear function of the coverage, θ,[251],

$$k_p = k_{\theta=0}^0 (1-\theta) + k_p^0 \theta \qquad [6.43]$$

where $k_{\theta=0}^0$ is the rate constant for electron transfer at the bare copper current collector and k_p^0 that for electron transfer through the PD film. The PD film also serves as tunneling barrier causing exponential decrease in the electron-transfer rate with increasing thickness of the film as

$$k_p = k_{\theta=0}^0 (1-\theta) + k_p^0 e^{-\beta d} \theta \qquad [6.44]$$

Where β is the tunneling barrier coefficient and d is the thickness of the PD film. The surface of the electrode is passivated by a polymeric insulating film as cycling proceeds [232]. This result in an increase in the coverage of the insulating PD film and can be expressed as

$$(1-\theta) = (1-\theta_0) e^{-k_\theta N} \qquad [6.45]$$

where k_θ is the rate constant at which the coverage increases and θ_0 is the initial coverage by the PD film prior to cycling. From Eq. 6.56 and 6.57 we obtain

$$k_p = k_{\theta=0}^0 (1-\theta_0) e^{-k_\theta N} + k_p^0 e^{-\beta d} \left(1 - e^{-k_\theta N}(1-\theta_0)\right) \qquad [6.46]$$

6.2.6 Coupling between lithiation kinetics and mechanical stress

The transport of Li ions within the host silicon can be described using Ficks second law described as

$$\frac{\partial c}{\partial t} + \nabla \cdot (-D\nabla c) = 0 \qquad [6.47]$$

The chemo-mechanical coupling in Si was modeled by embedding the stress effect in Li ion diffusion equation by empirically assuming the Li ion diffusion coefficient constant as a function of both Li ion concentration and the stress state [156,249] i.e. $D = D(c, \sigma)$. The effective Li ion diffusion coefficient D_s^{eff} can be expressed as

$$D_s^{eff} = D_{s,0} \exp\left(-\frac{\sigma_h \Omega}{k_B T}\right) \qquad [6.48]$$

where $D_{s,0}$ is the Li ion diffusion coefficient constant at the stress-free condition, σ_h is the hydrostatic stress which is defined as $\sigma_h = (\sigma_{11} + \sigma_{22} + \sigma_{33})/3$ (where σ_{ij} are the elements in stress tensor), Ω is the partial molar volume of Li ion that defines the volume change due to one mole of guest atom insertion into the host material, and $k_B T$ is the thermal energy.

As shown above, a diffusion-stress coupling model is used in the chemo-mechanical coupling model to describe the intercalation induced stress. The stress tensor is made up of two independent components, radial stress σ_r and tangential stress σ_t. The radial and the tangential stress can be respectively expressed as [252]:

$$\sigma_r = \frac{2\Omega E}{3(1-\nu)} \left(\frac{1}{r_0^3} \int_0^{r_0} c_{av} r^2 dr - \frac{1}{r^3} \int_0^r c_{av} r^2 dr \right) \qquad [6.49]$$

$$\sigma_t = \frac{\Omega E}{3(1-\nu)} \left(\frac{2}{r_0^3} \int_0^{r_0} c_{av} r^2 dr + \frac{1}{r^3} \int_0^r c_{av} r^2 dr - c_{av} \right) \qquad [6.50]$$

From equations 6.58 and 6.59, we can calculate the hydrostatic stress as

$$\sigma_h = \frac{\sigma_r + 2\sigma_t}{3} = \frac{2\Omega E}{9(1-\nu)}\left(\frac{3}{r_0^3}\int_0^{r_0} c_{av} r^2 \mathrm{d}r - c_{av}\right)$$ [6.51]

where $(3/r^3)\int_0^{r_0} cr^2 \mathrm{d}r$ is the average concentration $c_{av}(R)$ in the spherical volume of radius

r within the silicon particle of radius R. Under galvanostatic operation, the analytic solution

for the diffusion equation, Eq. 6.57 with the initial boundary conditions is [253]:

$$c(r,t) = c_0 + \frac{IR}{FD}\left[3\tau + \frac{1}{2}x^2 - \frac{3}{10}\sum_{n=1}^{\infty}\left(\frac{\sin(\lambda_n x)}{\lambda_n^2 \sin(\lambda_n)}\exp(-\lambda_n^2 \tau)\right)\right]$$ [6.52]

where $x = r/R$, $\tau = Dt/R^2$ and $\lambda_n\,(n=1,2,3,...)$ are the positive roots of $\tan(\lambda_n) = \lambda_n$.

The average concentrations using Eq. 6.62 can be expressed as [249]:

$$c_{av}(r,t) = c_0 + 3\left(\frac{IR}{FD}\right)\left[\tau + \frac{1}{10}(x^2-1) - \frac{2}{x^3}\sum_{n=1}^{\infty}\left(\frac{\sin(\lambda_n x) - (\lambda_n x)\cos(\lambda_n x)}{\lambda_n^4 \sin(\lambda_n)}\exp(-\lambda_n^2 \tau)\right)\right],$$

$$c_{av}(R,t) = c_0 + 3\left(\frac{IR}{FD}\right)\tau = c_0 + \frac{3It}{FR}$$ [6.53]

By substituting Eq. 6.62 into Eq. 6.61 we obtain the solution for the hydrostatic stress as

$$\sigma_h = \frac{1}{3}\frac{E\Omega}{(1-\nu)}\frac{IR}{FD}\left[\frac{1}{5}(1-x^2) + \frac{4}{x^3}\sum_{n=1}^{\infty}\left(\frac{\sin(\lambda_n x) - (\lambda_n x)\cos(\lambda_n x)}{\lambda_n^4 \sin(\lambda_n)}\exp(-\lambda_n^2 \tau)\right)\right]$$ [6.54]

For our low rate intensive intercalation studies, we are much concerned with longer times.

Also considering the fact that our charge/discharge cycles are much longer than R^2/D, the

characteristic time for solid-state diffusion of Li ions within the silicon electrode, the exponential terms in the hydrostatic stress equation move to zero and the summation can be ignored. Hence, the hydrostatic stress equation reduces to

$$\sigma_h = \frac{1}{5}\left(1-x^2\right)\left[\frac{E\Omega}{3\left(1-v\right)}\left(\frac{IR}{FD}\right)\right] = \frac{1}{5}\left(1-x^2\right)\left[\frac{E\Omega}{3\left(1-v\right)}\left(\frac{IR^2}{FD}\right)\right]\frac{I_{cell}}{\varepsilon_s\left(AL\right)_{PE}} \qquad [6.55]$$

6. 3 Pseudo-two-Dimensional (P2D) model – Incorporation

The developed capacity fade model was coupled with the P2D model developed by Doyle et al.[125,126] to predict the electrochemical performance of the Li/Si cells. The unit cell is made up of a porous silicon active material with a porosity of 73 % and a polymer separator with a porosity of 41 %. The porous parts are filled with a 1.15 M LiPF$_6$ in EC/EMC (3/7, v/v). The copper current collector is coated with a PD film of thickness 16 nm. Figure 6.3 is the schematic diagram of the Li ion cell modeled in this work.

A detailed description of the P2D model is given in section 1.4 and the governing equations are presented in Table 1.1.
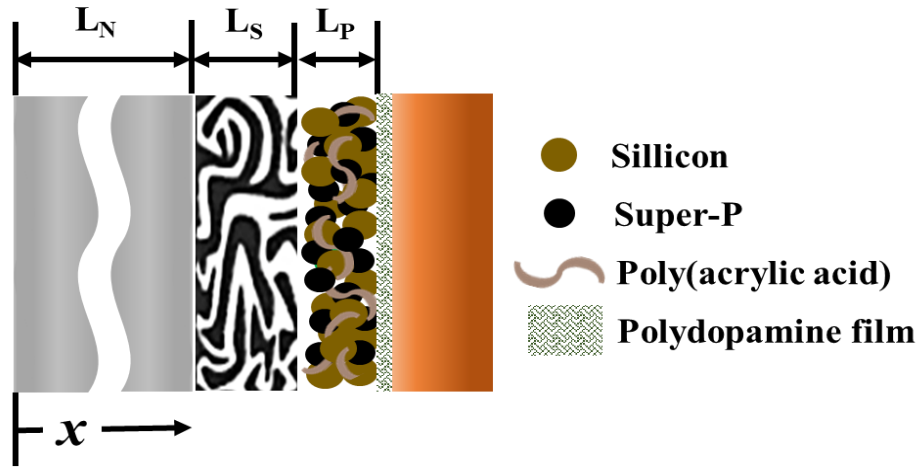
Figure 6.3. Schematic diagram of the cross section of the cell modeled in this study.

6. 4 Results and discussion

6.4.1 Model validation

To validate the developed degradation model for Si composite electrodes, the chemo-mechanical model was coupled with the P2D model to predict the charge profiles of the two cell systems with PD-treated and Bare Cu current collector. The predicted discharge profiles were fitted to the experimental data and the model best fits are presented in Figure 6.3a and 6.3c, respectively. The experimental procedures used to obtain the experimental data for the model validations are similar to those in section 5.2 of Chapter 5. A comparison between the model predicted normalized capacity for the cells with PD-treated and bare Cu current collector are presented in Figure 6.4b and 6.4d, respectively. The model best fits were obtained by using a non-linear least square method, Lavernberg-Marquardt to extract the fitting parameters in the two cell designs. The estimated standard deviations values are quite small indicating a high correlation between the model predictions and the experimental data as observed in Figure 6.4. The model parameters used for the simulations are presented in Table 6.1.

Table 6.1. Table of electrode design parameters, fitting parameters and constants used for the model prediction.

Symbol	Parameters	Value
L_p	Si electrode thickness, μm [a]	8×10^{-6}
L_n	Li metal electrode thickness, μm [a]	450×10^{-6}
L_s	Separator thickness, μm [a]	20×10^{-6}
r	Si particle radius, m [a]	30×10^{-9}
ε_e	Volume fraction electrolyte [a]	0.73
ε_s	Volume fraction of active material	0.21
$D_{s,p}$	Diffusion coefficient in Li_xSi, $m^2 \ s^{-1}$ [d]	3×10^{-16}
D	Diffusion coefficient of Li in electrolyte, $m^2 \ s^{-1}$ [c]	3.93×10^{-10}

k_n	Li-metal rate constant, $mol^{0.5}m^{-0.5}s^{-1}$ [c]	6.2×10^{-6}
K_1	Electronic conductivity Si, S m^{-1} [d]	33
$k_{p,0}$	Rate constant Si, $(m\ s^{-1})(mol\ m^3)^{-0.74}$ [d]	2×10^{-12}
$C_{mean,0}$	Theoretical maximum Li concentration, mol m^{-3} [d]	3.11×10^5
α_c	Cathodic apparent transfer coefficient [d]	0.26
α_a	Anodic apparent transfer coefficient [d]	0.74
E	Young's modulus, GPa [d]	190
ν	Poisson's ratio [d]	0.218
Ω	Partial molar volume, m^3 mol^{-1} [d]	8.9×10^{-6}
m_{cr}	Paris law constant for crack propagation [d]	2.5
ρ_c	Density of contact points m^{-2} [a]	1.67×10^{14}
k_{iso}	Isolation evolution parameter [b]	3.6×10^{-5}
A	Geometric area of Si electrode, m^2 [a]	1.131×10^{-4}
F	Faraday's constant, C [c]	96500
$k_{S,1}$	SEI formation rate constant, s^{-1} [b]	6.3×10^{-3}
$k_{S,2}$	SEI dissolution rate constant, s^{-1} [b]	4.5×10^{-4}
C_0	Initial concentration of solvent species, mol m^{-3}	1120
κ_{SEI}	Conductivity of SEI, S m^{-1} [d]	2.4×10^{-4}
k_{cr}	Paris law constant for crack propagation [b]	1.0×10^{-5}
b_{cr}	Paris law constant for crack propagation [d]	1.12
l_{cr}	Crack width, m [d]	2.0×10^{-10}
ρ_{cr}	Density of cracks, m^{-2}	2.5×10^{19}
L^0_{LiEDC}	Initial LiEDC thickness, m	2.0×10^{-10}
M_{LiEDC}	Molecular weight of LiEDC, g mol^{-1}	161.95
ρ_{SEI}	Density of SEI (LiEDC), g m^{-3} [d]	2.11×10^6
k_c	Paris law constant for loss of contact [b]	5.9×10^{15}
m_c	Paris law constant for loss of contact [d]	2.5
$l_{c,loss}$	Length of loss of contact, m	2.0×10^{-10}
k_θ	Rate constant for increase in PD coverage m s^{-1}	1.74×10^{-2}
β	Tunneling barrier coefficient m^{-1}	2.678×10^7
k_p^0	Electron transfer rate constant, PD film, m s^{-1}	2.52×10^{-13}
I_{app}	Current density, A m^{-2} [a]	5.1
θ_0	Initial PD film coverage	0.8

[a] Parameter set in cell design

[b] Fitted parameter

[c] Obtained from COMSOL library

[d] Parameters based on literature [14,238]
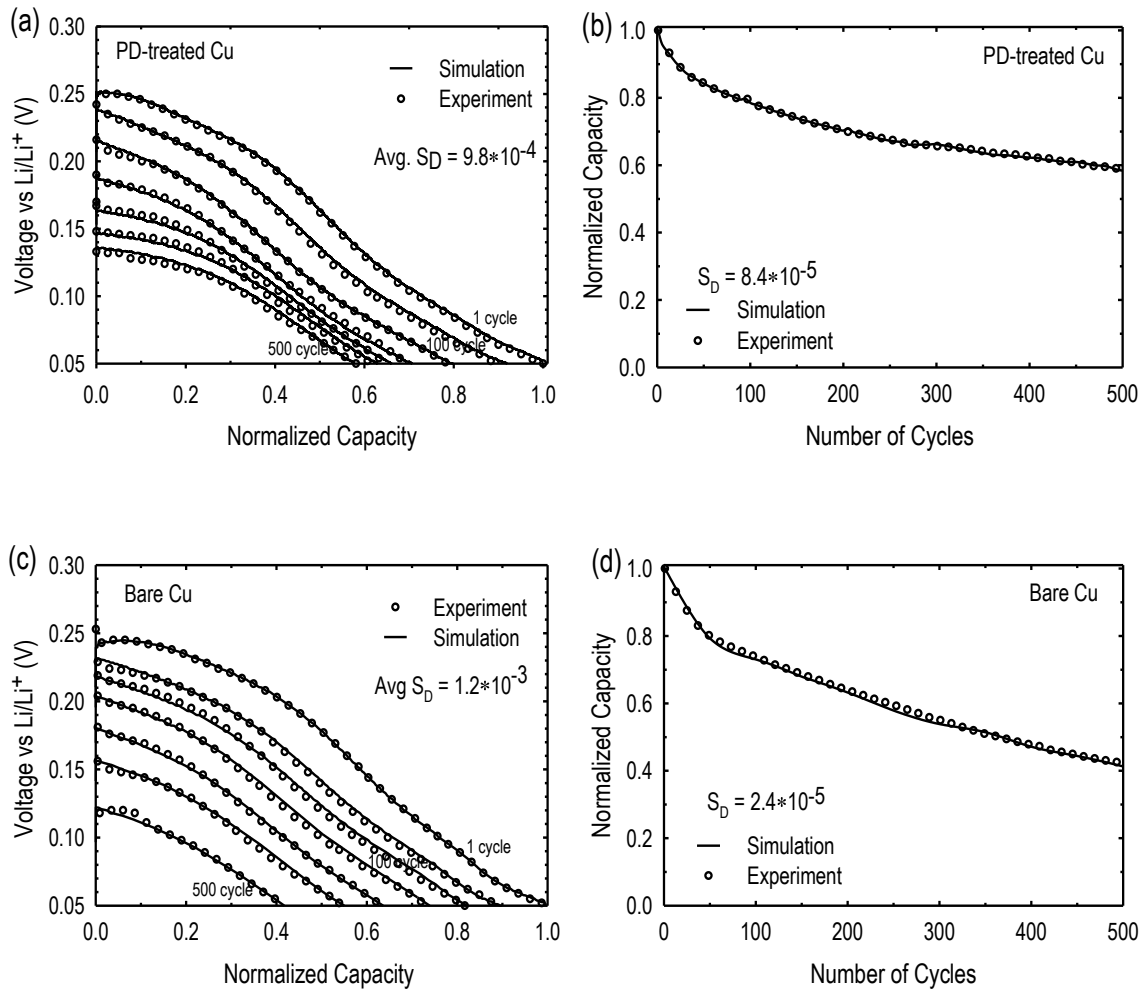
Figure 6.4. Model best fit of experimental data for charge voltage profiles at some selected number of cycles for Li/Si cells with (a) PD-treated and (b) Bare Cu current collector, and normalized capacity of (b) PD-treated and (d) Bare Cu current collector.

6.4.2 Simulation results

The correlation between the film resistance and number of cycles for the cells with PD-treated and bare Cu current collector is shown in Figure 6.5a and 6.5b respectively. The film resistance is the sum of the SEI (EMDOHC) resistance and the contact resistance between the Si composite electrode and the Cu current collector. The film resistance increased with number of cycles with the rate of increase being higher in the cells with bare Cu current

collector. The SEI (EMDOHC) resistance increased at a fast rate in the two systems at the initial stages of cycling but remained constant as cycling proceeded. For the two cell systems, the SEI (EMDOHC) resistance was almost the same at the end of the 500th cycle. Thus, the difference between the film resistances of the two systems is the contact resistance, which increases linearly with cycling. This is in line with the experimental results reported by Cho et al.[218]. The changes in contact resistance is due to the difference in the adhesion strength (γ) of the two systems resulting in a difference in the loss in the apparent contact surface area as shown in Figure 6.5c.
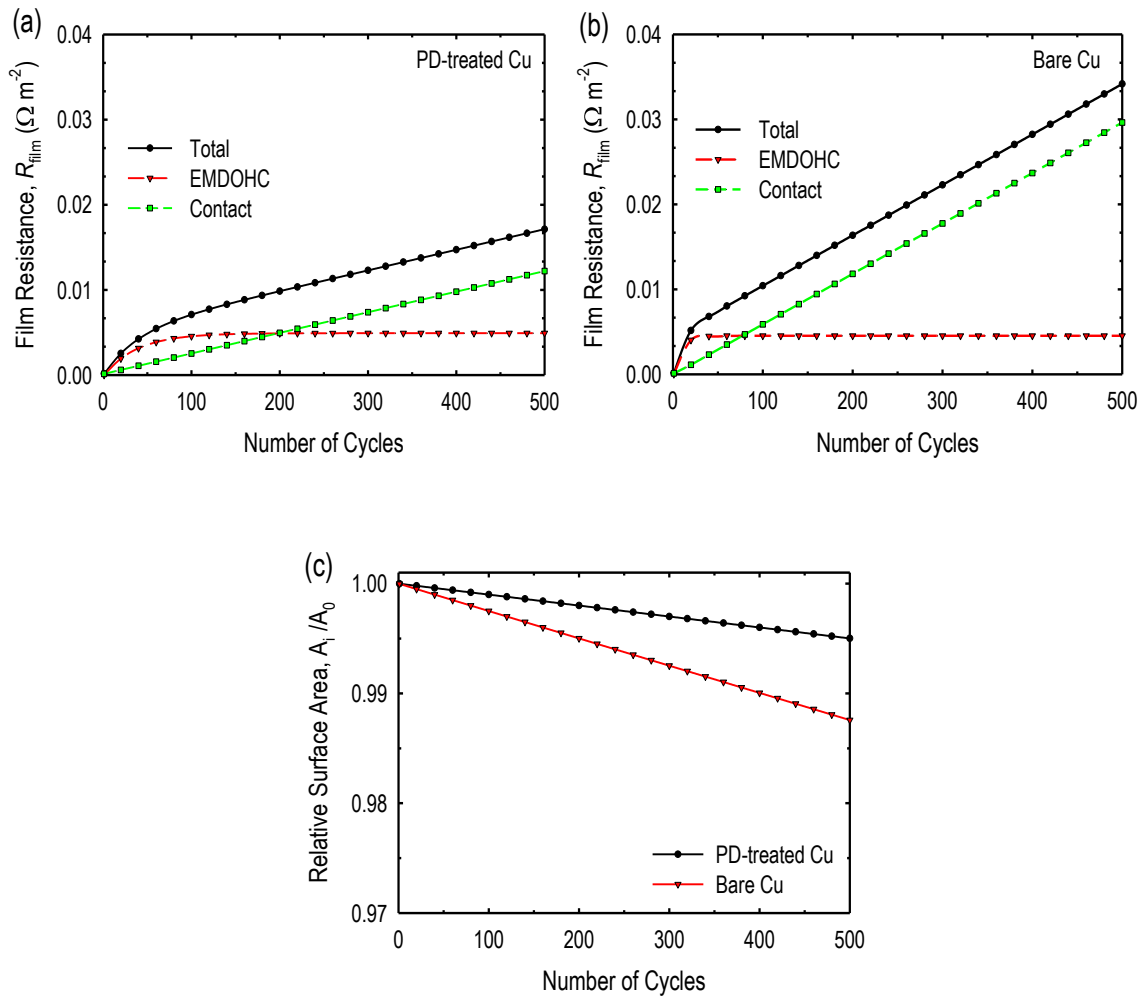
Figure 6.5. Changes in the film resistance in the Li/Si cells with (a) PD-treated and (b) bare Cu current collector, and (c) changes in the surface area.

Even though the PD film reduced the contact resistance in the Li/Si cells, it also increased the charge transfer resistance owing to its insulating-nature. This lead to a reduction in the rate constant for electron transfer in the BV equation [219]. Figure 6.6 shows the relationship between the rate constant (k_p) and number of cycles for Li/Si cells with PD-treated and bare Cu current collector. At the beginning of cycling, electrons tunnel through the PD-interlayer, which leads to a reduction in the rate constant. The tunneling effect is a function of the thickness of the PD-interlayer. As cycling proceeds, the coverage of the PD increases due to the passivation of the surface of the Cu current collector with insulating polymeric film [232], which leads to reduction in the electron transfer rate constant.
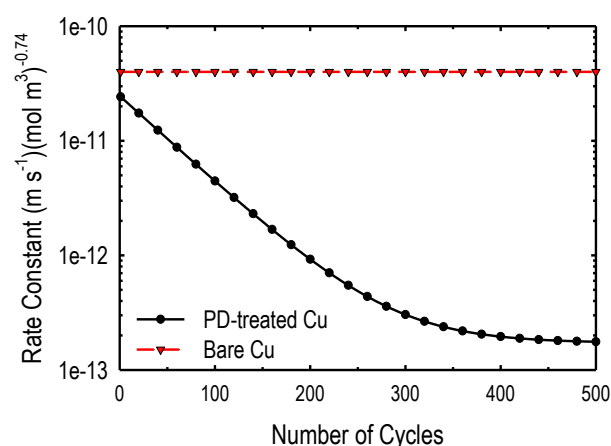
Figure 6.6. Correlation between the electron transfer rate constant and number of cycles for the PD-treated and bare Cu current collector.

Figure 6.7a and 6.7b show the state of charge (SOC) at the beginning of each cycle and at the end of charge (EOC) respectively. The initial SOC (Figure 6.7a), increased rapidly at the early stages of cycling because of the consumption of Li ions to the formation of SEI (EMDOHC). As cycling proceeded, there was a gradual increase in the initial SOC due to additional Li ions loss to the SEI (LiEDC) when the lithiated Si encountered the electrolyte. The rate of increase was higher in the cell with bare than that with PD-treated Cu current

collector. Nevertheless, there was no significant difference between the SOC at EOC for the two systems as illustrated in Figure 6.7b. The result in Figure 6.7b indicates that the amount of Li ions loss to the formation of SEI was almost the same for the cells with a PD-treated and bare Cu current collector as illustrated in Figure 6.7c and 6.7d respectively. Hence, the changes in the initial SOC is due to the difference for Li ions loss to isolation that, is higher for the cells with bare than those with PD-treated Cu current collector as illustrated in Figure 6.7c and 6.7d.
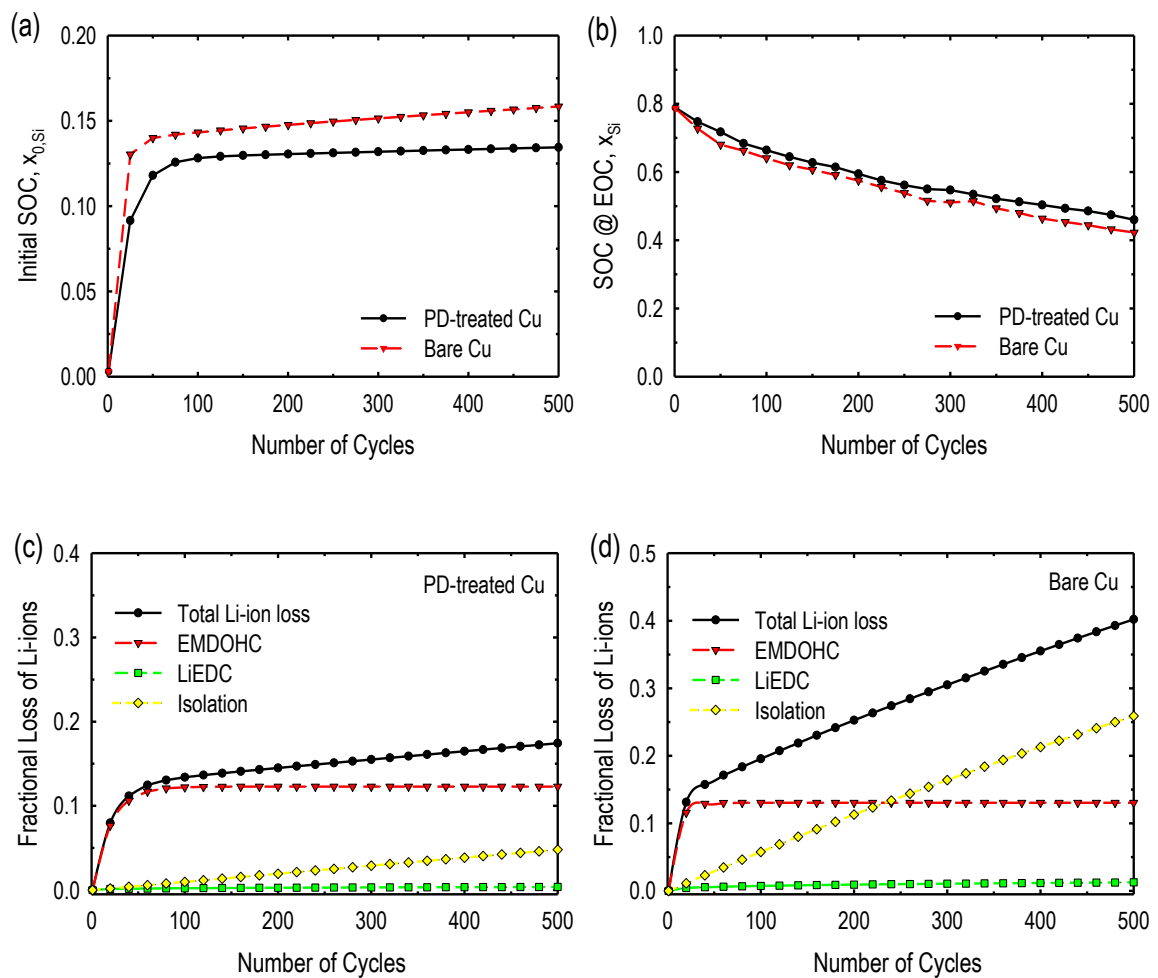
Figure 6.7. Changes in (a) initial SOC and (b) SOC at the the end of charrge (EOC) over 500 cycles. Simulated fractional Li ion loss in Li/Si cells with (c) PD-treated and (d) bare Cu current collector.

The relative contribution of the various degradation mechanisms to capacity fade in the Li/Si cells with PD-treated and bare Cu current collector corresponding to the results in Figure 6.3 are presented in Figure 6.8a and 6.8b respectively. The dominant degradation mechanism in the two cell systems is the contact resistance, which contributed to ca. 13 and 32 % of the capacity fade of the cells with PD-treated and bare Cu current collector, respectively. The enhancement in the contribution of the contact resistance to the capacity retention is due to the reduction of the delaminated Si particles from the surface of the Cu current collector by the PD film. However, the insulating-nature of PD film lead to an increase in the charge transfer resistance which contributed to ca. 11 % of the capacity fade of the cell with PD-treated Cu current collector. The difference between the contribution of Li ions loss to particle isolation to capacity fade; ca. 4 and 14 % for the cells with PD-treated and bare Cu current collector respectively, is attributed to the reduction in the amount of delaminated Si particles which could have been physical isolated from the composite electrode. The loss of Li ions to the formation of SEI (LiEDC) contributed only ca. 0.5 and 1.7 % to the capacity fade for the cells with PD-treated and bare Cu current collector, respectively. Because, the amount of Li ions loss to the formation of SEI (LiEDC) cannot account for the cumulative capacity retention due to the unlimited supply of Li ions from the Li metal as shown if Figure C.1. On the other hand, the increase in resistance due to the formation of the SEI (EMDOHC) contributed to ca. 12 % of the capacity fade in both cell systems. The results obtained are in line with that reported in Chapter 5 when we conducted a capacity fade analysis on the two cell systems.
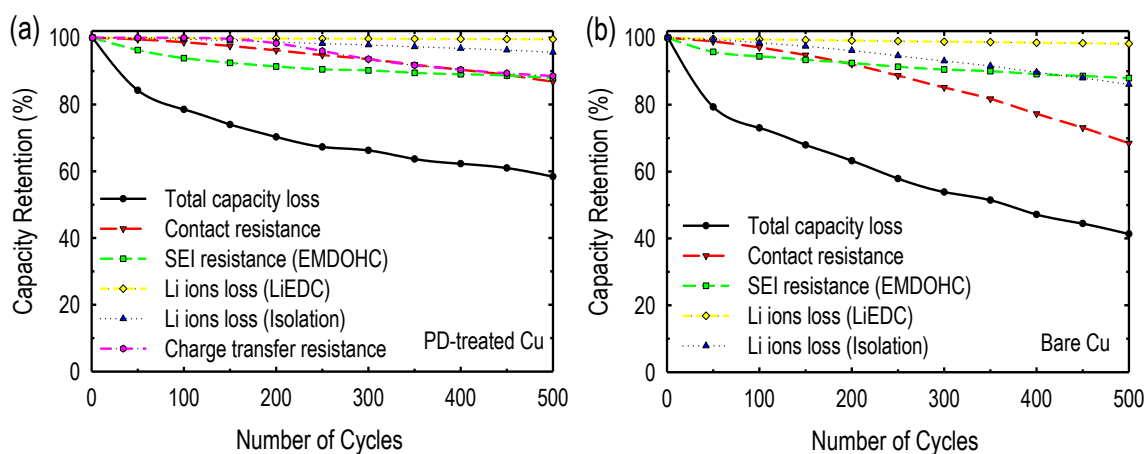
Figure 6.8. Relative contribution of various degradation mechanisms to the cumulative capacity retention for Li/Si cell with (a) PD-treated and (b) Bare Cu current collector.

6. 5 Conclusion

In this study, a comprehensive chemo-mechanical model was developed to describe the various degradation mechanisms of Li/Si cells and the effect of an adhesive film between the Si composite electrode and Cu current collector on the capacity retention. The estimation of capacity loss due to SEI (EMDOHC and LiEDC) was based on conservation of Li ions. The effect of particle isolation was captured in an apparent porosity. The idea of flux tubes was adopted to calculate the contact resistance between the Si composite electrode and Cu current collector where the JKR model limits were used to estimate the critical force. The Li ions inventory during cycling was estimated by considering the Si electrode as a plug flow reactor with recycle. Coupling between the lithiation kinetics and mechanical stress was achieved by modifying the Fick's law of diffusion in the P2D model to include the stress effect.

The major capacity-fading mechanism in Si-based anode is the contact resistance, which was reduced by ca. 18 % after treating the Cu current collector with PD film. The SEI (EMDOHC) resistance contributed to ca. 12 % of the capacity fade. Li ions loss to isolation of Si particles contributed to ca. 14 %, which was reduced to ca. 4 % by the presence of the PD film. Owing to the excess supply of Li ions from the Li metal, there was no significant contribution by Li ions loss to the formation of SEI (LiEDC) to the capacity fade.

Chapter 7

Application of chemo-mechanical model: Design and optimization of high energy density electrodes

7.1 Introduction

A chemo-mechanical degradation model for describing and quantifying the capacity-fading mechanisms of anodes with huge volume expansions and different adhesion strength was presented and validated in Chapter 6, using coin cells with Si anode and Li metal reference electrode and bare and PD-treated Cu current collector. This chapter explores the application of the chemo-mechanical degradation model to design and optimized electrodes with high specific energy density. The main optimization parameter considered in this Chapter is adhesion strength between the composite electrode and the current collector because adhesion strength reportedly have a significant effect on the electrochemical performance of anode material with huge volume expansion such as Si [217,218]. Design and optimization considering such optimization parameter in anode materials with huge volume expansion is of significant relevance in integration of high energy density active materials into LIBs.

Experiments and simulation-based optimization methods have been adopted to study the effect of various cell design parameters on the electrochemical performance of LIBs [254–257]. Choi et al. [258] reported a study on the effect of the $LiCoO_2$ cathode density and thickness on the on the rate capability and cycling performance of the Li ion cells. The authors concluded that, an increase in the thickness of cathode resulted in a significant decline of the rate and cycle performance of the cell. However, changing the cathode density did not

have any significant influence on the performance of the cell. Zheng et al. [259] investigated the influence of the thickness of $LiNi_{1/3}Co_{1/3}Mn_{1/3}O_2$ and $LiFePO_4$ electrodes on the rate performance, energy density, power density, and long-term cycling behavior of LIBs. Similar to the observation made by Choi et al., the electrode thickness had a profound impact on the electrochemical performance of LIBs. The authors correlated the deterioration in the rate performance to the retardation of the transport of Li ions in the electrode owing to the increase in the thickness of the electrodes. Yu et al. [260] conducted tests on coin cells composed of $LiFePO_4$ cathode and a graphite anode while varying the electrode thickness and active material density. In addition, they used an electro- chemical model to analyze the observed effects on cell performance and concluded that ion transport in the electrolyte phase decreases in the case of dense electrodes.

On Si anodes, optimizations are performed to eradicate the issues related to capacity fade due to volume expansion of the Si particles. Lie et al. [261] studied the dependence of fracture on Si anodes by varying the particle size of the individual particles. Upon lithiation of the individual particles of different sizes, they discovered a strong dependence of fracture on the particle size from which they concluded that, the critical particle diameter beyond which the particles neither crack nor fracture was 150 nm. The optimization of the adhesion strength between Si composite electrode via using a more adhesive binder have been presented in previous reports [262–264]. Optimization of the adhesion force between the Si composite electrode via the coating of the surface of the current collector by an adhesive thin film was reported by Cho et al [218]. Therein, the authors reported that, increasing the adhesion force between the Si composite electrode and the current collector enhances the electrochemical performance of the cells. However, the effect of other cell design parameters such as thickness, particle size and porosity, and the maximum adhesion strength required

were not considered, probably due to the huge amount of time involved in carrying out such experiments. Using a multiphysics microstructure-resolved model (MRM), Wang et al. [238] investigated the specific and volumetric capacities of Si nano wall/Li cells as a function of size, length/size ratio, spacing of the nanostructure and Li ion concentration in electrolyte. However, the effect of design parameters related to capacity decay was not considered.

The main objectives of this Chapter are to use the developed chemo-mechanical degradation model to investigate the effect of particle size, porosity, thickness and Li ion concentration, in tandem with the adhesion strength between the Si composite electrode and current collector on the specific capacity of Si/Li cells. The chemo-mechanical model predictions are validated with experimental data obtained from Si/Li cells with bare, PD-treated and a cross-link between the PD and the polymeric binder treated Cu current collector. In addition, the effect of the design parameters of the thin film polydopamine interlayer such as thickness and porosity on the cycle performance will be investigated.

A large part of the work presented in this Chapter was published in [250] presented at the Americas International Meeting on Electrochemistry and Solid State Science (AiMES 2018), the 234th Meeting of The Electrochemical Society (ECS) held at Cancun, Mexico.

7.2 Experiment

In order to meet the optimization objective based on the adhesive strength between the Si composite electrode and the current collector, we designed three types of cells with different adhesion strength as shown in Scheme 7.3. The detail of the cell fabrication and electrochemical test are similar to that described in Chapter 5. The difference is the cell with

the cross-linked PD and polymeric binder, which was achieved by heating the cells with PD-treated current collector overnight in a vacuum oven at 80 ˚C. The rate performance characterization of the as prepared Si electrodes was conducted using 2032 coin-type half-cells (Si/separator/Li metal) at 25 ˚C and various discharge current rates.
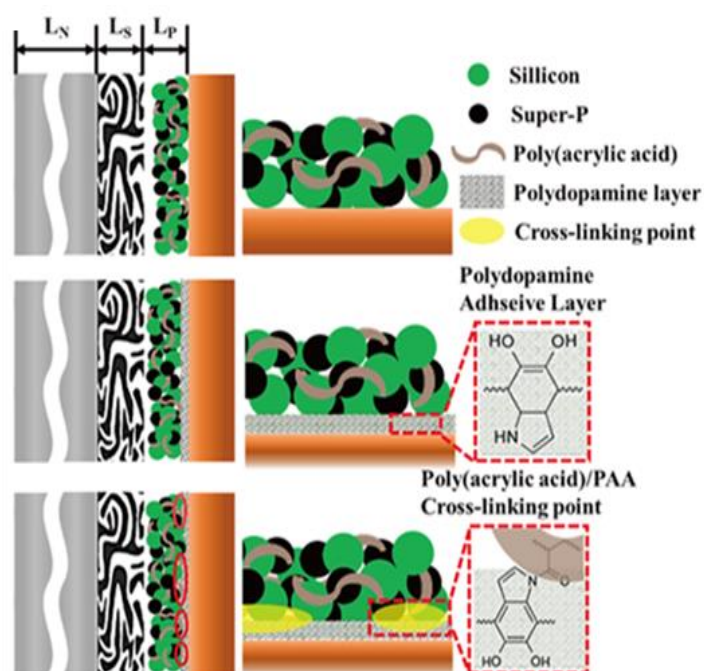
Figure 7.1. Schematic diagram of cell designs used in this study.

7.3 Results and discussion

7.3.1 Experimental results

Figure 7.2 shows the rate performance of the Si electrodes prepared by using a bare (bare), polydopamine (PD)-treated (PD-treated) and crosslinked PD-treated Cu current collector (crosslinked). The charge capacity of the cell strongly depends on the current rate.

Hence, an increase in the current rate for the three cell designs lead to a decrease in the charge capacity. The observed decrease in capacity can be attributed to the retardation of Li ions diffusivity due to the compressive stress generated during lithiation [265,266]. At high current rate, the compressive stress is sufficiently high to detain lithiation, leaving unlithiated particles electrochemically inaccessible and thereby resulting in a reduced capacity. However, the rate at which the capacity decrease as well as the initial capacity depended on the adhesion strength between the Si composite electrode and the current collector which is 245, 297.6, and 352.2 N m^{-1} for the bare, PD-coated and the crosslinked respectively as confirmed by using a surface and interfacial cutting analysis system (SAICAS). As shown in Figure 7.2, cell with the crosslinked PD-treated Cu current collector gave a higher initial capacity and a better rate performance as compared to that with the PD-treated and bare current collector. This was due to the ability of the crosslinked PD-binder to maintain the contact between the electrode and the current collector even at higher current rate where the compressive stress was quite high.
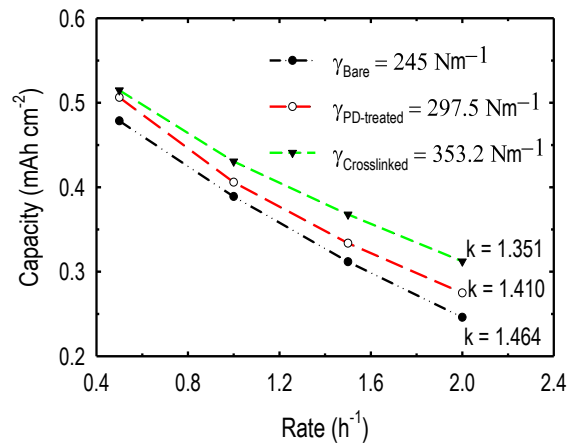
Figure 7.2. Experimental rate performance and the Peukert coefficient of the Si composite electrodes prepared by using a bare, PD-treated Cu and crosslinked Cu current collector.

Figure 7.3 also illustrate the Peukert coefficients, which were determined by fitting the charge capacities of the various cells at specified current rates (ranging from 0.5 C to 2 C) to the Peukert's law. The Peukert's law is given as $C = i^k \times t$, where k is the Peukert coefficient and t is the nominal charge time (in hours) for a specific C-rate (in Amperes), and C is the theoretical capacity of the specific cell under consideration. To be specific, a higher Peukert coefficient value signifies a lower cell rate performance. As the adhesive strength increased, the Peukert coefficient reduced, indicating the dependence of the rate performance on the adhesive strength between the composite electrode and the current collector. The Peukert law assumes that, at a given current rate all the reaction occurring in the electrode goes to completion. Nevertheless, for the all the three cells the electrode reaction did occur to completion during the charging process and the cut-off potential was reached preceding the completion of the electrochemical reaction at the surface of the electrodes with the rate of completion being higher in cells made with bare Cu current collector. This impromptu reaching of the cut-off potential can be related to both the polarization caused by high internal contact resistance and to the slow diffusion of Li ions due to the generated compressive stress as a result of large volume expansion [267].

7.3.2 Model validation

To validate the chemo-mechanical model, the experimental voltage profiles of the three cells with bare, PD-treated and cross-linked Cu current collector, during the galvanostatic charging at various current rates of C/2, 1 C, 1.5 C and 2 C were simulated and validated with the experimental data, and presented in Figure 7.3. The solid lines illustrate the predicted values, which were based on the parameters listed in Table 6.1. The simulated charge profiles were in good agreement with the experimental data for all the current rates

but with slight deviation at the initial stages of that at a current rate of 2 C. The simulations were conducted under the same condition for all the three cases. As the charge rate was increased, there was a slight steady increase in the IR drop. The increase in the IR drop was more visible in the cells with the bare Cu current collector as compared to the PD treated and the cross-linked Cu current collector. In addition, the initial charge capacities of the three cells were different with the cells with the cross-linked Cu current collector exhibiting the highest charge capacity. The enhanced adhesion strength between the silicon composite electrode and the current collector for the PD-treated and cross-linked Cu current collector was due to the formation of covalent bonds by the coating layer [32]. Thus, the difference between the IR drops in the voltage profiles as well as the difference in the initial discharge capacities of the three cells can be attributed to the adhesion strength between the Si composite electrode and the current collector.
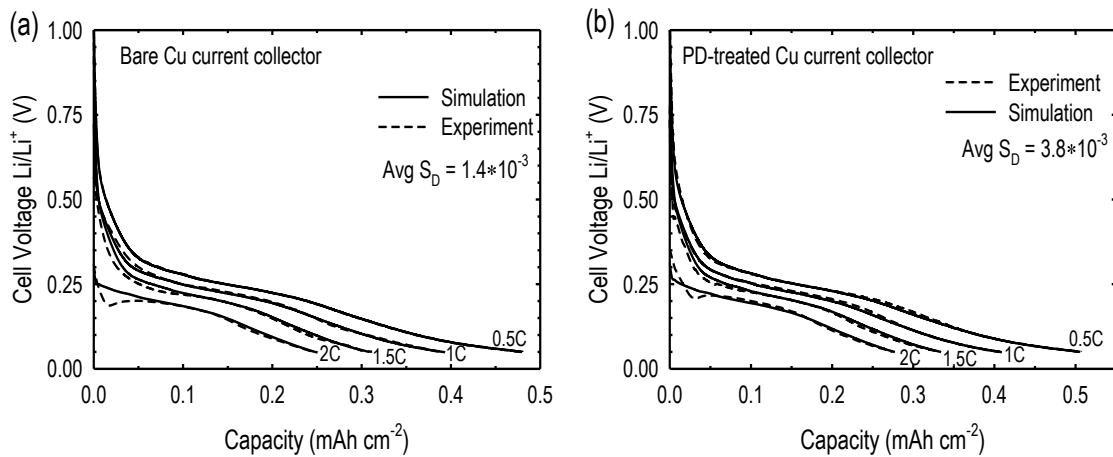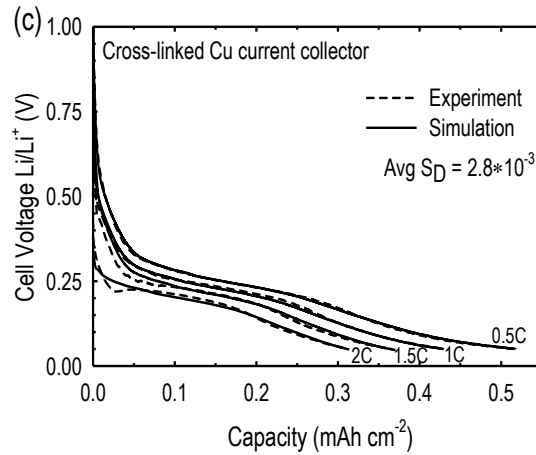
Figure 7.3. Experimental and simulation voltage profiles of the three cells with (a) bare (b) PD-treated and (c) cross-linked PD treated Cu current collector, during the galvanostatic charging at various current rates of C/2, 1 C, 1.5 C and 2 C based on the parameters listed in Table 6.1.

7.3.3 Simulation results

Figure 7.4 shows the simulated salt concentration profiles across the Si composite electrode for the three cells at the end of the galvanostatic charge (lithiation) at different current rates. The normalized distance indicates the distance from the electrolyte/Si composite interface (0) to the Si composite/current collector interface (1). The salt concentration at both the electrolyte/Si composite and the Si composite/current collector interface varies according to the adhesion strength between the Si composite electrode and the Cu current collector. The polydopamine in addition to enhancing the contact between the Si composite and the Cu current collector also alter the surface of the Cu current collector from hydrophobic to hydrophilic with the hydrophilicity being higher in the crosslinked PD binder. The enhanced hydrophilicity increased the supply of Li ions to the surface of the Si particles. This analogy was demonstrated experimentally by Cho et al. [218] when water droplet was dropped onto

the surface of each treated and bare current collector. The PD treated Cu current collector had a much smaller contact angle of 46 ° than the bare Cu current collector, which had 93 °. This can be attributed to the presence of the polar functional groups in the polydopamine which contains nitrogen and oxygen [268,269]. Also, it can be deduced from Figure 7.4 that, the rate at which the salt concentration decreases across the cell for all the three cells were identical at each current rate but the rate is quite higher at the 2 C current rate owing to the solution phase limitation in LIBs [222,270].
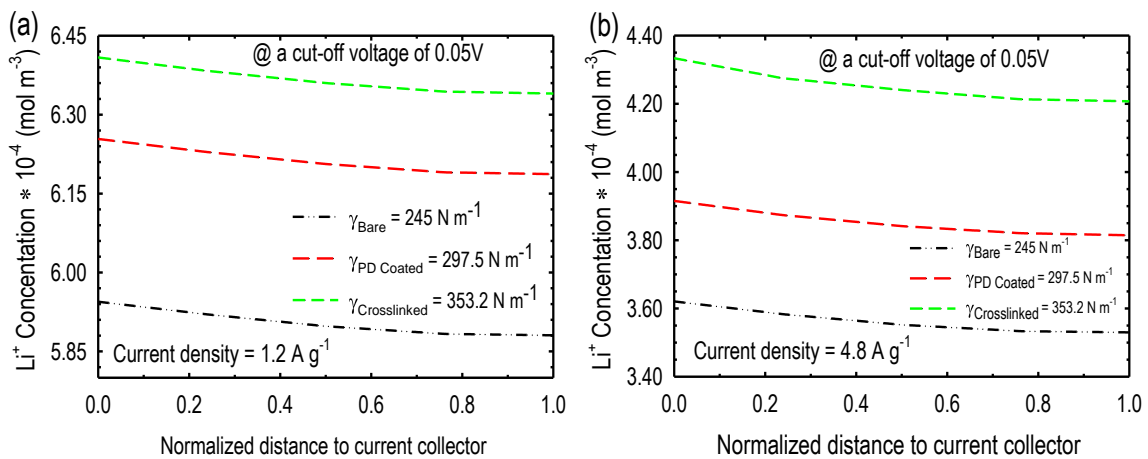
Figure 7.4. Simulated salt concentration profiles across the Si composite electrode for the bare, PD-treated and the cross-linked Cu current collector at the end of lithiation at (a) 0.5 C current rate and (b) 2 C current rate. The normalized distance indicates the distance from the electrolyte/Si composite interface (0) to the Si composite/current collector interface (1).

Figure 7.5 shows the Li ion concentration in the solid phase across the Si composite electrode at the end of the lithiation processes for the three cells designs. The simulation was performed at a low current density of 0.5 C for Figure 7.5a and high current density of 2 C for Figure 7.5b. Similar to the results obtained in Figure 7.4, the Li ion concentration in the solid at the two interfaces are different for the three cells, even though a similar binding material (PAA) was used in the electrode. The only difference is the adhesion force between

the Si composite electrode and the Cu current collector. This illustrates the effect of the adhesive strength between the Si composite and the current collector have on the capacity of the cell. That is, the cell with the cross-linked Cu current collector exhibited a relatively higher capacity than that of the PD-treated and bare Cu current collector due to its higher Li ion concentration across the Si composite electrode as compared to the other two. Different from the results obtained in Figure 7.4, the rate at which the Li ion concentration reduces across at the two current rates considered in this study was almost the same. This signifies that, the solid-state diffusion limitations are not dominant in the cells considered in this study probably due to their higher porosity of 0.85.
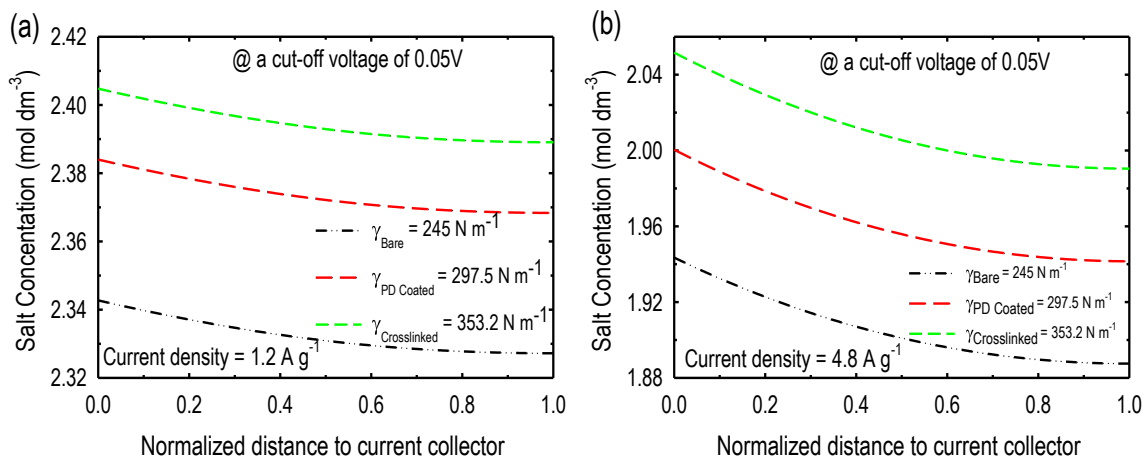
Figure 7.5. Simulated Li ion concentration in the solid phase across the Si composite electrode for the bare, PD-treated and the cross-linked Cu current collector at the end of the galvanostatic lithiation at (a) 0.5 C current rate and (b) 2 C current rate.

Figure 7.6 illustrates the contact resistance and the adhesive strength between the Si composite electrode and the current collector as a function of the current for the three cells. The adhesive strength was determined at the various rates by fitting the model predictions to the experimental data using the Levernberg-Marquardt non-linear least squares fitting technique. From Figure 7.6a, the contact resistance increased linearly with an increase in the

current rate. The experimental rate performance was conducted over 30 cycles at the end of the 3 C current rate. In view of this, the contact area between the Si composite electrode and the Cu current collector reduces. This led to the gradual increase in the contact resistance. Experimentally, it has been reported that, the Si composite electrode losses physical contact with the Cu current collector as cycling proceeds [218,239,271] and thereby increasing the contact resistance at the interface, which is in line with the results presented in Figure 7.6a. Moreover, the contact resistance in Fig 7.6a increased linearly with a decrease in the adhesive strength at the various current rates. This is because, as the adhesive strength increases, the contact area between the Si composite electrode and the Cu current collector also increases resulting in a lower contact resistance.

From Figure 7.6b, the adhesive strength of the three cells at the surface of the Cu current collector reduced as the current rate increased form 0.5 C to 3 C. As mentioned earlier, the rate performance was done over a number of cycles, thus as the number of cycles increased, the contact area between the Si composite electrode and the Cu current collector reduces due to the compressive stress induced at the interface owing to the volume expansion of the Si particles. The reduction in the contact area can be attributed to the weakening of the adhesive strength of the coatings at the interface as cycling proceeds. Thus, from Figure 7.6b the adhesive strength reduced with cycling, with the rate of reduction being higher in the bare Cu current collector due to its low initial adhesive strength. The adhesive strength of the cross-linked, PD-treated Cu and the bare Cu current collector decreased by ca. 48, 25, and 22 % respectively after 3 C current rate.
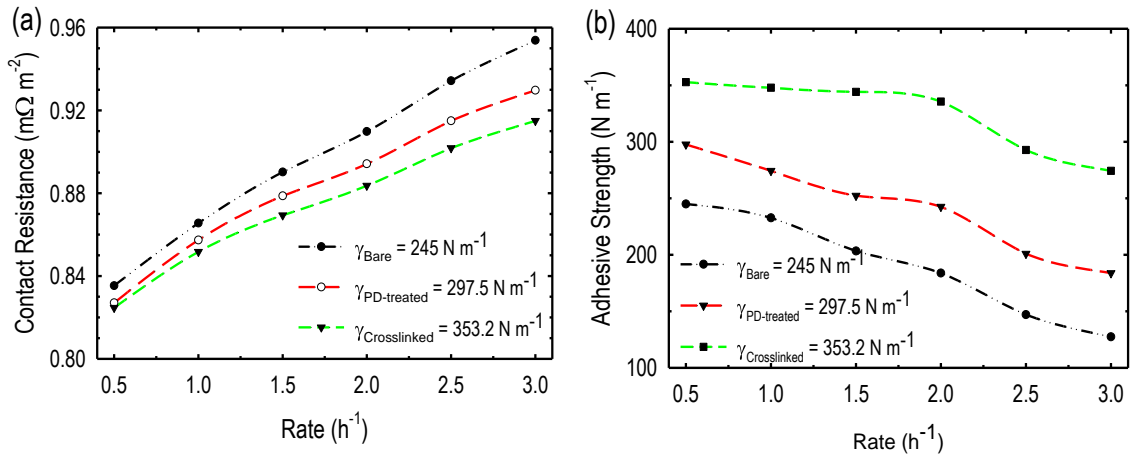
Figure 7.6. (a) Contact resistance and (b) Adhesive strength between the Si composite electrode and the current collector as a function of various current rates for the bare, PD-treated and the crosslinked Cu current collector.

Figure 7.7 show the simulated results for the specific capacity as a function of the adhesive strength as well as different electrode thicknesses, salt concentrations, particle sizes, and electrode porosities, at current rates of 1 and 4C. The specific capacity increases with increasing adhesive strength in all four cases for both current rates. Increasing the electrode thickness results in a decrease in the specific capacity, with a higher rate of decrease at the 4C rate compared to that at 1C (Figure 7.7a). On the other hand, increasing the initial salt concentration (Figure 7.7b) does not significantly increase the specific capacity at either the low or the high current rate. The specific capacity decreases with the growth in particle radius, with a higher rate of decrease at a high current rate (Figure 7.7c). The specific capacity increases as the electrode porosity declines for both current rates (Figure 7.7d). However, the specific capacity decreases after the electrode porosity decreases below 0.5 and 0.6 for the lower and higher current rates, respectively. In addition, beyond an electrode thickness of 20 μm (Figure 7.7a) and particle radius of 75 nm, the

specific capacity is insignificant at the 4C rate for the lower adhesive strength but increases as the adhesive strength increases.
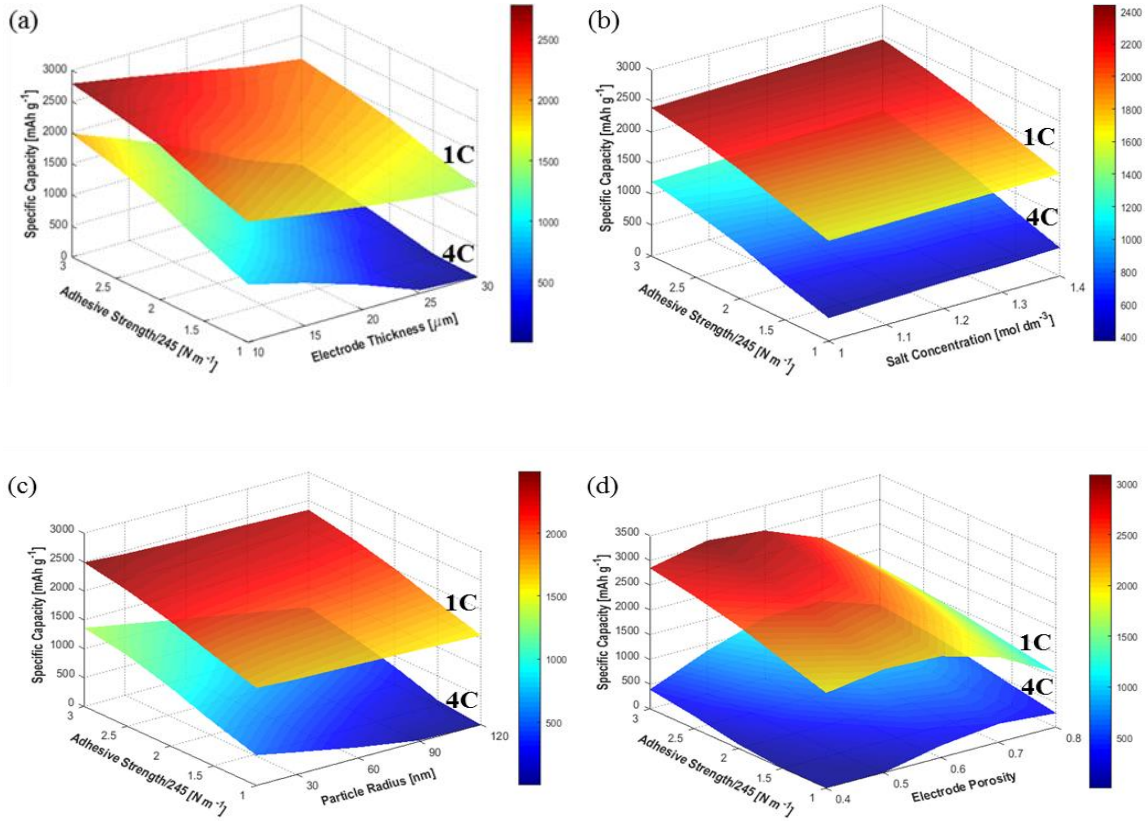
Figure 7.7. Specific capacity as a function of the adhesive strength and (a) Electrode thickness (b) Salt concentration (c) Si particle size and (d) Electrode porosity, at different current rates of 1C and 4 C.

The developed degradation model was used to study the effect of the design parameters of the PD thin film on cycle performance. The obtained results are presented in Figure 7.8. From Figure 7.8a, increasing the adhesive strength did not have any effect on the capacity retention during the first 50 cycles but showed a significant increase as cycling proceeded. Because, at the beginning of cycling, the SEI resistance controls the capacity fade, however increasing adhesive strength reduces the contact resistance (Figure C.2a) and Li ions loss to particle isolation (Figure C.2b) which control the capacity fade at the later stages of cycling.

Previous experimental studies, suggested that, the coverage and thickness of the PD film could be regulated depending on the type of oxidant and deposition time [272]. Increasing the thickness of the PD film from 8 nm to 96 nm for a completely coated Cu surface (coverage = 1), resulted in a decrease in the initial charge capacity but the rate of capacity fade remained almost the same. A further increase in thickness beyond 96 nm lead to a further decrease in the in initial charge capacity and drastic increase in the rate of capacity of fade (Figure 7.8b). Because, increasing the thickness of the PD-film slows the charge transfer rate (Figure C.3a) owing to the tunneling of electrons through a thicker insulating-layer [273]. However, for a partially covered Cu surface (coverage = 0.8), increasing the thickness of the PD film did not have any significant effect on the capacity retention during the first 200 cycles but reduced as the number of cycles increased with rate of capacity fade being higher for thicker PD films (Figure 7.8c). Because, even though the thickness of the electron tunneling layer is increased, the rate of charge transfer on the uncovered part of the Cu current collector is very high which nullifies the electron tunneling effect at the initial stages of cycling. As cycling proceeds, the uncovered part of the Cu current collector is passivated by an insulative-polymeric layer [232] resulting in a reduction in charge transfer rate (Figure C.3b) and dominance of the tunneling effect. Increasing the PD film coverage, resulted in a decrease in the initial charge capacity but the capacity retention was better for cells with a higher PD film coverage than those with lower PD film coverage (Figure 7.8d). Because a lower PD film coverage increases, the rate of charge transfer at the initial stages of cycling but the rate gradually reduces as cycling proceeds (Figure C.4) owing to the covering of the uncovered surface by an insulating polymeric film. The reduction in the capacity retention as the PD film coverage reduced, was due to the increase in the contact resistance (Figure C.5a) and the increase in the Li ions loss to isolation (Figure C.5b) owing the large amount of delaminated Si particles.
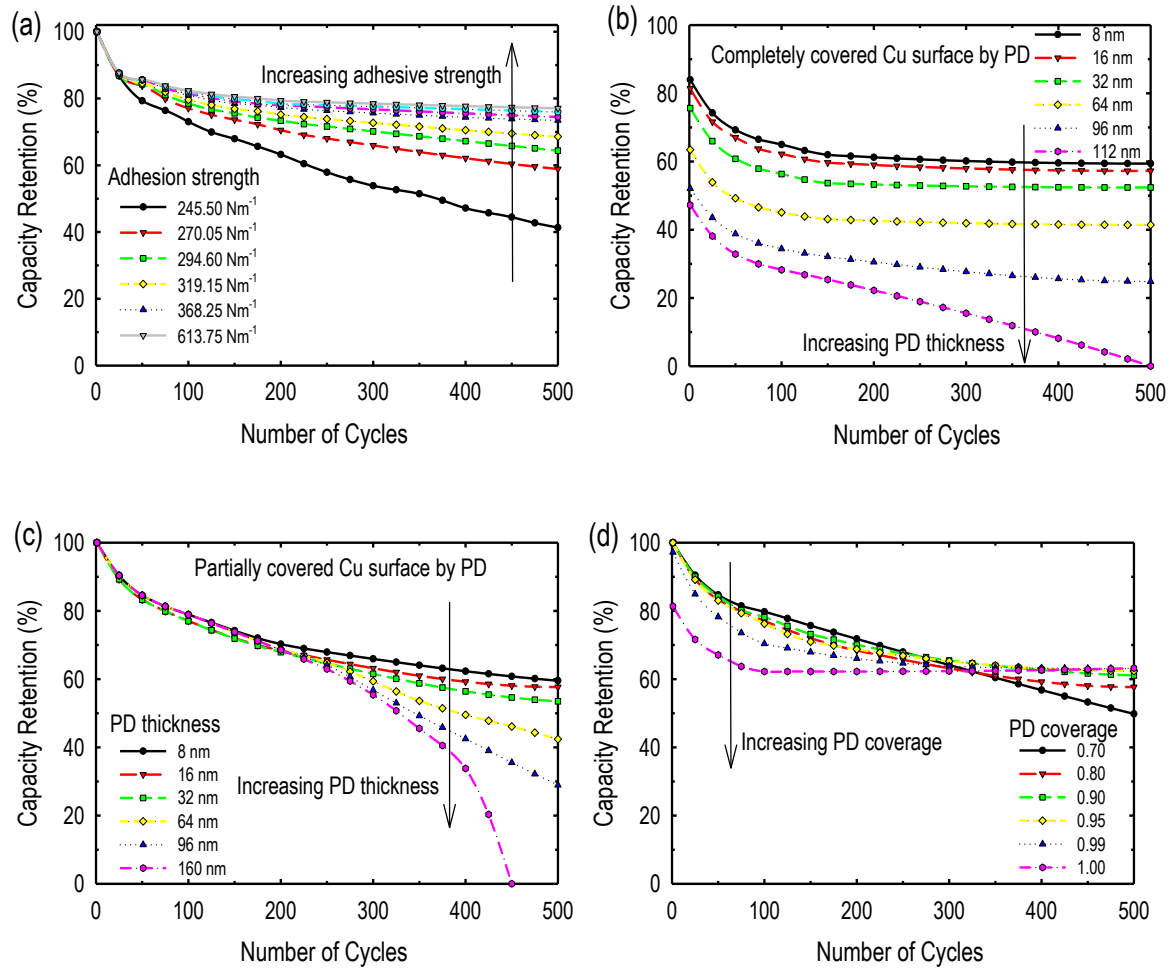
Figure 7.8. Effect of PD film design parameters: (a) adhesion strength, (b) PD film thickness (coverage = 1), (c) PD film thickness (coverage = 0.8), and (d) PD film coverage on capacity retention of Li/Si cells.

7.4 Conclusion

The proposed chemo-mechanical model was used to investigate the specific capacity as a function of Si electrode thickness, Li ion concentration in the electrolyte, Si nanoparticle size and porosity. Increasing the adhesive strength between the Si composite electrode and Cu current collector by coating the latter with binder materials of different adhesive strengths increases the contact radius between the Si particles and current collector surface, thus reducing the contact resistance and enhancing the electrochemical performance of the cell. The adhesive strength is reduced with increasing cycle number due to volume expansion, resulting in an increase in the contact resistance. The specific capacity decreases with an increase in both the Si electrode thickness and particle size at both high and low current rates, with a lower rate of decrement for cells with higher adhesive strength. The developed model can be used for cell design optimization and as a guide for selecting a binder to coat the current collector with a specific adhesive strength for a given application.

In addition, the chemo-mechanical model was used to study the effect of a thin film interlayer on the cycling performance of Li/Si cells. Increasing the adhesion strength between the Si composite electrode and Cu current collector enhanced the capacity retention until a threshold (ca. 2.5 times of the adhesion strength of the bare Cu current collector system) where the capacity fade is no longer controlled by contact resistance and Li ions loss to particle isolation. A thinner PD film interlayer between the Si composited material and the Cu current collector with a coverage of ca. 0.95 is more suitable for a better electrochemical performance of Si-based Li ion batteries. Replacing the insulating PD film with a conductive adhesion film will aid in improving the capacity retention of Si-based anodes for LIBs.

Chapter 8

Conclusion and future work

This work presents a holistic approach for the diagnosis and modeling of capacity fading in Li-ion cells with high energy density active materials. The cell degradation information on the individual active materials contained in the parameters that changes with cycling in a multiphysics-based model is exploited to identify the nature and extent of the capacity fade. To further predict the capacity-fading mechanism and eliminate possible long-term cell failures, holistic models describing the identified degradation mechanisms are developed to quantify the contribution of the various capacity-fading mechanisms. The devised comprehensive models are employed to theoretically design robust electrodes that can withstand the major degradation mechanisms and to propose a fast but accurate accelerated cyclic aging analysis method for Li ion batteries.

8.1 Contributions

The contributions of this work can be summarized as follows:

1. A physics-based model capacity fade analysis of spinel-based cathode materials for Li-ion batteries [185].

2. A mathematical model for the cyclic aging of spinel-based cathode materials for Li-ion batteries [192].

3. Time-effective accelerated cyclic aging analysis of Li-ion batteries using developed physico-chemical model [211].

4. A multiphysics-based capacity fade analysis of high volume expansion anodes with an adhesive thin film interlayer [219].

5. A comprehensive chemo-mechanical degradation model on the cyclic aging of anode materials with high volume expansion.

6. Design and optimization of robust and high energy density electrodes for Li-ion batteries using developed chemo-mechanical degradation model [250].

8.1.1 Multiphysics-based model capacity fade analysis

To address the issues related to non-destructive but effective means of extracting capacity-fading mechanisms of Li-ion cells, a multiphysics-based model (P2D model) alongside a parameter estimation method (the Levernberg-Marquardt method) was used to identify the various degradation mechanisms of high energy density electrodes. Based on the monitoring of the model parameters that changed with cycling using the Levernberg-Marquardt parameter estimation method. This approach was effectively applied to identify the degradation mechanisms of two different cells systems: Spinel-based cathode material and graphite Li-ion cell, and silicon anode with a bare Polydopamine treated Cu current collector.

The capacity fade analysis method using the non-destructive multiphysics-based model was effectively used to unveil the dependency of the degradation mechanisms of various active materials on temperature. The major degradation mechanisms of various active materials at different operating conditions can be identified and addressed effectively without spending much time or resources by this approach. The positive and negative effects of the measures taken to address degradation issues such as the use of adhesive thin films to

eliminated delamination problems in high volume expansion anodes can be ascertain using this non-destructive capacity fade analysis method.

8.1.2 A capacity fade model for spinel-based cathode materials

The key features of the developed capacity fade model are its ability to

- account for most of the chemical degradation mechanisms in Li-ion batteries.

- account for different operating conditions such as temperature and cut-off voltages.

- be adopted for different cell chemistries.

Even though the parameterization of the developed physico-chemical model is difficult, it takes into account different operating conditions such as temperature and cut-off voltages, which are known to have a great influence on the capacity fading of Li-ion batteries. For most developed physics-based degradation model, only the degradation effect on the anode such as the formation of SEI at the anode are considered. However, the degradation of the cathode also plays a significant role in the capacity fading of the cell and must be considered. Thus, a comprehensive capacity fade model that considers most of the chemical degradation in both the cathode and anode is a necessity for accurate prediction of cell cycle life and detection of long-term failures for safety reasons.

8.1.3 A time-effective cyclic accelerated aging analysis framework

Critical innovations in the proposed framework include its

- ability to account for the degradation mechanisms of different active materials from the PCM-PCEM.

- ability to determine the maximum upper limit temperature required for accelerated cyclic aging analysis with few experimental data.

- simple yet effective and accurate

The proposed framework can be applied to different cell chemistries since the PCM-PCEM model adopted in the framework considers both the linear and non-linear relationship between capacity decay and number of cycles. This makes it suitable for describing and effectively predicting the cycling performance of Li-ion cells with different active materials at different operating conditions such as temperature.

The adopted PCM-PCEM can effectively predict the cycle performance at different temperatures after validating it with experimental data obtained at two extreme temperatures. Thus, the number of experiments required to determine the maximum temperature at which the accelerated cyclic analysis can be conducted without altering the degradation mechanism is reduced to only two. This makes the proposed framework time effective and less expensive since the number resources required is less.

Even though the adopted PCM-PCEM is difficult to parameterize, the SELM developed from the predicted data is quite simple and easy to parameterize. The coupling of the sophisticated but accurate PCM-PCEM and simple SELM for the accelerated cycling aging analysis based on two sets of experimental cycling data, makes the proposed framework simple, accurate and easy to apply.

8.1.4 A chemo-mechanical degradation model

The crucial features of the chemo-mechanical model include its ability to

- account for both chemical and mechanical degradation mechanisms.

- account for adhesion properties in the electrode

- be adopted for different cell chemistries.

- used for developing robust electrodes with high specific capacity

Unlike previously reported degradation model, the chemo-mechanical model developed in this work simultaneously account for both chemical and mechanical degradation. This feature makes it plausible for describing the cycle performance of electrodes, which experience both degradation mechanism owing to volume expansion of particles. Adhesion force is one of the most important parameters considered in designing robust electrodes to withstanding huge volume expansion and improve cycle life of Li-ion secondary batteries. Thus, a model that considers this factor can aid in designing better electrodes with high specific capacity and long cycle life.

Even though the model was developed for anode with materials with high volume expansion, it can be adopted for other cell chemistries with little or no volume expansion. Because the chemical part of the model considers almost all the chemical degradation mechanisms of active materials employed in Li ion batteries. The mechanical part deals with the crack formation and effect of volume expansion on the lithiation kinetics.

8.1.5 Practical relevance

The main motivation behind the work presented in this thesis is the importance to practical application. The developed models were built for and validated with state-of-the-art coin cells made from commercially available active materials. This work is purposed to be applicable to Li ion battery life-time prediction systems and design of new electrodes materials with high specific energy and enhanced cycle life.

Life-time prediction systems of Li-ion batteries utilizing the framework presented in this work can operate in this manner. The physico-chemical model incorporated into a porous composite electrode model (PCM-PCEM) is validated with experimental data obtained from cells at room and extreme temperatures. The validated PCM-PCEM is used to predict the cycle life of the cell at different operating temperatures. The data obtained from the model predictions are used to develop a simple life empirical model (SELM). The developed SELM is then used to extrapolate the number of cycles obtained at the various high temperatures to room temperature. The parameters of the SELM can be used to determine the maximum temperature beyond which the degradation mechanisms changes. This maximum temperature is then used to determine the number years the battery can last before reaching the minimum capacity required for granting a warranty.

The models developed in this thesis can be used to design new electrodes in this manner. The model is used to quantify the degradation mechanism of the electrode by fitting the model predictions to experimental data obtained from Li-ion cells comprising the electrodes of interest. The identified major contributing degradation mechanism can then be controlled using various remedies. The effect of electrode physical parameters can be regulated to analyze their effect on the various degradation mechanisms. Physical parameters that have positive effects are experimentally modified accordingly.

Greater certainty about the reliability of life prediction under real operating conditions can be a major step for dependable integration of Li-ion batteries into vehicles and elimination of warranty issues. Hence, the findings presented in the work are of both technological and commercial interest.

8.2 Future work

A number of avenues for further research on modeling and simulation of high energy density Li-ion batteries have been unveiled because of the studies conducted in this thesis.

8.2.1 Modeling of Ni-rich cathode materials

Replacing Co with Ni in layered structured cathode active material have been reported to yield higher lithium utilization and thereby higher specific capacities. The energy density of Ni-rich cathode (800 Wh kg^{-1}) materials are by far one of the highest in Li ion batteries. However, this material suffers from cation mixing owing to the similar radius of Li^+ (0.076 nm) and Ni^{2+} (0.069 nm). This phenomenon causes problems such as capacity loss and structure deterioration, acceleration of capacity fade due to side reaction at elevated temperatures and poor thermal stability [31]. The mechanism constituting the capacity fade is complex and the impact of each degradation mechanism is not well quantified. Thus, an extension of the work presented in this thesis to identify, quantify and model the various degradation mechanisms of Ni-rich cathode material is of great interest in my future work.

8.2.2 Exploring the negative side of adhesive thin film interlayers

The major reason for the failure of high energy density anode materials such as Si is huge volume expansion. This leads to pulverization, delamination, and formation of unstable SEI. To deal with this issue, particularly for delamination, the use of adhesive thin film interlayers has proven to be effective. However, as presented in this work, these thin film interlayers have both positive and negative sides. The information provided in this work about the negative side was limited to only the mechanical reasons. However, to understand and

improve the performance of these adhesive thin film interlayers, there is the need to couple the capacity fade model designed in this work with molecular dynamics simulation (MDS) to explore the chemical effects.

8.2.3 Investigation into degradation mechanisms of large format Li ion cells

One of the major drawbacks of the results presented in this work is that, the developed model was validated with experimental data obtained from coin cells. Unlike large format Li-ion cells, the heat generated from coin cells are easily dissipate thus energy balance equations were ignored. However, real battery systems employ large format cell and pouch cell system where the heat generated can lead to safety issues and must be accounted for in degradation models. Thus, the model developed in this work will be extended to large format Li-ion cells to include thermal effect in the model.

8.2.4 Short term future research

My short-term goal is to apply the developed framework to large format batteries and battery pack systems composed of different cell chemistries. This will help to develop commercially applicable degradation models based on identified degradation mechanism during the operation of the batteries and to accurately predict their end-of-life. Post-mortem analysis will be conducted on the faded cells to confirm the identified degradation mechanisms. This will improve the fundamental understanding of the degradation mechanism and enable the development of a chemistry-agnostic degradation model for battery lifetime prediction and accelerated aging analysis. A principled classification of the degradation mechanism based on decision making theories such as the Bayesian theory will be conducted compared to just qualitative analysis.

My long-term goal is to extend my modeling and simulation skills to other electrochemistry systems such as solar cells, electrochromic devices, and fuel cells.

References

[1]   N. Kim, A. Moawad, N. Shidore, and A. Rousseau, "Fuel Consumption and Cost Potential of Different Plug-In Hybrid Vehicle Architectures", *SAE Int. J. Altern. Powertrains* **2015**, *4*, 88.

[2]   A. Opitz, P. Badami, L. Shen, K. Vignarooban, and A. M. Kannan, "Can Li-Ion batteries be the panacea for automotive applications?", *Renew. Sustain. Energy Rev.* **2017**, *68*, 685.

[3]   H. Budde-Meiwes, J. Drillkens, B. Lunz, J. Muennix, S. Rothgang, J. Kowal, and D. U. Sauer, "A review of current automotive battery technology and future prospects", *Proc. Inst. Mech. Eng. Part D J. Automob. Eng.* **2013**, *227*, 761.

[4]   J.-M. Tarascon and M. Armand, "Issues and challenges facing rechargeable lithium batteries", *Nature* **2001**, *414*, 359.

[5]   W. A. Appiah, J. Park, S. Song, S. Byun, M.-H. Ryou, and Y. M. Lee, "Design optimization of $LiNi_{0.6}Co_{0.2}Mn_{0.2}O_2$/graphite lithium-ion cells based on simulation and experimental data", *J. Power Sources* **2016**, *319*, 147.

[6]   N. Nitta, F. Wu, J. T. Lee, and G. Yushin, "Li-ion battery materials: present and future", *Mater. Today* **2015**, *18*, 252.

[7]   S.-T. Myung, F. Maglia, K.-J. Park, C. Seung Yoon, P. Lamp, S.-J. Kim, and Y.-K. Sun, "Nickel-Rich Layered Cathode Materials for Automotive Lithium-Ion Batteries: Achievements and Perspectives", *ACS Energy Lett.*, **2017**, *2*, 223.

[8]   R. Yazami and P. Touzain, "A reversible graphite-lithium negative electrode for electrochemical generators", *J. Power Sources* **1983**, *9*, 365.

[9]   M. Winter, J. O. Besenhard, M. E. Spahr, and P. Novák, *Adv. Mater.,* "Insertion Electrode Materials for Rechargeable Lithium Batteries"*,* **1998**, *10*, 725.

[10]   R. A. Huggins, "Lithium alloy negative electrodes" „*J. Power Sources* **1999**, *81–82*, 13.

[11]   H. Wu and Y. Cui, "Designing nanostructured Si anodes for high energy lithium ion batteries", *Nano Today* **2012**, *7*, 414.

[12]   M. T. McDowell, S. W. Lee, W. D. Nix, and Y. Cui, "Studying the Kinetics of Crystalline Silicon Nanoparticle Lithiation with In Situ Transmission Electron Microscopy", *Adv. Mater.* **2013**, *25*, 4966.

[13]   J. W. Choi and D. Aurbach, "Promise and reality of post-lithium-ion batteries with high energy densities", *Nat. Rev. Mater.* **2016**, *1*, 16013.

[14]   R. Deshpande, M. Verbrugge, Y.-T. Cheng, J. Wang, and P. Liu, "Battery cycle life prediction with coupled chemical degradation and fatigue mechanics", *J. Electrochem. Soc.* **2012**, *159*, A1730.

[15]   D. S. Jung, T. H. Hwang, S. Bin Park, and J. W. Choi, "Spray drying method for

large-scale and high-performance silicon negative electrodes in Li-ion batteries", *Nano Lett.* **2013**, *13*, 2092.

[16]   I. H. Son, J. Hwan Park, S. Kwon, S. Park, M. H. Rümmeli, A. Bachmatiuk, H. J. Song, J. Ku, J. W. Choi, J. Choi, S.-G. Doo, and H. Chang, "Silicon carbide-free graphene growth on silicon for lithium-ion battery with high volumetric energy density", *Nat. Commun.* **2015**, *6*, 7393.

[17]   T. Kwon, Y. K. Jeong, I. Lee, T.-S. Kim, J. W. Choi, and A. Coskun, "Systematic Molecular-Level Design of Binders Incorporating Meldrum's Acid for Silicon Anodes in Lithium Rechargeable Batteries", *Adv. Mater.* **2014**, *26*, 7979.

[18]   C. Wang, H. Wu, Z. Chen, M. T. McDowell, Y. Cui, and Z. Bao, "Self-healing chemistry enables the stable operation of silicon microparticle anodes for high-energy lithium-ion batteries", *Nat. Chem.* **2013**, *5*, 1042.

[19]   Z. Chen, C. Wang, J. Lopez, Z. Lu, Y. Cui, and Z. Bao, "High-areal-capacity silicon electrodes with low-cost silicon particles based on spatial control of self-healing binder", *Adv. Energy Mater.* **2015**, *5*, 1401826.

[20]   A. M. Wilson and J. R. Dahn, "Lithium insertion in carbons containing nanodispersed silicon", *J. Electrochem. Soc.* **1995**, *142*, 326.

[21]   N. Liu, H. Wu, M. T. McDowell, Y. Yao, C. Wang, Y. Cui, *Nano Lett.* **2012**, *12*, 3315.[22]   T. H. Hwang, Y. M. Lee, B.-S. Kong, J.-S. Seo, and J. W. Choi, "Electrospun core–shell fibers for robust silicon nanoparticle-based lithium ion battery anodes" *Nano Lett.* **2012**, *12*, 802.

[23]   Y. Yu, L. Gu, C. Zhu, S. Tsukimoto, P. A. van Aken, and J. Maier, "Reversible Storage of Lithium in Silver-Coated Three-Dimensional Macroporous Silicon", *Adv. Mater.* **2010**, *22*, 2247.

[24]   B. Koo, H. Kim, Y. Cho, K. T. Lee, N.-S. Choi, and J. Cho, "A highly cross-linked polymeric binder for high-performance silicon negative electrodes in lithium ion batteries", *Angew. Chemie Int. Ed.* **2012**, *51*, 8762.

[25]   E. M. Erickson, E. Markevich, G. Salitra, D. Sharon, D. Hirshberg, E. de la Llave, I. Shterenberg, A. Rosenman, A. Frimer, and D. Aurbach, "Development of Advanced Rechargeable Batteries: A Continuous Challenge in the Choice of Suitable Electrolyte Solutions" *J. Electrochem. Soc.* **2015**, *162*, A2424.

[26]   V. Etacheri, R. Marom, R. Elazari, G. Salitra, and D. Aurbach, "Challenges in the development of advanced Li-ion batteries: a review", *Energy Environ. Sci.* **2011**, *4*, 3243.

[27]   E. Markevich, G. Salitra, A. Rosenman, Y. Talyosef, D. Aurbach, and A. Garsuch, "High performance of thick amorphous columnar monolithic film silicon anodes in ionic liquid electrolytes at elevated temperature", *RSC Adv.* **2014**, *4*, 48572.

[28]   E. Rossen, C. D. W. Jones, and J. R. Dahn, "Structure and electrochemistry of $LixMnyNi_{1-y}O_2$" *Solid State Ionics* **1992**, *57*, 311.

[29]   M. H. Rossouw, D. C. Liles, and M. M. Thackeray, "Synthesis and structural characterization of a novel layered lithium manganese oxide, $Li_{0.36}Mn_{0.91}O_2$, and its

lithiated derivative, $Li_{1.09}Mn_{0.91}O_2$", *J. Solid State Chem.* **1993**, *104*, 464.

[30] S. B. Chikkannanavar, D. M. Bernardi, and L. Liu, "A review of blended cathode materials for use in Li-ion batteries", *J. Power Sources* **2014**, *248*, 91.

[31] W. Liu, P. Oh, X. Liu, M.-J. Lee, W. Cho, S. Chae, Y. Kim, and J. Cho, "Nickel-rich layered lithium transition-metal oxide for high-energy lithium-ion batteries", *Angew. Chemie Int. Ed.* **2015**, *54*, 4440.

[32] F. Lin, I. M. Markus, D. Nordlund, T.-C. Weng, M. D. Asta, H. L. Xin, and M. M. Doeff, "Surface reconstruction and chemical evolution of stoichiometric layered cathode materials for lithium-ion batteries", *Nat. Commun.* **2014**, *5*, 3529.

[33] A. Manthiram, J. C. Knight, S.-T. Myung, S.-M. Oh, and Y.-K. Sun, "Nickel-rich and lithium-rich layered oxide cathodes: progress and perspectives", *Adv. Energy Mater.* **2016**, *6*, 1501010.

[34] P. K. Nayak, J. Grinblat, M. Levi, B. Markovsky, and D. Aurbach, "Structural and Electrochemical Evidence of Layered to Spinel Phase Transformation of Li and Mn Rich Layered Cathode Materials of the Formulae $xLi[Li_{1/3}Mn_{2/3}]O_2.(1-x)LiMn_{1/3}Ni_{1/3}Co_{1/3}O_2$ (x = 0.2, 0.4, 0.6) upon Cycling", *J. Electrochem. Soc.* **2014**, *161*, A1534.

[35] O. Haik, N. Leifer, Z. Samuk-Fromovich, E. Zinigrad, B. Markovsky, L. Larush, Y. Goffer, G. Goobes, and D. Aurbach, "On the Surface Chemistry of $LiMO_2$ Cathode Materials (M = [MnNi] and [MnNiCo]): Electrochemical, Spectroscopic, and Calorimetric Studies", *J. Electrochem. Soc.* **2010**, *157*, A1099.

[36] K. C. Kam, A. Mehta, J. T. Heron, and M. M. Doeff, "Electrochemical and Physical Properties of Ti-Substituted Layered Nickel Manganese Cobalt Oxide (NMC) Cathode Materials", *J. Electrochem. Soc.* **2012**, *159*, A1383.

[37] N. K. Karan, M. Balasubramanian, D. P. Abraham, M. M. Furczon, D. K. Pradhan, J. J. Saavedra-Arias, R. Thomas, and R. S. Katiyar, "Structural characteristics and electrochemical performance of layered $Li[Mn_{0.5-x}Cr_{2x}Ni_{0.5-x}]O_2$ cathode materials", *J. Power Sources* **2009**, *187*, 586.

[38] J. Kim and K. Amine, "A comparative study on the substitution of divalent, trivalent and tetravalent metal ions in $LiNi_{1-x}M_xO_2$ (M=Cu^{2+}, Al^{3+} and Ti^{4+})", *J. Power Sources* **2002**, *104*, 33.

[39] H.-B. Kim, B.-C. Park, S.-T. Myung, K. Amine, J. Prakash, and Y.-K. Sun, "Electrochemical and thermal characterization of AlF_3-coated $Li[Ni_{0.8}Co_{0.15}Al_{0.05}]O_2$ cathode in lithium-ion cells", *J. Power Sources* **2008**, *179*, 347.

[40] W. C. West, J. Soler, M. C. Smart, B. V. Ratnakumar, S. Firdosy, V. Ravi, M. S. Anderson, J. Hrbacek, E. S. Lee, and A. Manthiram, "Electrochemical Behavior of Layered Solid Solution $Li_2MnO_3-LiMO_2$ (M = Ni, Mn, Co) Li-Ion Cathodes with and without Alumina Coatings", *J. Electrochem. Soc.* **2011**, *158*, A883.

[41] X. Zhang, I. Belharouak, L. Li, Y. Lei, J. W. Elam, A. Nie, X. Chen, R. S. Yassar, and R. L. Axelbaum, "Structural and Electrochemical Study of Al_2O_3 and TiO_2 Coated $Li_{1.2}Ni_{0.13}Mn_{0.54}Co_{0.13}O_2$ Cathode Material Using ALD", *Adv. Energy Mater.* **2013**, *3*, 1299.

[42]   J. Cho, H. Kim, and B. Park, Comparison of Overcharge Behavior of $AlPO_4$-Coated $LiCoO_2$ and $LiNi_{0.8}Co_{0.1}Mn_{0.1}O_2$ Cathode Materials in Li-Ion Cells *J. Electrochem. Soc.* **2004**, *151*, A1707.

[43]   Y.-K. Sun, Z. Chen, H.-J. Noh, D.-J. Lee, H.-G. Jung, Y. Ren, S. Wang, C. S. Yoon, S.-T. Myung, and K. Amine, "Nanostructured high-energy cathode materials for advanced lithium batteries", *Nat. Mater.* **2012**, *11*, 942.

[44]   B. Saha, K. Goebel, S. Poll, and J. Christophersen, "Prognostics Methods for Battery Health Monitoring Using a Bayesian Framework", *IEEE Trans. Instrum. Meas.* **2009**, *58*, 291.

[45]   W. He, N. Williard, M. Osterman, and M. Pecht, "Prognostics of lithium-ion batteries based on Dempster–Shafer theory and the Bayesian Monte Carlo method", *J. Power Sources* **2011**, *196*, 10314.

[46]   L. Zhang, L. Wang, C. Lyu, J. Li, and J. Zheng, "Non-destructive analysis of degradation mechanisms in cycle-aged graphite/$LiCoO2$ batteries", *Energies*, **2014**, *7*, 6282.

[47]   B. Stiaszny, J. C. Ziegler, E. E. Krauß, J. P. Schmidt, and E. Ivers-Tiffée, "Electrochemical characterization and post-mortem analysis of aged $LiMn_2O_4$–Li ($Ni_{0.5}Mn_{0.3}Co_{0.2}$)O_2/graphite lithium ion batteries. Part I: Cycle aging", *J. Power Sources* **2014**, *251*, 439.

[48]   M. Bauer, C. Guenther, M. Kasper, M. Petzl, and M. A. Danzer, "Discrimination of degradation processes in lithium-ion cells based on the sensitivity of aging indicators towards capacity loss", *J. Power Sources* **2015**, *283*, 494.

[49]   M. J. Brand, S. F. Schuster, T. Bach, E. Fleder, M. Stelz, S. Gläser, J. Müller, G. Sextl, and A. Jossen, "Effects of vibrations and shocks on lithium-ion cells", *J. Power Sources* **2015**, *288*, 62.

[50]   H. Wu, D. Zhuo, D. Kong, and Y. Cui, "Improving battery safety by early detection of internal shorting with a bifunctional separator", *Nat. Commun.* **2014**, *5*, 5193.

[51]   J. Steiger, D. Kramer, and R. Mönig, "Mechanisms of dendritic growth investigated by in situ light microscopy during electrodeposition and dissolution of lithium", *J. Power Sources* **2014**, *261*, 112.

[52]   C. Uhlmann, J. Illig, M. Ender, R. Schuster, and E. Ivers-Tiffée, "In situ detection of lithium metal plating on graphite in experimental cells", *J. Power Sources* **2015**, *279*, 428.

[53]   S. J. Harris, A. Timmons, D. R. Baker, and C. Monroe, "Direct in situ measurements of Li transport in Li-ion battery negative electrodes", *Chem. Phys. Lett.* **2010**, *485*, 265.

[54]   M. Pfanzelt, P. Kubiak, M. Fleischhammer, and M. Wohlfahrt-Mehrens, "TiO_2 rutile—An alternative anode material for safe lithium-ion batteries", *J. Power Sources* **2011**, *196*, 6815.

[55]   M. Pharr, Z. Suo, and J. J. Vlassak, "Measurements of the fracture energy of lithiated silicon electrodes of Li-ion batteries", *Nano Lett.* **2013**, *13*, 5570.

[56] Y. Li, and P. S. Fedkiw, "Effect of gel electrolytes containing silica nanoparticles on aluminum corrosion", *Electrochim. Acta* **2007**, *52*, 2471.

[57] T. Waldmann, M. Wilka, M. Kasper, M. Fleischhammer, and M. Wohlfahrt-Mehrens, "Temperature dependent ageing mechanisms in Lithium-ion batteries–A Post-Mortem study", *J. Power Sources* **2014**, *262*, 129.

[58] J. C. Burns, A. Kassam, N. N. Sinha, L. E. Downie, L. Solnickova, B. M. Way, and J. R. Dahn, "Predicting and Extending the Lifetime of Li-Ion Batteries", *J. Electrochem. Soc.* **2013**, *160*, A1451.

[59] T. Waldmann, N. Ghanbari, M. Kasper, and M. Wohlfahrt-Mehrens, "Correlations between Electrochemical Data and Results from Post-Mortem Analysis of Aged Lithium-Ion Batteries" *J. Electrochem. Soc.* **2015**, *162*, A1500.

[60] M. Broussely, S. Herreyre, P. Biensan, P. Kasztejna, K. Nechev, and R. . Staniewicz, "Aging mechanism in Li ion cells and calendar life predictions", *J. Power Sources* **2001**, *97–98*, 13.

[61] H. Honbo, K. Takei, Y. Ishii, and T. Nishida, "Electrochemical properties and Li deposition morphologies of surface modified graphite after grinding", *J. Power Sources* **2009**, *189*, 337.

[62] M. Zier, F. Scheiba, S. Oswald, J. Thomas, D. Goers, T. Scherer, M. Klose, H. Ehrenberg, and J. Eckert, "Lithium dendrite and solid electrolyte interphase investigation using OsO_4", *J. Power Sources* **2014**, *266*, 198.

[63] P. Svens, R. Eriksson, J. Hansson, M. Behm, and T. Gustafsson, G. Lindbergh, "Analysis of aging of commercial composite metal oxide–$Li_4Ti_5O_{12}$ battery cells", *J. Power Sources* **2014**, *270*, 131.

[64] M. Zhu, J. Park, and A. M. Sastry, "Fracture Analysis of the Cathode in Li-Ion Batteries: A Simulation Study", *J. Electrochem. Soc.* **2012**, *159*, A492.

[65] W. H. Woodford, Y.-M. Chiang, and W. C. Carter, ""Electrochemical Shock" of Intercalation Electrodes: A Fracture Mechanics Analysis", *J. Electrochem. Soc.* **2010**, *157*, A1052.

[66] X. Zhang, B. Winget, M. Doeff, J. W. Evans, and T. M. Devine, "Corrosion of Aluminum Current Collectors in Lithium-Ion Batteries with Electrolytes Containing $LiPF_6$", *J. Electrochem. Soc.* **2005**, *152*, B448.

[67] E. Cho, J. Mun, O. B. Chae, O. M. Kwon, H.-T. Kim, J. H. Ryu, Y. G. Kim, and S. M. Oh, "Corrosion/passivation of aluminum current collector in bis (fluorosulfonyl) imide-based ionic liquid for lithium-ion batteries", *Electrochem. commun.* **2012**, *22*, 1.

[68] C. Peabody and C. B. Arnold, "The role of mechanically induced separator creep in lithium-ion battery capacity fade", *J. Power Sources* **2011**, *196*, 8147.

[69] E. Sarasketa-Zabala, F. Aguesse, I. Villarreal, L. M. Rodriguez-Martinez, C. M. López, and P. Kubiak, "Understanding lithium inventory loss and sudden performance fade in cylindrical cells during cycling with deep-discharge steps", *J. Phys. Chem. C* **2015**, *119*, 896.

[70] L. Gu, D. Xiao, Y.-S. Hu, H. Li, and Y. Ikuhara, "Atomic-Scale Structure Evolution in a Quasi-Equilibrated Electrochemical Process of Electrode Materials for Rechargeable Batteries", *Adv. Mater.* **2015**, *27*, 2134.

[71] S. Watanabe, M. Kinoshita, and K. Nakura, "Capacity fade of LiNi(1−x−y)CoxAlyO2 cathode for lithium-ion batteries during accelerated calendar and cycle life test. I. Comparison analysis between $LiNi_{(1-x-y)}Co_xAl_yO_2$ and $LiCoO_2$ cathodes in cylindrical lithium-ion cells during long term storage test", *J. Power Sources* **2014**, *247*, 412.

[72] J. Nelson Weker, and M. F. Toney, "Emerging In Situ and Operando Nanoscale X-Ray Imaging Techniques for Energy Storage Materials", *Adv. Funct. Mater.* **2015**, *25*, 1622.

[73] M. Klett, R. Eriksson, J. Groot, P. Svens, K. Ciosek Högström, R. W. Lindström, H. Berg, T. Gustafson, G. Lindbergh, and K. Edström, "Non-uniform aging of cycled commercial LiFePO4//graphite cylindrical cells revealed by post-mortem analysis", *J. Power Sources* **2014**, *257*, 126.

[74] S. F. Schuster, M. J. Brand, C. Campestrini, and M. Gleissenberger, A. Jossen, "Correlation between capacity and impedance of lithium-ion cells during calendar and cycle life", *J. Power Sources* **2016**, *305*, 191.

[75] Y. Krämer, C. Birkenmaier, J. Feinauer, A. Hintennach, C. L. Bender, M. Meiler, V. Schmidt, R. E. Dinnebier, and T. Schleid, "A New Method for Quantitative Marking of Deposited Lithium by Chemical Treatment on Graphite Anodes in Lithium-Ion Cells", *Chem. - A Eur. J.* **2015**, *21*, 6062.

[76] H. Maleki and J. N. Howard, "Effects of overdischarge on performance and thermal stability of a Li-ion cell", *J. Power Sources* **2006**, *160*, 1395.

[77] P. N. Ross, "Catalysis and Interfacial Chemistry in Lithium Batteries: A Surface Science Approach", *Catal. Letters* **2014**, *144*, 1370.

[78] M. Lu, H. Cheng, and Y. Yang, "A comparison of solid electrolyte interphase (SEI) on the artificial graphite anode of the aged and cycled commercial lithium ion cells", *Electrochim. Acta* **2008**, *53*, 3539.

[79] F. German, A. Hintennach, A. Lacroix, D. Thiemig, S. Oswald, F. Scheiba, M. J. Hoffmann, and H. Ehrenberg, "Influence of temperature and upper cut-off voltage on the formation of lithium-ion cells", *J. Power Sources* **2014**, *264*, 100.

[80] Y. Zheng, Y.-B. He, K. Qian, B. Li, X. Wang, J. Li, C. Miao, and F. Kang, "Effects of state of charge on the degradation of LiFePO4/graphite batteries during accelerated storage test", *J. Alloys Compd.* **2015**, *639*, 406.

[81] X. Feng, M.-K. Song, W. C. Stolte, D. Gardenghi, D. Zhang, X. Sun, J. Zhu, E. J. Cairns, and J. Guo, "Understanding the degradation mechanism of rechargeable lithium/sulfur cells: a comprehensive study of the sulfur–graphene oxide cathode after discharge–charge cycling", *Phys. Chem. Chem. Phys.* **2014**, *16*, 16931.

[82] M. C. Smart, B. L. Lucht, S. Dalavi, F. C. Krause, and B. V. Ratnakumar, "The Effect of Additives upon the Performance of MCMB/LiNixCo1−xO2 Li-Ion Cells Containing Methyl Butyrate-Based Wide Operating Temperature Range Electrolytes", *J.*

Electrochem. Soc. **2012**, *159*, A739.

[83] G. Chen, G. V. Zhuang, T. J. Richardson, G. Liu, and P. N. Ross, "Anodic polymerization of vinyl ethylene carbonate in Li-Ion battery electrolyte", *Electrochem. Solid-State Lett.* **2005**, *8*, A344.

[84] G. G. Eshetu, S. Grugeon, G. Gachot, D. Mathiron, M. Armand, and S. Laruelle, "LiFSI vs. LiPF$_6$ electrolytes in contact with lithiated graphite: Comparing thermal stabilities and identification of specific SEI-reinforcing additives", *Electrochim. Acta* **2013**, *102*, 133.

[85] N. S. Norberg, S. F. Lux, and R. Kostecki, "Interfacial side-reactions at a LiNi$_{0.5}$Mn$_{1.5}$O$_4$ electrode in organic carbonate-based electrolytes", *Electrochem. commun.* **2013**, *34*, 29.

[86] M. Wohlfahrt-Mehrens, C. Vogler, and J. Garche, "Aging mechanisms of lithium cathode materials", *J. Power Sources* **2004**, *127*, 58.

[87] J. Vetter, P. Novák, M. R. Wagner, C. Veit, K.-C. Möller, J. O. Besenhard, M. Winter, M. Wohlfahrt-Mehrens, C. Vogler, A. Hammouche, "Ageing mechanisms in lithium-ion batteries", *J. Power Sources* **2005**, *147*, 269.

[88] C. P. Grey and Y. J. Lee, "Lithium MAS NMR studies of cathode materials for lithium-ion batteries", *Solid State Sci.* **2003**, *5*, 883.

[89] M. Wagemaker, R. van de Krol, A. P. M. Kentgens, A A. van Well, and F. M. Mulder, "Two Phase Morphology Limits Lithium Diffusion in TiO2 (Anatase): A ^{7}Li MAS NMR Study", *J. Am. Chem. Soc.*, **2001**, 123, 11454.

[90] C. P. Grey and N. Dupré, "NMR Studies of Cathode Materials for Lithium-Ion Rechargeable Batteries", *Chem. Rev.* **2004**, 101, 4493.

[91] N. Delpuech, N. Dupré, D. Mazouzi, J. Gaubicher, P. Moreau, J. S. Bridel, D. Guyomard, and B. Lestriez, "Correlation between irreversible capacity and electrolyte solvents degradation probed by NMR in Si-based negative electrode of Li-ion cell", *Electrochem. commun.* **2013**, *33*, 72.

[92] B. Key, R. Bhattacharyya, M. Morcrette, V. Seznéc, J.-M. Tarascon, and C. P. Grey, "Real-time NMR investigations of structural changes in silicon electrodes for lithium-ion batteries", *J. Am. Chem. Soc.* **2009**, *131*, 9239.

[93] J. H. S. R. DeSilva, V. Udinwe, P. J. Sideris, M. C. Smart, F. C. Krause, C. Hwang, K. A. Smith, S. G. Greenbaum, "Solid State Multinuclear Magnetic Resonance Investigation of Electrolyte Decomposition Products on Lithium-Ion Electrodes", *ECS Trans.*, **2012**, 41, 207.

[94] J. Self, C. P. Aiken, R. Petibon, J. R. Dahn, "Survey of Gas Expansion in Li-Ion NMC Pouch Cells", *J. Electrochem. Soc.* **2015**, *162*, A796.

[95] T. Sasaki, T. Abe, Y. Iriyama, M. Inaba, and Z. Ogumi, "Formation mechanism of alkyl dicarbonates in Li-ion cells", *J. Power Sources* **2005**, *150*, 208.

[96] L. Gireaud, S. Grugeon, S. Pilard, P. Guenot, and J-M. Tarascon, S. Laruelle, "Mass Spectrometry Investigations on Electrolyte Degradation Products for the

Development of Nanocomposite Electrodes in Lithium Ion Batteries", *Anal. Chem.* **2006**, 78, 3688.

[97] G. Gachot, P. Ribière, D. Mathiron, S. Grugeon, M. Armand, J.-B. Leriche, S. Pilard, and S. Laruelle, "Gas chromatography/mass spectrometry as a suitable tool for the Li-ion battery electrolyte degradation mechanisms study", *Anal. Chem.* **2011**, *83*, 478.

[98] G. Gachot, S. Grugeon, M. Armand, S. Pilard, P. Guenot, J.-M. Tarascon, and S. Laruelle, "Deciphering the multi-step degradation mechanisms of carbonate-based electrolyte in Li batteries", *J. Power Sources* **2008**, *178*, 409.

[99] G. Gachot, S. Grugeon, I. Jimenez-Gordon, G. G. Eshetu, S. Boyanov, A. Lecocq, G. Marlair, S. Pilard, and S. Laruelle, "Gas chromatography/Fourier transform infrared/mass spectrometry coupling: a tool for Li-ion battery safety field investigation", *Anal. Methods* **2014**, *6*, 6120.

[100] T. Waldmann, A. Iturrondobeitia, M. Kasper, N. Ghanbari, F. Aguesse, E. Bekaert, L. Daniel, S. Genies, I. J. Gordon, M. W. Löble, E. De Vito, and M. Wohlfahrt-Mehrens, "Post-Mortem Analysis of Aged Lithium-Ion Batteries: Disassembly Methodology and Physico-Chemical Analysis Techniques", *J. Electrochem. Soc.* **2016**, *163*, 2149.

[101] M. Dubarry, C. Truchot, and B. Y. Liaw, "Synthesize battery degradation modes via a diagnostic and prognostic model", *J. Power Sources* **2012**, *219*, 204.

[102] M. Dubarry, A. Devie, and B. Y. Liaw, "The Value of Battery Diagnostics and Prognostics", *J. Energy Power Sources*, **2014**, 5, 242

[103] I. Bloom, L. Trahey, A. Abouimrane, I. Belharouak, X. Zhang, Q. Wu, W. Lu, D. P. Abraham, M. Bettge, J. W. Elam, X. Meng, A. K. Burrell, C. Ban, R. Tenent, J. Nanda, and N. Dudney, "Effect of interface modifications on voltage fade in 0.5 Li_2MnO_3 0.5 $LiNi_{0.375}Mn_{0.375}Co_{0.25}O_2$ cathode materials", *J. Power Sources* **2014**, *249*, 509.

[104] A. H. Thompson, "Electrochemical potential spectroscopy: a new electrochemical measurement", *J. Electrochem. Soc.* **1979**, *126*, 608.

[105] J. R. Dahn, "Phase diagram of Li_xC_6", *Phys. Rev. B* **1991**, *44*, 9170.

[106] T. Ohzuku, Y. Iwakoshi, and K. Sawai, "Formation of lithium-graphite intercalation compounds in nonaqueous electrolytes and their application as a negative electrode for a lithium ion (shuttlecock) cell", *J. Electrochem. Soc.* **1993**, *140*, 2490.

[107] D. Aurbach, B. Markovsky, I. Weissman, E. Levi, and Y. Ein-Eli, "On the correlation between surface chemistry and performance of graphite negative electrodes for Li ion batteries", *Electrochim. Acta* **1999**, *45*, 67.

[108] J. Barker, *Electrochim.*" Three Electrode Electrochemical Voltage Spectroscopy (TEVS): evaluation of a model lithium ion system", *Acta* **1995**, *40*, 1603.

[109] M. Y. Saïdi, J. Barker, and R. Koksbang, "Structural and electrochemical investigation of lithium insertion in the $Li_{1-x}Mn_2O_4$ spinel phase", *Electrochim. Acta* **1996**, *41*, 199.

[110] R. Koksbang, J. Barker, H. Shi, and M. Y. Saïdi, "Cathode materials for lithium rocking chair batteries", *Solid State Ionics* **1996**, *84*, 1.

[111] J. Barker, M. Y. Saidi, and J. L. Swoyer, "Performance evaluation of the electroactive material, gamma-LiV_2O_5, made by a carbothermal reduction method", *J. Electrochem. Soc.* **2003**, *150*, A1267.

[112] K. Striebel, A. Guerfi, J. Shim, M. Armand, M. Gauthier, and K. Zaghib, "$LiFePO_4$/gel/natural graphite cells for the BATT program", *J. Power Sources,* **2003**, *119–121*, 951.

[113] I. Bloom, A. N. Jansen, D. P. Abraham, J. Knuth, S. A. Jones, V. S. Battaglia, and G. L. Henriksen, "Differential voltage analyses of high-power, lithium-ion cells: 1. Technique and application", *J. Power Sources* **2005**, *139*, 295.

[114] M. Dubarry, V. Svoboda, R. Hwu, and B. Yann Liaw, "Incremental capacity analysis and close-to-equilibrium OCV measurements to quantify capacity fade in commercial rechargeable lithium batteries", *Electrochem. Solid-State Lett.* **2006**, *9*, A454.

[115] X. Han, M. Ouyang, L. Lu, J. Li, Y. Zheng, and Z. Li, "A comparative study of commercial lithium ion battery cycle life in electrical vehicle: Aging mechanism identification", *J. Power Sources* **2014**, *251*, 38.

[116] A. Barai, K. Uddin, M. Dubarry, L. Somerville, A. McGordon, P. Jennings, I. Bloom, "A comparison of methodologies for the non-invasive characterisation of commercial Li-ion cells", *Prog. Energy Combust. Sci.* **2019**, *72*, 1.

[117] M. M. Kabir and D. E. Demirocak, "Degradation mechanisms in Li-ion batteries: a state-of-the-art review", *Int. J. Energy Res.* **2017**, *41*, 1963.

[118] M. Dubarry, C. Truchot, M. Cugnet, B. Y. Liaw, K. Gering, S. Sazhin, D. Jamison, and C. Michelbacher, "Evaluation of commercial lithium-ion cells based on composite positive electrode for plug-in hybrid electric vehicle applications. Part I: Initial characterizations", *J. Power Sources* **2011**, *196*, 10328.

[119] C. R. Birkl, M. R. Roberts, E. McTurk, P. G. Bruce, and D. A. Howey, "Degradation diagnostics for lithium ion cells", *J. Power Sources* **2017**, *341*, 373.

[120] M. Kassem, and C. Delacourt, "Postmortem analysis of calendar-aged graphite/$LiFePO_4$ cells", *J. Power Sources* **2013**, *235*, 159.

[121] J. P. Schmidt, H. Y. Tran, J. Richter, E. Ivers-Tiffée, M. Wohlfahrt-Mehrens, "Analysis and prediction of the open circuit potential of lithium-ion cells", *J. Power Sources* **2013**, *239*, 696.

[122] Dai Haifeng, Wei Xuezhe, Sun Zechang, "A new SOH prediction concept for the power lithium-ion battery used on HEVs", in *2009 IEEE Veh. Power Propuls. Conf.*, IEEE, **2009**, 1649.

[123] S. Sepasi, R. Ghorbani, and B. Y. Liaw, "A novel on-board state-of-charge estimation method for aged Li-ion batteries based on model adaptive extended Kalman filter", *J. Power Sources* **2014**, *245*, 337.

[124] Z. Guo, X. Qiu, G. Hou, B. Y. Liaw, and C. Zhang, "State of health estimation for

lithium ion batteries based on charging curves", *J. Power Sources* **2014**, *249*, 457.

[125] M. Doyle, T. F. Fuller, and J. Newman, "Modeling of galvanostatic charge and discharge of the lithium/polymer/insertion cell", *J. Electrochem. Soc.* **1993**, *140*, 1526.

[126] M. Doyle, J. Newman, A. S. Gozdz, C. N. Schmutz, and J. Tarascon, "Comparison of modeling predictions with experimental data from plastic lithium ion cells", *J. Electrochem. Soc.* **1996**, *143*, 1890.

[127] Y. Ye, Y. Shi, and A. A. O. Tay, "Electro-thermal cycle life model for lithium iron phosphate battery", *J. Power Sources* **2012**, *217*, 509.

[128] Q. Zhang and R. E. White, "Calendar life study of Li-ion pouch cells: Part 2: Simulation", *J. Power Sources* **2008**, *179*, 785.

[129] Q. Zhang, and R. E. White, "Capacity fade analysis of a lithium ion cell", *J. Power Sources* **2008**, *179*, 793.

[130] C. Delacourt, and M. Safari, "Life simulation of a graphite/LiFePO$_4$ cell under cycling and storage", *J. Electrochem. Soc.* **2012**, *159*, A1283.

[131] A. P. Schmidt, M. Bitzer, Á. W. Imre, L. Guzzella, "Model-based distinction and quantification of capacity loss and rate capability fade in Li-ion batteries", *J. Power Sources* **2010**, *195*, 7634.

[132] V. Ramadesigan, K. Chen, N. A. Burns, V. Boovaragavan, R. D. Braatz, and V. R. Subramanian, "Parameter estimation and capacity fade analysis of lithium-ion batteries using reformulated models", *J. Electrochem. Soc.* **2011**, *158*, A1048.

[133] R. Fu, S.-Y. Choe, V. Agubra, and J. Fergus, "Modeling of degradation effects considering side reactions for a pouch type Li-ion polymer battery with carbon anode", *J. Power Sources* **2014**, *261*, 120.

[134] S.-K. Jung, H. Gwon, J. Hong, K.-Y. Park, D.-H. Seo, H. Kim, J. Hyun, W. Yang, and K. Kang, "Understanding the Degradation Mechanisms of LiNi0.5Co0.2Mn0.3O2 Cathode Material in Lithium Ion Batteries", *Adv. Energy Mater.* **2014**, *4*, 1300787.

[135] I. Bloom, B. . Cole, J. . Sohn, S. . Jones, E. . Polzin, V. . Battaglia, G. . Henriksen, C. Motloch, R. Richardson, T. Unkelhaeuser, D. Ingersoll, and H. . Case, "An accelerated calendar and cycle life study of Li-ion cells", *J. Power Sources* **2001**, *101*, 238.

[136] J. Wang, P. Liu, J. Hicks-Garner, E. Sherman, S. Soukiazian, M. Verbrugge, H. Tataria, J. Musser, and P. Finamore, "Cycle-life model for graphite-LiFePO4 cells", *J. Power Sources* **2011**, *196*, 3942.

[137] Z. Li, L. Lu, M. Ouyang, and Y. Xiao, "Modeling the capacity degradation of LiFePO4/graphite batteries based on stress coupling analysis", *J. Power Sources* **2011**, *196*, 9757.

[138] M. Safari, M. Morcrette, A. Teyssot, and C. Delacourt, "Life Prediction Methods for Lithium-Ion Batteries Derived from a Fatigue Approach II. Capacity-Loss Prediction

of Batteries Subjected to Complex Current Profiles", *J. Electrochem. Soc.* **2010**, *157*, A892.

[139] V. Klass, M. Behm, G. Lindbergh, "A support vector machine-based state-of-health estimation method for lithium-ion batteries under electric vehicle operation", *J. Power Sources* **2014**, *270*, 262.

[140] J. Guo, Z. Li, and M. Pecht, "A Bayesian approach for Li-Ion battery capacity fade modeling and cycles to failure prognostics", *J. Power Sources* **2015**, *281*, 173.

[141] Datong Liu, Wei Xie, Haitao Liao, and Yu Peng, "An integrated probabilistic approach to lithium-ion battery remaining useful life estimation", *IEEE Trans. Instrum. Meas.* **2015**, *64*, 660.

[142] W. Waag, C. Fleischer, and D. U. Sauer, "Critical review of the methods for monitoring of lithium-ion batteries in electric and hybrid vehicles", *J. Power Sources* **2014**, *258*, 321.

[143] G. L. Plett, "Extended Kalman filtering for battery management systems of LiPB-based HEV battery packs: Part 2. Modeling and identification", *J. Power Sources* **2004**, *134*, 277.

[144] M. Verbrugge, B. Koch, "Generalized recursive algorithm for adaptive multiparameter regression application to lead acid, nickel metal hydride, and lithium-ion batteries", *J. Electrochem. Soc.* **2006**, *153*, A187.

[145] IL-Song Kim, "A technique for estimating the state of health of lithium batteries through a dual-sliding-mode observer", *IEEE Trans. Power Electron.* **2010**, *25*, 1013.

[146] J. Remmlinger, M. Buchholz, M. Meiler, P. Bernreuter, K. Dietmayer, "State-of-health monitoring of lithium-ion batteries in electric vehicles by on-board internal resistance estimation", *J. Power Sources* **2011**, *196*, 5357.

[147] Y. F. Reynier, R. Yazami, B. Fultz, "Thermodynamics of lithium intercalation into graphites and disordered carbons", *J. Electrochem. Soc.* **2004**, *151*, A422.

[148] S. Zhao, S. R. Duncan, and D. A. Howey, "Observability analysis and state estimation of lithium-ion batteries in the presence of sensor biases", *IEEE Trans. Control Syst. Technol.* **2017**, *25*, 326.

[149] A. Jokar, B. Rajabloo, M. Désilets, and M. Lacroix, "Review of simplified Pseudo-two-Dimensional models of lithium-ion batteries", *J. Power Sources* **2016**, *327*, 44.

[150] J. Newman, and W. Tiedemann, "Porous-electrode theory with battery applications", *AIChE J.* **1975**, *21*, 25.

[151] C.-H. Lu, and S.-W. Lin, "Dissolution kinetics of spinel lithium manganate and its relation to capacity fading in lithium ion batteries", *J. Mater. Res.* **2002**, *17*, 1476.

[152] J. Park, J. H. Seo, G. Plett, W. Lu, and A. M. Sastry, "Numerical simulation of the effect of the dissolution of $LiMn_2O_4$ particles on Li-ion battery performance", *Electrochem. Solid-State Lett.* **2011**, *14*, A14.

[153] L. Cai, Y. Dai, M. Nicholson, R. E. White, K. Jagannathan, G. Bhatia, "Life modeling of a lithium ion cell with a spinel-based cathode", *J. Power Sources* **2013**, *221*, 191.

[154] Y. Dai, L. Cai, and R. E. White, Capacity Fade Model for Spinel $LiMn_2O_4$ Electrode *J. Electrochem. Soc.* **2013**, *160*, A182.

[155] P. Ramadass, B. Haran, P. M. Gomadam, R. White, and B. N. Popov, "Development of first principles capacity fade model for Li-ion cells", *J. Electrochem. Soc.* **2004**, *151*, A196.

[156] R. Narayanrao, M. M. Joglekar, and S. Inguva, "A phenomenological degradation model for cyclic aging of lithium ion cell materials", *J. Electrochem. Soc.* **2013**, *160*, A125.

[157] R. Fu, S.-Y. Choe, V. Agubra, and J. Fergus, "Development of a physics-based degradation model for lithium ion polymer batteries considering side reactions", *J. Power Sources* **2015**, *278*, 506.

[158] D. Zhang, B. N. Popov, and R. E. White, "Modeling lithium intercalation of a single spinel particle under potentiodynamic control", *J. Electrochem. Soc.* **2000**, *147*, 831.

[159] R. Spotnitz, "Simulation of capacity fade in lithium-ion batteries", *J. Power Sources* **2003**, *113*, 72.

[160] J. Christensen and J. Newman, "A mathematical model for the lithium-ion negative electrode solid electrolyte interphase", *J. Electrochem. Soc.* **2004**, *151*, A1977.

[161] M. Safari, M. Morcrette, A. Teyssot, and C. Delacourt, "Multimodal physics-based aging model for life prediction of Li-ion batteries", *J. Electrochem. Soc.* **2009**, *156*, A145.

[162] M. B. Pinson, and M. Z. Bazant, "Theory of SEI formation in rechargeable batteries: capacity fade, accelerated aging and lifetime prediction", *J. Electrochem. Soc.* **2013**, *160*, A243.

[163] I. Laresgoiti, S. Käbitz, M. Ecker, and D. U. Sauer, "Modeling mechanical degradation in lithium ion batteries during cycling: Solid electrolyte interphase fracture", *J. Power Sources* **2015**, *300*, 112.

[164] E. Prada, D. Di Domenico, Y. Creff, J. Bernard, V. Sauvant-Moynot, and F. Huet, "A simplified electrochemical and thermal aging model of $LiFePO_4$-graphite Li-ion batteries: power and capacity fade simulations", *J. Electrochem. Soc.* **2013**, *160*, 616.

[165] G. K. Prasad, and C. D. Rahn, "Model based identification of aging parameters in lithium ion batteries", *J. Power Sources* **2013**, *232*, 79.

[166] S. Santhanagopalan, Q. Guo, and R. E. White, "Parameter estimation and model discrimination for a lithium-ion cell", *J. Electrochem. Soc.* **2007**, *154*, A198.

[167] X. Hu, S. Li, and H. Peng, "A comparative study of equivalent circuit models for Li-ion batteries", *J. Power Sources* **2012**, *198*, 359.

[168] C. Y. Wang, W. B. Gu, and B. Y. Liaw, "Micro-macroscopic coupled Modeling of batteries and fuel cells I. Model Development", *J. Electrochem. Soc.* **1998**, *145*, 3407.

[169] V. R. Subramanian, J. A. Ritter, and R. E. White, "Approximate solutions for galvanostatic discharge of spherical particles i. constant diffusion coefficient", *J. Electrochem. Soc.* **2001**, *148*, E444.

[170] V. R. Subramanian, V. D. Diwakar, and D. Tapriyal, "Efficient macro-micro scale coupled modeling of batteries", *J. Electrochem. Soc.* **2005**, *152*, A2002.

[171] L. Cai, and R. E. White, "Reduction of model order based on proper orthogonal decomposition for lithium-ion battery simulations", *J. Electrochem. Soc.* **2009**, *156*, A154.

[172] X. Li, S.-Y. Choe, W. T. Joe, "A reduced order electrochemical and thermal model for a pouch type lithium ion polymer battery with $LiNixMnyCo_{1-x-y}O_2$/LiFePO_4 blended cathode", *J. Power Sources* **2015**, *294*, 545.

[173] V. Ramadesigan, V. Boovaragavan, J. Carl Pirkle, and V. R. Subramanian "Efficient Reformulation of Solid-Phase Diffusion in Physics-Based Lithium-Ion Battery Models", *J. Electrochem. Soc.* **2010**, *157*, A854.

[174] W. Luo, C. Lyu, L. Wang, and L. Zhang, "A new extension of physics-based single particle model for higher charge–discharge rates", *J. Power Sources* **2013**, *241*, 295.

[175] J. Marcicki, M. Canova, A. T. Conlisk, and G. Rizzoni, "Design and parametrization analysis of a reduced-order electrochemical model of graphite/LiFePO4 cells for SOC/SOH estimation", *J. Power Sources* **2013**, *237*, 310.

[176] M.-H. Ryou, G.-B. Han, Y. M. Lee, J.-N. Lee, D. J. Lee, Y. O. Yoon, J.-K. Park, "Effect of fluoroethylene carbonate on high temperature capacity retention of LiMn2O4/graphite Li-ion cells", *Electrochim. Acta* **2010**, *55*, 2073.

[177] Z. Liu, K. Han, Y. K. Chen-Wiegart, J. Wang, H. H. Kung, J. Wang, S. A. Barnett, and K. T. Faber, "X-ray nanotomography analysis of the microstructural evolution of LiMn2O4 electrodes", *J. Power Sources* **2017**, *360*, 460.

[178] E. Wang, D. Ofer, W. Bowden, N. Iltchev, R. Moses, and K. Brandt, "Stability of lithium ion spinel cells. III. Improved life of charged cells", *J. Electrochem. Soc.* **2000**, *147*, 4023.

[179] H. Tsunekawa, S. Tanimoto,a, R. Marubayashi, M. Fujita, K. Kifune, and M. Sano, "Capacity fading of graphite electrodes due to the deposition of manganese ions on them in Li-ion batteries", *J. Electrochem. Soc.* **2002**, *149*, A1326.

[180] Y. Xia, Y. Zhou, M. Yoshio, "Capacity fading on cycling of 4 V Li/LiMn_2O_4 Cells", *J. Electrochem. Soc.* **1997**, *144*, 2593.

[181] P. Arorat, R. E. White, and M. Doyle, "Capacity Fade Mechanisms and Side Reactions in Lithium-Ion Batteries", *J. Electrochem. Soc.* **1998**, *145*, 3647.

[182] C. Zhan, J. Lu, A. Jeremy Kropf, T. Wu, A. N. Jansen, Y.-K. Sun, X. Qiu, K. Amine, "Mn (II) deposition on anodes and its effects on capacity fade in spinel lithium manganate–carbon systems", *Nat. Commun.* **2013**, *4*, 2437.

[183] A. Manthiram, K. Chemelewski, E.-S. Lee, "A perspective on the high-voltage LiMn1.5Ni0.5O4 spinel cathode for lithium-ion batteries", *Energy Environ. Sci.* **2014**, *7*, 1339.

[184] L. L. Lam, R. B. Darling, "Determining the optimal discharge strategy for a lithium-ion battery using a physics-based model", *J. Power Sources* **2015**, *276*, 195.

[185] W. A. Appiah, M.-H. Ryou, and Y. M. Lee, "A Physics-Based Model Capacity Fade Analysis of LiMn2O4/Graphite Cell at Different Temperatures", *J. Electrochem. Soc.* **2019**, *166*, 5109.

[186] M. Jeong, M.-J. Lee, J. Cho, and S. Lee, "Surface Mn Oxidation State Controlled Spinel $LiMn_2O_4$ as a Cathode Material for High-Energy Li-Ion Batteries", *Adv. Energy Mater.* **2015**, *5*, 1500440.

[187] M.-J. Lee, S. Lee, P. Oh, Y. Kim, and J. Cho, "High Performance $LiMn_2O_4$ Cathode Materials Grown with Epitaxial Layered Nanostructure for Li-Ion Batteries", *Nano Lett.* **2014**, *14*, 993.

[188] S. J. An, J. Li, C. Daniel, D. Mohanty, S. Nagpure, and D. L. Wood, "The state of understanding of the lithium-ion-battery graphite solid electrolyte interphase (SEI) and its relationship to formation cycling", *Carbon.* **2016**, *105*, 52.

[189] V. A. Agubra, and J. W. Fergus, "The formation and stability of the solid electrolyte interface on the graphite anode", *J. Power Sources* **2014**, *268*, 153.

[190] D. H. Jang, Y. J. Shin, and S. M. Oh, "Dissolution of spinel oxides and capacity losses in 4 V $Li/Li_xMn_2O_4$ cells", *J. Electrochem. Soc.* **1996**, *143*, 2204.

[191] W. A. Appiah, J. Park, L. Van Khue, Y. Lee, J. Choi, M.-H. Ryou, and Y. M. Lee, "Comparative study on experiments and simulation of blended cathode active materials for lithium ion batteries", *Electrochim. Acta* **2016**, *187*, 422.

[192] W. A. Appiah, J. Park, S. Byun, M.-H. Ryou, and Y. M. Lee, "A mathematical model for cyclic aging of spinel $LiMn_2O_4$/graphite lithium-ion cells", *J. Electrochem. Soc.* **2016**, *163*, 2757.

[193] G. Sikha, B. N. Popov, R. E. White, "Effect of porosity on the capacity fade of a lithium-ion battery theory", *J. Electrochem. Soc.* **2004**, *151*, A1104.

[194] T. Eriksson, A. M. Andersson, C Gejke, and T. Gustafsson, and J. O. Thomas, "Influence of Temperature on the Interface Chemistry of $Li_xMn_2O_4$ Electrodes", *Langmuir* **2002**, 18, 3609

[195] A. Du Pasquier, A. Blyr, P. Courjal, D. Larcher, G. Amatucci, B. Gérand, J. Tarascon, "Mechanism for Limited 55 C Storage Performance of $Li_{1.05}Mn_{1.95}O_4$ Electrodes", *J. Electrochem. Soc.* **1999**, *146*, 428.

[196] S. Sankarasubramanian, B. Krishnamurthy, "A capacity fade model for lithium-ion batteries including diffusion and kinetics", *Electrochim. Acta* **2012**, *70*, 248.

[197] S. Ramesh, and B. Krishnamurthy, "A mathematical model to study capacity fading in lithium ion batteries: formation and dissolution reactions", *J. Electrochem. Soc.* **2015**, *162*, A545.

[198] D. Zhang, B. N. Popov, and R. E. White, "Electrochemical investigation of $CrO_{2.65}$ doped $LiMn_2O_4$ as a cathode material for lithium-ion batteries", *J. Power Sources* **1998**, *76*, 81.

[199] S. R. Das, S. B. Majumder, and R. S. Katiyar, "Kinetic analysis of the Li^+ ion intercalation behavior of solution derived nano-crystalline lithium manganate thin

films", *J. Power Sources* **2005**, *139*, 261.

[200] S. Komaba, N. Kumagai, Y. Kataoka, "Influence of manganese (II), cobalt (II), and nickel (II) additives in electrolyte on performance of graphite anode for lithium-ion batteries", *Electrochim. Acta* **2002**, *47*, 1229.

[201] J. Lei, L. Li, R. Kostecki, R. Muller, and F. McLarnon, "Characterization of SEI layers on $LiMn_2O_4$ cathodes with in situ spectroscopic ellipsometry", *J. Electrochem. Soc.* **2005**, *152*, A774.

[202] R. Fong, U. von Sacken, and J. R. Dahn, "Studies of lithium intercalation into carbons using nonaqueous electrochemical cells", *J. Electrochem. Soc.* **1990**, *137*, 2009.

[203] L.-F. Wang, C.-C. Ou, K. A. Striebel, and J.-S. Chen, "Study of Mn Dissolution from $LiMn_2O_4$ Spinel Electrodes Using Rotating Ring-Disk Collection Experiments", *J. Electrochem. Soc.* **2003**, *150*, A905.

[204] G. Ning, B. Haran, and B. N. Popov, "Capacity fade study of lithium-ion batteries cycled at high discharge rates", *J. Power Sources* **2003**, *117*, 160.

[205] T. Guan, S. Sun, Y. Gao, C. Du, P. Zuo, Y. Cui, L. Zhang, G. Yin, "The effect of elevated temperature on the accelerated aging of $LiCoO_2$/mesocarbon microbeads batteries", *Appl. Energy* **2016**, *177*, 1.

[206] K. Jalkanen, J. Karppinen, L. Skogström, T. Laurila, M. Nisula, and K. Vuorilehto, "Cycle aging of commercial NMC/graphite pouch cells at different temperatures", *Appl. Energy* **2015**, *154*, 160.

[207] S. Saxena, C. Hendricks, and M. Pecht, "Cycle life testing and modeling of graphite/$LiCoO_2$ cells under different state of charge ranges", *J. Power Sources* **2016**, *327*, 394.

[208] C. Liu, and L. Liu, "Optimal design of Li-ion batteries through multi-physics modeling and multi-objective optimization", *J. Electrochem. Soc.* **2017**, *164*, E3254.

[209] K.-C. Chiu, C.-H. Lin, S.-F. Yeh, Y.-H. Lin, C.-S. Huang, and K.-C. Chen, "Cycle life analysis of series connected lithium-ion batteries with temperature difference", *J. Power Sources* **2014**, *263*, 75.

[210] F. Leng, C. M. Tan, and M. Pecht, "Effect of temperature on the aging rate of Li ion battery operating above room temperature", *Sci. Rep.* **2015**, *5*, 12967.

[211] W. A. Appiah, J. Park, S. Byun, Y. Roh, M. Ryou, and Y. M. Lee, "Time-Effective Accelerated Cyclic Aging Analysis of Lithium-Ion Batteries", *ChemElectroChem* **2019**, *6*, 3714.

[212] M.-H. Ryou, G.-B. Han, Y. M. Lee, J.-N. Lee, D. J. Lee, Y. O. Yoon, and J.-K. Park, Effect of fluoroethylene carbonate on high temperature capacity retention of $LiMn_2O_4$/graphite Li-ion cells *Electrochim. Acta* **2010**, *55*, 2073.

[213] M. Ko, S. Chae, J. Ma, N. Kim, H.-W. Lee, Y. Cui, and J. Cho, "Scalable synthesis of silicon-nanolayer-embedded graphite for high-energy lithium-ion batteries", *Nat. Energy* **2016**, *1*, 16113.

[214] M. T. McDowell, S. W. Lee, W. D. Nix, and Y. Cui, "Studying the kinetics of

crystalline silicon nanoparticle lithiation with in situ transmission electron microscopy", *Adv. Mater.* **2013**, *25*, 4966.

[215] C. K. Chan, H. Peng, G. Liu, K. McIlwrath, X. F. Zhang, R. A. Huggins, and Y. Cui, "High-performance lithium battery anodes using silicon nanowires", *Nat. Nanotechnol.* **2008**, *3*, 31.

[216] J. B. Bates, N. J. Dudney, B. Neudecker, A. Ueda, and C. D. Evans, "Thin-film lithium and lithium-ion batteries", *Solid State Ionics* **2000**, *135*, 33.

[217] Y. Son, J. Sung, Y. Son, and J. Cho, "Recent progress of analysis techniques for silicon-based anode of lithium-ion batteries", *Curr. Opin. Electrochem.* **2017**, *6*, 77.

[218] I. Cho, S. Gong, D. Song, Y. G. Lee, M. H. Ryou, Y. M. Lee, "Mussel-inspired Polydopamine-treated Copper Foil as a Current Collector for High-performance Silicon Anodes", *Sci. Rep.* **2016**, *6*, 30945.

[219] W. A. Appiah, D. Kim, J. Song, M. Ryou, Y. M. Lee, "Understanding the Effect of Polydopamine Interlayer onthe Long-Term Cycling Performance of Silicon Anodes: AMultiphysics-Based Model Study", *Batter. Supercaps* **2019**, *2*, 541.

[220] M. H. Ryou, Y. M. Lee, J. K. Park, and J. W. Choi, "Mussel-inspired polydopamine-treated polyethylene separators for high-power Li-ion batteries", *Adv. Mater.* **2011**, *23*, 3066.

[221] D. Mazouzi, N. Delpuech, Y. Oumellal, M. Gauthier, M. Cerbelaud, J. Gaubicher, N. Dupré, P. Moreau, D. Guyomard, L. Roué, and B. Lestriez, "New insights into the silicon-based electrode's irreversibility along cycle life through simple gravimetric method", *J. Power Sources* **2012**, *220*, 180.

[222] W. A. Appiah, J. Park, S. Song, S. Byun, M. H. Ryou, and Y. M. Lee, "Design optimization of LiNi$_{0.6}$Co$_{0.2}$Mn$_{0.2}$O$_2$/graphite lithium-ion cells based on simulation and experimental data", *J. Power Sources* **2016**, *319*, 147.

[223] C. C. Nguyen, S.-W. Song, "Interfacial structural stabilization on amorphous silicon anode for improved cycling performance in lithium-ion batteries", *Electrochim. Acta,* **2010**, *55*, 3026.

[224] M. Winter, "The solid electrolyte interphase–the most important and the least understood solid electrolyte in rechargeable Li batteries", *Zeitschrift für Phys. Chemie* **2009**, *223*, 1395.

[225] N. Delpuech, N. Dupre, P. Moreau, J. Bridel, J. Gaubicher, B. Lestriez, and D. Guyomard, "Mechanism of Silicon Electrode Aging upon Cycling in Full Lithium-Ion Batteries", *ChemSusChem* **2016**, *9*, 841.

[226] Y. Oumellal, N. Delpuech, D. Mazouzi, N. Dupre, J. Gaubicher, P. Moreau, P. Soudan, B. Lestriez, and D. Guyomard, "The failure mechanism of nano-sized Si-based negative electrodes for lithium ion batteries", *J. Mater. Chem.* **2011**, *21*, 6201.

[227] F. Shi, P. N. Ross, G. A. Somorjai, and K. Komvopoulos, "The Chemistry of Electrolyte Reduction on Silicon Electrodes Revealed by in Situ ATR-FTIR Spectroscopy", *J. Phys. Chem. C* **2017**, *121*, 14476.

[228] N. Dupré, P. Moreau, E. De Vito, L. Quazuguel, M. Boniface, A. Bordes, C. Rudisch, P. Bayle-Guillemaud, and D. Guyomard, "Multiprobe study of the solid electrolyte interphase on silicon-based electrodes in full-cell configuration", *Chem. Mater.* **2016**, *28*, 2557.

[229] M. Nie, D. P. Abraham, Y. Chen, A. Bose, and B. L. Lucht, "Silicon solid electrolyte interphase (SEI) of lithium ion battery characterized by microscopy and spectroscopy", *J. Phys. Chem. C* **2013**, *117*, 13403.

[230] L. Baggetto, R. A. H. Niessen, and P. H. L. Notten, "On the activation and charge transfer kinetics of evaporated silicon electrode/electrolyte interfaces", *Electrochim. Acta* **2009**, *54*, 5937.

[231] C.-T. Chen, F. J. Martin-Martinez, G. S. Jung, and M. J. Buehler, "Polydopamine and eumelanin molecular structures investigated with ab initio calculations", *Chem. Sci.* **2017**, *8*, 1631.

[232] R. A. Zangmeister, T. A. Morris, M. J. Tarlov, "Characterization of Polydopamine Thin Films Deposited at Short Times by Autoxidation of Dopamine", *Langmuir*, **2013**, *29*, 8619.

[233] Y. Xie, and C. Yuan, "An integrated anode stress model for commercial Li_xC_6-$Li_yMn_2O_4$ battery during the cycling operation", *J. Power Sources* **2015**, *274*, 101.

[234] J. Li, K. Adewuyi, N. Lotfi, R. G. Landers, and J. Park, "A single particle model with chemical/mechanical degradation physics for lithium ion battery State of Health (SOH) estimation", *Appl. Energy* **2018**, *212*, 1178.

[235] M. Wang, X. Xiao, and X. Huang, "Study of lithium diffusivity in amorphous silicon via finite element analysis", *J. Power Sources* **2016**, *307*, 77.

[236] M. Wang, and X. Xiao, "Investigation of the chemo-mechanical coupling in lithiation/delithiation of amorphous Si through simulations of Si thin films and Si nanospheres", *J. Power Sources* **2016**, *326*, 365.

[237] H. Yang, F. Fan, W. Liang, X. Guo, T. Zhu, and S. Zhang, "A chemo-mechanical model of lithiation in silicon", *J. Mech. Phys. Solids* **2014**, *70*, 349.

[238] M. Wang, X. Xiao, and X. Huang, "A multiphysics microstructure-resolved model for silicon anode lithium-ion batteries", *J. Power Sources* **2017**, *348*, 66.

[239] T. Yoon, C. Nguyen, D. M. Seo, and B. L. Lucht, "Capacity fading mechanisms of silicon nanoparticle negative electrodes for lithium ion batteries", *J. Electrochem. Soc.* **2015**, *162*, 2325.

[240] C. K. Chan, R. Ruffo, S. S. Hong, and Y. Cui, "Surface chemistry and morphology of the solid electrolyte interphase on silicon nanowire lithium-ion battery anodes", *J. Power Sources* **2009**, *189*, 1132.

[241] M. G. Cooper, B. B. Mikic, and M. M. Yovanovich, "Thermal contact conductance", *Int. J. Heat Mass Transf.* **1969**, *12*, 279.

[242] G. Zavarise, P. Wriggers, E. Stein, and B. A. Schrefler, "Real contact mechanisms and finite element formulation—a coupled thermomechanical approach", *Int. J.*

Numer. Methods Eng. **1992**, *35*, 767.

[243] C. Weißenfels, and P. Wriggers, "Numerical modeling of electrical contacts", *Comput. Mech.* **2010**, *46*, 301.

[244] R. Holm, E. Holm, "Electric contact theory and application", *Electric Contacts : Theory and Application*, Springer-Verlag, **1967**.

[245] U. D. Schwarz, "A generalized analytical model for the elastic deformation of an adhesive contact between a sphere and a flat surface", *J. Colloid Interface Sci.* **2003**, *261*, 99.

[246] K. L. Johnson, K. Kendall, A. D. Roberts, "Surface energy and the contact of elastic solids", in *Proc. R. Soc. London A Math. Phys. Eng. Sci.*, The Royal Society, **1971**, *324*, 301.

[247] J. Choi, K. Kim, J. Jeong, K. Y. Cho, M.-H. Ryou, and Y. M. Lee, "Highly adhesive and soluble copolyimide binder: improving the long-term cycle life of silicon anodes in lithium-ion batteries", *ACS Appl. Mater. Interfaces* **2015**, *7*, 14851.

[248] B. Son, M.-H. Ryou, J. Choi, T. Lee, H. K. Yu, J. H. Kim, and Y. M. Lee, "Measurement and analysis of adhesion property of lithium-ion battery electrodes with SAICAS", *ACS Appl. Mater. Interfaces* **2013**, *6*, 526.

[249] Y.-T. Cheng, and M. W. Verbrugge, "Evolution of stress within a spherical insertion electrode particle under potentiostatic and galvanostatic operation", *J. Power Sources* **2009**, *190*, 453.

[250] W. A. Appiah, J. Park, S. Byun, I. Cho, A. Mozer, M.-H. Ryou, and Y. M. Lee, "A coupled chemo-mechanical model to study the effects of adhesive strength on the electrochemical performance of silicon electrodes for advanced lithium ion batteries", *J. Power Sources* **2018**, *407*, 153.

[251] A. J. Bard, L. R. Faulkner, *Electrochemical Methods : Fundamentals and Applications*, Wiley, **2001**, 570.

[252] X. Zhang, W. Shyy, and A. M. Sastry, "Numerical simulation of intercalation-induced stress in Li-ion battery electrode particles", *J. Electrochem. Soc.* **2007**, *154*, A910.

[253] H. S. Carslaw, J. C. Jaeger, *Conduction of Heat in Solids*, Clarendon Press, Oxford, **1959**, 250

[254] J. Shim, and K. A. Striebel, "The dependence of natural graphite anode performance on electrode density", *J. Power Sources* **2004**, *130*, 247.

[255] H. Zheng, L. Tan, G. Liu, X. Song, and V. S. Battaglia, "Calendering effects on the physical and electrochemical properties of Li $[Ni_{1/3}Mn_{1/3}Co_{1/3}]O_2$ cathode", *J. Power Sources* **2012**, *208*, 52.

[256] Y. H. Chen, C. W. Wang, X. Zhang, and A. M. Sastry, "Porous cathode optimization for lithium cells: Ionic and electronic conductivity, capacity, and selection of materials", *J. Power Sources* **2010**, *195*, 2851.

[257] C. Fongy, A. C. Gaillot, S. Jouanneau, D. Guyomard, and B. Lestriez, "Ionic vs

Electronic Power Limitations and Analysis of the Fraction of Wired Grains in LiFePO$_4$ Composite Electrodes", *J. Electrochem. Soc.* **2010**, *157*, A885.

[258] J. Choi, B. Son, M.-H. Ryou, S. H. Kim, J. M. Ko, Y. M. Lee, "Effect of LiCoO$_2$ Cathode Density and Thickness on Electrochemical Performance of Lithium-Ion Batteries", *J. Electrochem. Sci. Technol.* **2013**, *4*, 27.

[259] H. Zheng, J. Li, X. Song, G. Liu, and V. S. Battaglia, "A comprehensive understanding of electrode thickness effects on the electrochemical performances of Li-ion battery cathodes", *Electrochim. Acta* **2012**, *71*, 258.

[260] S. Yu, Y. Chung, M. S. Song, J. H. Nam, and W. Il Cho, "Investigation of design parameter effects on high current performance of lithium-ion cells with LiFePO$_4$/graphite electrodes", *J. Appl. Electrochem.* **2012**, *42*, 443.

[261] X. Hua Liu, L. Zhong, S. Huang, S. X. Mao, T. Zhu, J. Yu Huang, "Size-Dependent Fracture of Silicon Nanoparticles During Lithiation", *ACS Nano*, **2012,** 6, 1522.

[262] J. Choi, K. Kim, J. Jeong, K. Y. Cho, M.-H. Ryou, and Y. M. Lee, "Highly adhesive and soluble copolyimide binder: improving the long-term cycle life of silicon anodes in lithium-ion batteries", *ACS Appl. Mater. Interfaces* **2015**, *7*, 14851.

[263] L. Shen, L. Shen, Z. Wang, L. Chen, "In situ thermally cross-linked polyacrylonitrile as binder for high-performance silicon as lithium ion battery anode", *ChemSusChem* **2014**, *7*, 1951.

[264] A. Magasinski, B. Zdyrko, I. Kovalenko, B. Hertzberg, R. Burtovyy, C. F. Huebner, T. F. Fuller, I. Luzinov, and G. Yushin, "Toward Efficient Binders for Li-Ion Battery Si-Based Anodes: Polyacrylic Acid", *ACS Appl. Mater. Interfaces* **2010**, *2*, 3004.

[265] M. T. McDowell, I. Ryu, S. W. Lee, C. Wang, W. D. Nix, and Y. Cui, "Studying the kinetics of crystalline silicon nanoparticle lithiation with in situ transmission electron microscopy", *Adv. Mater.* **2012**, *24*, 6034.

[266] W. Liang, H. Yang, F. Fan, Y. Liu, X. H. Liu, J. Y. Huang, T. Zhu, S. Zhang, "Tough germanium nanoparticles under electrochemical cycling", *ACS Nano* **2013**, *7*, 3427.

[267] S. Zhang, "Chemomechanical modeling of lithiation-induced failure in high-volume-change electrode materials for lithium ion batteries", *NPJ Comput. Mater.* **2017**, *3*, 1.

[268] J. H. Waite, "Mussel power", *Nat. Mater.* **2008**, *7*, 8.

[269] H. Lee, S. M. Dellatore, W. M. Miller, P. B. Messersmith, "Mussel-inspired surface chemistry for multifunctional coatings", *Science.* **2007**, *318*, 426.

[270] P. Arora, M. Doyle, A. S. Gozdz, R. E. White, and J. Newman, "Comparison between computer simulations and experimental data for high-rate discharges of plastic lithium-ion batteries", *J. Power Sources* **2000**, *88*, 219.

[271] J.-S. Bridel, T. Azais, M. Morcrette, J.-M. Tarascon, and D. Larcher, "Key parameters governing the reversibility of Si/carbon/CMC electrodes for Li-ion batteries", *Chem. Mater.* **2009**, *22*, 1229.

[272] C. Zhang, Y. Lv, W.-Z. Qiu, A. He, and Z.-K. Xu, "Polydopamine Coatings with Nanopores for Versatile Molecular Separation", *ACS Appl. Mater. Interfaces,* **2017**,

9, 14437.

[273] A. M. Becka and C. J. Miller "Electrochemistry at .omega.-hydroxy thiol coated electrodes. 3. Voltage independence of the electron tunneling barrier and measurements of redox kinetics at large overpotentials", *J. Phys. Chem.,* **1992,** 96, 2657.

Appendix A

A.1 Model development: SEI formation at cathode

A.1.1 Definition of the Li-ion loss due to SEI formation

The loss of Li ions due to the formation of SEI at both cathode and anode can be defined as

$$x(t) = \frac{\text{amount of lithium ions consumed}}{\text{initial amount of lithium ions available for cycling}}$$

$$= \frac{N_{Li(consumed)}}{N_{Li(initial)}} = \frac{N_{Li(intial)} - N_{Li(t)}}{N_{Li(intial)}}. \qquad [A1]$$

Dividing the numerator and the denominator by volume (V) yields

$$x(t) = \frac{C_{Li(intial)} - C_{Li(t)}}{C_{Li(intial)}}. \qquad [A2]$$

At $t = 0$, the concentration of the solvent at the electrolyte/electrode interface is equal to the bulk electrolyte solvent concentration, $C_{eq(Li)}$, because there is no SEI formed on the electrode surface. Hence, at $z = L(0) = 0, C_{Li(initial)} = C_{eq(Li)}$. Thus, Eq. [A2] becomes

$$x(t) = \frac{C_{eq(Li)} - C_{Li(t)}}{C_{eq(Li)}}. \qquad [A3]$$

From the stoichiometry of the reaction,

$$2C_{eq(Li)} = C_{eq(S)} \qquad \text{and} \qquad 2C_{Li} = C_S. \qquad [A4]$$

Substituting Eq. [A4] into Eq. [A3] gives

$$x(t) = \frac{C_{eq(S)} - C_{S(t)}}{C_{eq(S)}} \,. \tag{A5}$$

A.2 Transport equations

From total mass balance on the solvent component, S, we know that

$$\frac{\partial C_{S,i}}{\partial t} + \frac{\partial J_{z,s,i}}{\partial z} = 0 \qquad\qquad i = p,n \,. \tag{A6}$$

Fick's second law can then be used to describe the transport of the solvent species in the SEI layer as follows:

$$\frac{\partial J_{z,s,i}}{\partial z} = -D_s \frac{\partial^2 C_{S,i}}{\partial z^2} \,, \tag{A7}$$

where D_s is the solvent diffusivity through the SEI layer. This value is assumed constant for both the cathode and anode SEI.

Assuming a uniform concentration of component S over the entire surface, the general material balance of component S at the SEI interface can be written as

$$f_{s,i(in)} - f_{s,i(out)} + r_{s,i}V = \frac{dN_{s,i}}{dt} \,. \tag{A8}$$

Assuming that there is no accumulation of component S at the interfaces and that all of the S component that diffused into the interface undergoes complete reaction,

$$\frac{dN_{s,i}}{dt} = 0 \quad \text{and} \quad f_{s(out)} = 0 \,. \tag{A9}$$

Hence,

$$f_{s,i(in)} = -r_{s,i}V. \tag{A10}$$

From the definition of molar flow rate, the flow of solvent into the interface can be written as

$$f_{s,i(in)} = -V\frac{\partial C_S}{\partial t}. \tag{A11}$$

Hence, for the anode we obtain

$$-r_{s,n} = k_{S,2}C_{s,n} + k'_{S,4}C_{s,n}C_{Mn^{2+}} - k'_{S,3}C_pC_e = \frac{\partial C_{S,n}}{\partial t}. \tag{A12}$$

Eq. [A12] is the expression for the rate of the formation and dissolution of the SEI layer and of the reaction of the deposited Mn with the electrolyte at the anode. From Eq. [A7] and [A12] we obtain

$$D_{S,n}\frac{\partial^2 C_{S,n}}{\partial z^2} = k_{S,2}C_{S,n} + k'_4C_{S,n}C_{Mn^{2+}} - k'_{S,3}C_pC_e. \tag{A13}$$

The concentration of ethylene and Mn(II) ions are assumed to be constant, so we can write $k_{S,3} = k'_{S,3}C_e$ and $k_{S,4} = k'_{S,4}C_e$. At any point in time t,

$$C_{S,n} + C_p = \text{constant} = C_{S,0}. \tag{A14}$$

Hence, equation [A13] can be simplified to

$$D_{S,n}\frac{\partial^2 C_{S,n}}{\partial z^2} = C_{S,n}\left(k_{S,2} + k_{S,3} + k_{S,4}\right) - k_{S,3}C_{S,0}. \tag{A15}$$

The boundary conditions for Eq. [A15] at the film/electrolyte interphase are given by:

$$C_{S,n} = C_{S,0} \text{ at } z = 0 \tag{A16}$$

The boundary condition at the electrode/film interphase can be derived by solving for the rate of consumption of the solvent as follows:

$$-\frac{dC_{S,n}}{dt} = C_{S,n}\left(k_{S,2} + k_{S,3} + k_{S,4}\right) - k_{S,3}C_{S,0}. \qquad [A17]$$

Integrating Eq. [A17] gives

$$-\frac{1}{\left(k_{S,2} + k_{S,3} + k_{S,4}\right)}\ln\left(\frac{C_S\left(k_{S,2} + k_{S,3} + k_{S,4}\right) - k_{S,4}C_{S,0}}{C_{S,0}\left(k_{S,2} + k_{S,3} + k_{S,4}\right) - k_{S,4}C_{S,0}}\right) = t. \qquad [A18]$$

Solving for $C_{s,n}$,

$$C_{S,p} = C_{S,0}e^{-\left(k_{S,2}+k_{S,3}+k_{S,4}\right)t} - \frac{C_{S,0}k_{S,4}}{\left(k_{S,2}+k_{S,3}+k_{S,4}\right)}e^{-\left(k_{S,2}+k_{S,3}+k_{S,4}\right)t} + \frac{C_{S,0}k_{S,4}}{\left(k_{S,2}+k_{S,3}+k_{S,4}\right)} \quad \text{at} \quad z = L(t)$$

$$. \; [A19]$$

The same approach is followed to obtain the boundary condition for the SEI layer on the cathode.

We assumed that the fluxes of the Mn^{2+} and H^+ in the electrolytes are not affected by the electric field in the electrolyte and their effects on the electric field are negligible because the concentration of the salt, $LiPF_6$, is much higher than the concentrations of Mn^{2+} and H^+ in the electrolytes. The material balance for Mn^{2+} the electrolyte is given by:

$$\varepsilon_{2,j}\frac{\partial c_{Mn^{2+}}}{\partial t} = D_{eff,Mn^{2+}}\frac{\partial^2 c_{Mn^{2+}}}{\partial z^2} + a_j R_0 - a_j R_{s,2}, \; j = pos, sep, neg \qquad [A20]$$

where $\varepsilon_{2,j}$ is the porosity of j region (pos = cathode, sep = separator, neg = negative), $D_{Mn^{2+}}$ is the effective diffusion coefficient of Mn^{2+}, a_j is the specific area, R_0 is the rate of Mn^{2+} dissolution described by Eq. 2.

The material balance for H^+ in the electrolyte is given by:

$$\varepsilon_{2,j} \frac{\partial c_{H^+}}{\partial t} = D_{eff,H^+} \frac{\partial^2 c_{H^+}}{\partial z^2} + a_j R_{s,1} \qquad \text{[A21]}$$

where D_{H^+} is the effective diffusion coefficient of H^+, c_{H^+} is the concentration of H^+ ions in the electrolyte. The effective diffusion coefficient of the Mn^{2+} and H^+ ions are assumed to be equal to D_s. We assume that Mn^{2+} and H^+ is reduced at the surface of the anode when the cell is charged according to the following reaction:

$$Mn^{2+} + 2e^- = Mn \qquad \text{[A22]}$$

$$H^+ + e^- = H_2 \qquad \text{[A23]}$$

The electric field of the reduced Mn and H_2 is assumed negligible due to the relatively small amount of Mn and H_2 at the anode compared to the Li ions.

Appendix B

B.1 Expressions

The open circuit potential as a function of the stoichiometric coefficient of the Li-ions in the spinel-based cathode and the graphite anode at a reference temperature of 25 °C are determined experimentally and fitted to the following relations:

$$
\begin{aligned}
U_{P,0} = 4.19829 + 0.0565661 \tanh(-14.5546y + 8.60942) \\
- 0.1031 \left[\frac{1}{(0.998432 - y)^{0.492465}} - 1.90111 \right] - \\
0.1209 \exp(-0.04738y^8) + 0.810239 \exp(-40(y - 0.3748))
\end{aligned}
\qquad \text{[B1]}
$$

$$
\begin{aligned}
U_{n,0} = 0.7222 + 0.1387x + 0.029x^{0.5} - \frac{0.0172}{x} + \frac{0.00109}{x^{1.55}} + 0.5136 \exp(0.90 - 18.7x) \\
- 0.8262 \exp(0.4241x - 0.4108)
\end{aligned}
$$

$$\text{[B2]}$$

where x and y are the stoichiometric coefficients of Li ions in the graphite anode and the spinel-based cathode, respectively.

The concentration and temperature-dependent ionic conductivity and diffusion coefficient in the binary electrolyte are given by [53].

$$
\kappa_i = 10^{-4} \times c_{e,i} \left(\begin{array}{l}
-10.5 + 0.668 \times 10^{-3} c_{e,i} + 0.494 \times 10^{-6} c_{e,i}^2 \\
+ 0.074T - 1.78 \times 10^{-5} c_{e,i} T - 8.86 \times 10^{-10} c_{e,i}^2 T \\
-6.96 \times 10^{-5} T^2 + 2.80 \times 10^{-8} c_{e,i} T^2
\end{array} \right),
\qquad \text{[B3]}
$$

$$
D_i = 10^{-4} \times 10^{-4.43 - \frac{54}{T - 229 - 5.0 \times 10^{-3} c_i} - 0.22 \times 10^{-3} c_{e,i}}.
\qquad \text{[B4]}
$$

The effective ionic conductivity and diffusion coefficient in the binary electrolyte are estimated using the following equations:

$$\kappa_{eff,i} = \kappa_i \varepsilon_i^{brugg_i} \qquad i = \text{p, s, n},$$
[B5]

$$D_{eff,i} = D_i \varepsilon_i^{brugg_i} \qquad i = \text{p, s, n}.$$
[B6]

The temperature dependent reaction rate constants for the electrodes are determined by

$$k_i = k_{i,0} \exp\left(\frac{E_{ak,i}}{R} \left(\frac{1}{T_0} - \frac{1}{T} \right) \right),$$
[B7]

where $k_{i,0}$ is the reaction rate constant for the electrode i at the reference temperature, T_0, and $E_{ak,i}$ is the activation energy related to the reaction constant for the electrode i.

The temperature dependent diffusion coefficients of Li-ion in the solid phase in the electrodes are determined by

$$D_{s,i} = D_{s,i,0} \exp\left(\frac{E_{ad,i}}{R} \left(\frac{1}{T_0} - \frac{1}{T} \right) \right),$$ [B8]

where $D_{s,i,0}$ is the reaction rate constant for the electrode i at the reference temperature, T_0, and $E_{ad,i}$ is the activation energy related to the diffusion coefficient of Li-ion in the solid phase in electrode i.

The standard deviation between the experimental and modeled discharge profile is estimated by

$$S_D = \sqrt{ \frac{1}{N-1} \sum_{j=1}^{N} \left[\left(U_{cell} \right)_j - \left(U_{cell} \right)_j^* \right]^2 },$$ [B9]

where N is the total number of experimental data points, $(U_{cell})_j$ and $(U_{cell})_j^*$ are the experimental and predicted values of the cell voltage at the jth data point, respectively. The cell voltages are replaced with the normalized capacity when estimating the standard deviation between the experimental and modeled normalized capacity.

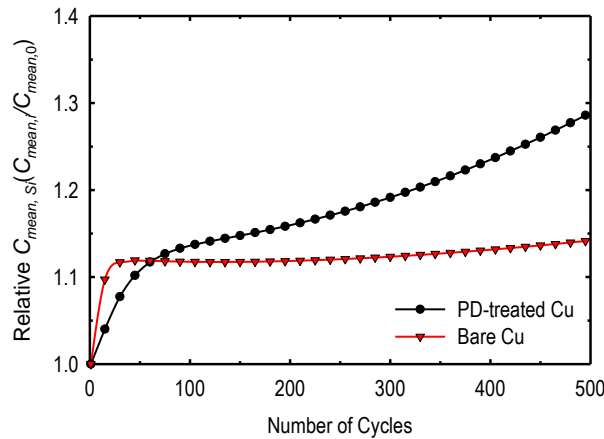# Appendix C

C.1 Li ions inventory in Si electrode

Figure C.1. Li ions inventory in the Si composite electrode for the cells with PD-treated and bare Cu current collector. There were more Li ions available in the cells with the PD-treated Cu current collector owing the existence of more active material due to the ability of PD to reduce delaminated Si particles.

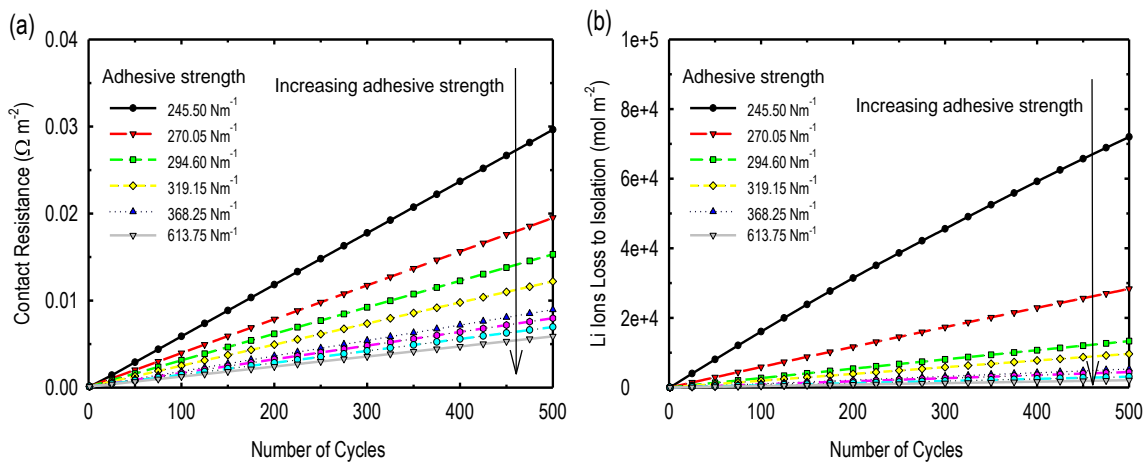## C.2 Effect of polydopamine design on degradation parameters

Figure C.2. Effect of adhesion strength between Si composite electron an Cu current collector on (a) contact resistance and (b) Li ions loss to isolation. Increasing the adhesion

strength results in a decrease in the contact resistance and Li ions loss to isolation owing to the reduction in the delaminated Si particles.
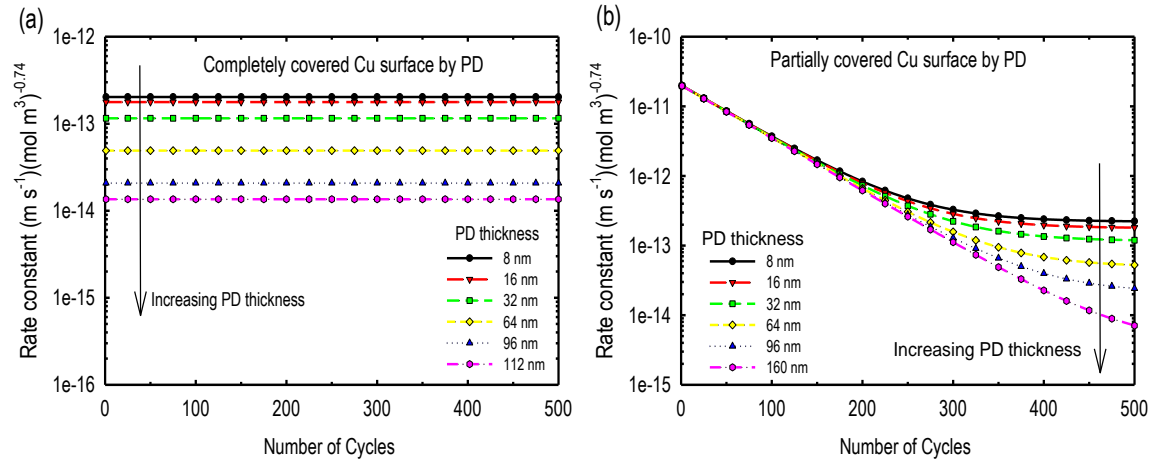

Figure C.3. Effect of various PD film (a) thickness (coverage $= 1$), (b) thickness (coverage $= 0.8$) on the rate constant. Increasing the thickness for a coverage of 1 only resulted in enhancing the tunneling the effect. However, for a coverage less the 1, an increase in the film thickness lead to an increase in both tunneling effect and passivation of the uncovered surface by an insulating polymeric film as cycling proceeded.
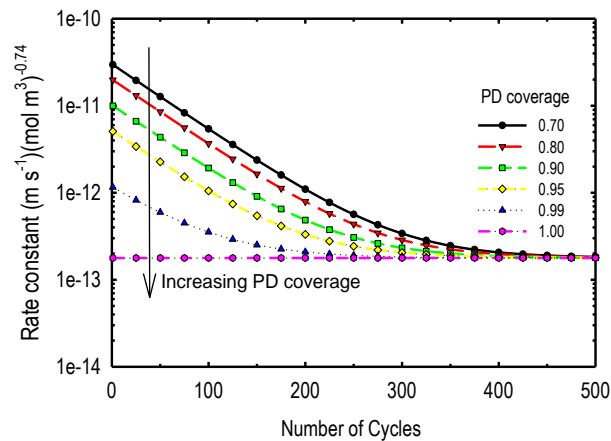

Figure C.4. Effect of various PD film coverage on the reaction rate constant. The thickness was maintained constant while varying the coverage.
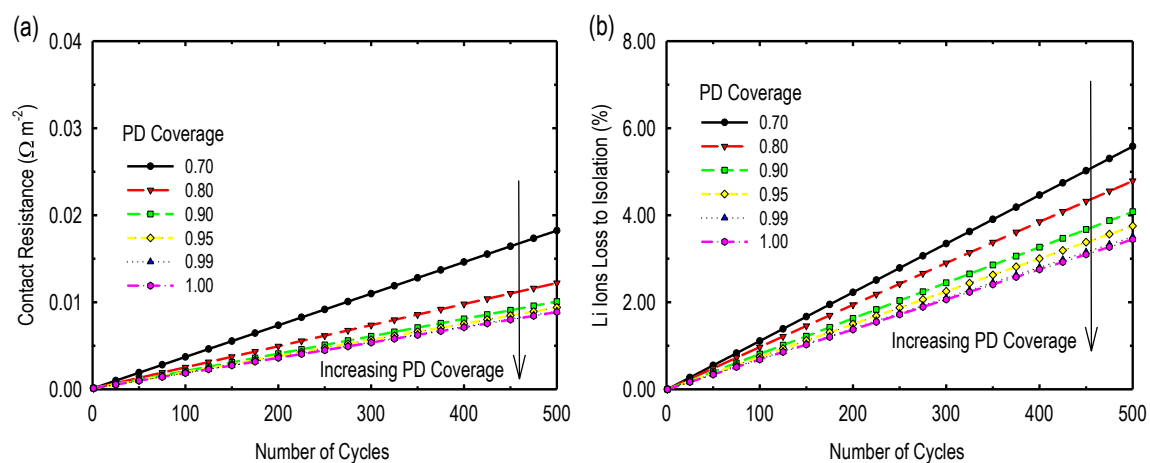
Figure C.5. Effect of PD film coverage on (a) contact resistance and (b) Li ions loss to isolation. Increasing the PD film coverage while maintaining the thickness constant lead to a decrease in the film resistance and Li ions loss to isolation.

요 약 문

리튬이온전지의 용량감소 원인 분석 및 모델링

리튬이온전지는 우수한 전기화학 특성으로 인해 전기자동차 및 에너지저장시스템 등, 다양한 에너지 저장 분야에 사용되고 있다. 특히, 전기자동차의 경우, 마일리지 확보뿐만 아니라 안전성 및 안정성에 대한 확보가 필수적이다. 전기자동차의 마일리지를 확보하기 위해서는 리튬이온전지의 에너지밀도를 증가시키는 방법이 있다. 예를 들어, 고용량 에너지 밀도를 갖는 활물질로 교체함으로써 전지의 용량을 증가시킬 수 있다. 그러나, 이러한 활물질의 적용은 심각한 전지의 용량감소로 이어질 수 있다. 이러한 용량 감소를 예측하기 위해선, 전지 내 복잡한 전기화학적 특성을 이해해야 한다. 하지만, 이런 모든 열화현상을 반영하여 전지의 수명을 예측 및 열화 요소를 정량화한 방법이 매우 부족한 실정이다.

본 논문은 고에너지밀도 활물질을 가진 리튬이온전지의 다양한 열화메카니즘을 확인할 수 있는 비파괴 용량감소 분석법을 제안한다. 핵심은 모델의 물리적 파라미터로부터 특정 열화 정보를 추출하는 것이다. 해당 물리적 파라미터는 파라미터 평가법 (Parameter Estimation Technique)에 의해 사이클이 반복됨에 따라 변한다. 이러한 통합적인 용량감소모델은 물리화학적 및 화학역학적 (Physico-Chemical and Chemo-Mechanical Model)모델을 기반으로 하며, 더 나아가 특정 열화메카니즘을 이해 및 정량화를 위해 모델을 응용 및 개선하였다. 수정된 용량 감소 모델은 리튬이온전지의 용량 및 안전성에 대한 다양한 전지설계 파라미터 및 접착 강도의 특성을 연구하는데 사용된다. 또한 계산의 효율성을 확보하기 위해, 물리 화학적 모델 및 P2D 모델 (Pseudo-Two-Dimensional Model)이 사용되었다. 개선 및 응용된 모델은 고에너지밀도 기반 활물질의 열화메카니즘을 예측 및 정량화를 향상시킬 수 있다. 이에 따라, 고에너지밀도를 가지는 전극의 활물질을 리튬이온전지에 효과적으로 적용함으로써 높은 마일리지 및 안정성을 확보한 전기자동차에 확장 가능하다. 이러한 발견은 기술 및 상업적 이익의 측면 모두에 적합하다.

Keywords: 리튬이온전지, 용량감소, 물리적 모델, 물리화학적 모델, 화학역학적 모델